Structural Insights into Pharmaceutical Solids from Synchrotron and Laboratory X-Ray Powder Diffraction Data

A thesis presented for the degree of

Doctor of Philosophy

in the

Faculty of Science

of the University of Strathclyde

by

Ryan Taylor

Strathclyde Institute of Pharmacy and Biomedical Sciences
University of Strathclyde
Glasgow

August 2012

Abstract

Structural insights into a wide range of pharmaceutically relevant solids, including pharmaceutical salts, co-crystals and amorphous solids have been gained through the use of X-ray powder diffraction techniques.

By combining global optimisation methods with high-quality powder diffraction data collected in the laboratory or at a synchrotron radiation source, the crystal structures of pharmaceutically relevant materials were solved successfully and reproducibly. The crystal structures which were solved are moderately complex, and at the midpoint of the complexity that can be routinely tackled by the DASH structure solution package. The crystal structures of six salts of the β_2-adrenoceptor agonist, salbutamol were solved directly from powder diffraction data collected in the laboratory. For five of these salts, no single crystals could be grown, however, for one salt, a single crystal was obtained, and comparison of the single crystal structure with the structure solved from powder diffraction data confirms the excellent accuracy of structures from powder diffraction data.

Co-crystals of the anti-epileptic drug, carbamazepine were examined on beamline I11 at Diamond Light Source in Oxfordshire. The beamline was in the optimisation phase when the co-crystals were examined, and were the first fully organic structures to be examined on the beamline. The accuracy of the structures solved from powder data was confirmed by comparison with published single crystal structures. Additional carbamazepine co-crystal structures were solved from laboratory powder diffraction data in order to assess the increase in accuracy associated with high resolution powder diffraction collected at a synchrotron radiation source.

Total scattering pair distribution function (TS-PDF) analysis was carried out on nanocrystalline powders of carbamazepine and the NSAID indomethacin, and it was found that melt-quenched “amorphous” carbamazepine is in actual fact a nanocrystalline version of form II, which is the clinically used polymorph.

Acknowledgements

I would like to thank my supervisors, Prof. Alastair J. Florence and Dr Kenneth Shankland (University of Reading) for their support and advice throughout the course of my studies. The input of Dr Norman Shankland is also gratefully acknowledged.

Thanks are also due to Dr Andrea Johnston (Strathclyde Institute of Pharmacy and Biomedical Sciences) for powder diffraction support; to Dr Jean-Baptiste Arlin and Mr Scott M^{c}Kellar (Strathclyde Institute of Pharmacy and Biomedical Sciences) for running single-crystal samples; to Dr Julie Bardin (Department of Pure and Applied Chemistry, University of Strathclyde) and Miss Rajni Miglani (Strathclyde Institute of Pharmacy and Biomedical Sciences) for performing geometry optimisation calculations; Miss Naomi Briggs (Strathclyde Institute of Pharmacy and Biomedical Sciences) for assisting with data collection; the Billinge group (Columbia University, New York) for their contribution to the TS-PDF studies; APS Argonne (Argonne National Laboratory, Argonne, Chicago) and Diamond Light Source (Didcot, Oxfordshire) for beamtime. Thanks are also due to the EPSRC and centre for molecular and structural dynamics (CMSD) for funding during this project.

Finally, I would like to thank my friends and family for their support and encouragement throughout the course of my studies.

Contents

Chapter 1	**Introduction**	**1**
1.1	Background	2
1.2	Pharmaceuticals and the solid state	4
1.3	Crystal structure	7
1.4	The amorphous state	7
1.5	Overview of structure determination by single crystal methods	8
1.6	X-ray powder diffraction	10
1.6.1	Laboratory X-rays vs. synchrotron radiation	12
1.7	Structure determination from powder diffraction data (SDPD)	14
1.7.1	Direct methods	14
1.7.2	Structure solution by global optimisation	15
1.7.2.1	General	15
1.7.2.2	The structural fragment	17
1.7.2.3	The molecular Z-matrix	18
1.7.2.4	Structure solution by simulated annealing	20
1.8	The SDPD process	22
1.8.1	Sample preparation and data collection	22
1.8.2	Indexing the powder diffraction data	23
1.8.3	Space group determination	24
1.8.4	Pawley refinement	24
1.8.5	Model building	25
1.8.6	Simulated annealing structure solution	27
1.8.7	Rietveld refinement	29
1.8.8	Crystal structure verification	31
1.8.8.1	Interactions and molecular geometry	31
1.8.8.2	Unconstrained refinement	31
1.8.8.3	DFT analysis of the structure	31
1.9	Study of amorphous structure	32
1.9.1	General	32
1.9.2	Thermal analysis of amorphous pharmaceuticals	33
1.9.3	Spectroscopic analysis of amorphous pharmaceuticals	34
1.9.4	Total scattering and PDF analysis	34
1.10	Summary	37

Chapter 2 Aims and Objectives 38

2.1 Aims 39

2.2 Objectives 39

Chapter 3 Materials and methods 41

3.1 Materials 42

3.2 Methods 43

3.2.1 Laboratory XRPD 43

3.2.2 Synchrotron powder diffraction 44

3.2.2.1 Beamline I11 at DLS 44

3.2.2.2 Beamline ID-11-B at APS 44

3.2.3 Standard Structure Solution Sequence (SSSS) 45

3.2.3.1 Pattern indexing and space group determination 45

3.2.3.2 Pawley refinement 46

3.2.3.3 Model building and Z-matrix preparation 46

3.2.3.4 Simulated annealing structure solution 48

3.2.3.5 Rigid body Rietveld refinement 48

3.2.3.5.1 Preparation of the rigid bodies 49

3.2.3.5.2 Unconstrained Rietveld refinement 50

3.2.3.5.3 DFT calculations 50

Chapter 4 Crystal structures of pharmaceutically acceptable carbamazepine co-crystals from synchrotron and laboratory X-ray powder diffraction data 52

4.1 Introduction 53

4.2 Diamond Light Source (DLS) 56

4.3 Preparation of polycrystalline materials 58

4.4 X-ray powder diffraction 58

4.4.1 Laboratory X-ray powder diffraction 58

4.4.2 Synchrotron X-ray powder diffraction 58

4.5	Indexing and choice of space group	58
4.6	Thermal analysis of the co-crystals	59
4.7	Model building and Z-matrix preparation	59
4.8	Simulated annealing structure solution	60
4.9	Rigid body Rietveld refinement	61
4.10	Density functional theory (DFT) calculations	61
4.11	Results	62
4.11.1	Indexing results	62
4.11.2	Results from simulated annealing structure solution	62
4.11.3	CBZ: OXA and CBZ: GLY co-crystals	63
4.11.4	Thermal analysis results	65
4.11.5	The crystal structures of the CBZ co-crystals	66
4.11.5.1	CBZ: HNA co-crystal	66
4.11.5.2	CBZ: CAM co-crystal	69
4.11.5.3	CBZ: BEN co-crystal	72
4.11.5.4	CBZ: SAL co-crystal	75
4.12	Comparison of single crystal and powder structures	79
4.13	Summary	83

Chapter 5 Crystal structures of organic salbutamol salts from laboratory X-ray powder diffraction data **84**

5.1	Introduction	85
5.2	Preparation and characterisation of salbutamol salts	91
5.2.1	Solution based salt screening	91
5.2.2	Mechanochemistry based salt screening	92
5.2.3	Indexing of the salts	92
5.2.4	Thermal analysis of the salts	92
5.2.5	XRPD data collection	93
5.2.6	Model building and Z-matrix preparation	93
5.2.7	Simulated annealing structure solution	94

5.2.8	Rigid body Rietveld refinement	94
5.2.9	DFT calculations	94
5.3	Results	95
5.3.1	Screening results	95
5.3.2	Indexing results	96
5.3.3	Thermal analysis of the salts	96
5.3.4	Simulated annealing results	101
5.3.5	Crystal structures of the salbutamol salts	102
5.3.5.1	Crystal structure of salbutamol acetate	103
5.3.5.2	Crystal structure of salbutamol butyrate	107
5.3.5.3	Crystal structure of salbutamol formate	110
5.3.5.4	Crystal structure of salbutamol nicotinate	112
5.3.5.5	Crystal structure of salbutamol saccharinate	115
5.3.5.6	Crystal structure of salbutamol xinafoate	117
5.3.6	DFT calculations and unconstrained Rietveld refinement	120
5.4	Summary	122

Chapter 6 Characterisation of X-ray amorphous pharmaceuticals using a Total Scattering Pair Distribution Function (TS-PDF) approach 124

6.1	Introduction	125
6.1.1	Methods of preparing amorphous pharmaceuticals	127
6.1.1.1	Milling	127
6.1.1.2	Melt-quenching	127
6.1.1.3	Melt extrusion	128
6.1.1.4	Formation of amorphous solid dispersions (ASDs)	128
6.1.2	Structural characterisation and analysis of the amorphous state	129
6.2.	Preparation and characterisation of amorphous pharmaceuticals	131
6.2.1	Preparation of amorphous CBZ and IND	131
6.2.2	Laboratory characterisation of amorphous CBZ and IND	131
6.2.2.1	Laboratory XRPD	131

6.2.2.2 Thermal analysis 132
6.2.2.3 Study of recrystallisation kinetics 132
6.2.2.4 Preparation of pure phase pharmaceutical polymorphs 132
6.2.3 Characterisation of materials at APS 133
6.3 Results and discussion 134
6.3.1 Laboratory XRPD characterisation of amorphous pharmaceuticals 134
6.3.1.1 Laboratory XRPD characterisation of amorphous CBZ 134
6.3.1.2 Thermal analysis of amorphous CBZ 135
6.3.1.3 Study of recrystallisation kinetics of CBZ 137
6.3.2. Total Scattering Pair Distribution Function analysis 140
6.3.2.1 Analysis of CBZ by Total Scattering Pair Distribution Function 141
6.3.2.2 Analysis of IND by Total Scattering Pair Distribution Function 145
6.4 Summary 150

Chapter 7 Conclusions and further work 151

7.1 Conclusions 152
7.1.1 Crystal structures of pharmaceutically acceptable co-crystals from synchrotron and laboratory X-Ray powder diffraction data 152
7.1.2 Crystal structures of organic salbutamol salts from laboratory X-ray powder diffraction data 153
7.1.3 Characterisation of X-ray amorphous pharmaceuticals using a Total Scattering Pair Distribution Function (TS-PDF) approach 154
7.2 Further work 155
7.2.1 Crystal structures of pharmaceutically acceptable co-crystals from synchrotron and laboratory X-Ray powder diffraction data 155

7.2.2 Crystal structures of organic salbutamol salts from laboratory X-ray powder diffraction data 156

7.2.3 Characterisation of X-ray amorphous pharmaceuticals using a Total Scattering Pair Distribution Function (TS-PDF) approach 158

References **159**

Appendices Please note that Appendix 4 is included on a CD

Appendix 1 Publications arising from this work

Appendix 2 An example TOPAS rigid-body Rietveld refinement ".inp" file

Appendix 3 DSC data for CBZ co-crystals

Appendix 4 CIF files for salbutamol salts

List of Figures

Chapter 1

1.1 XRPD fingerprints of carbamazepine form III and carbamazepine dihydrate 3

1.2 Molecular structure of zafirlukast 6

1.3 Molecular structure of raffinose 8

1.4 Laboratory vs. synchrotron data collected from a sample of carbamazepine: 1-hydroxy-2-naphthoic acid co-crystal 13

1.5 Molecular structure of clomipramine hydrochloride 15

1.6 Molecular structure of hydrochlorothiazide 17

1.7 Molecular structure of verapamil hydrochloride 18

1.8 Molecular structure of the nicotinate anion showing atomic numbering 18

1.9 Molecular structure of capsaicin 21

1.10 Molecular structure of benfluorex hydrochloride 21

1.11 Molecular structure of bromophenol blue 26

1.12 Molecular structure of bromocresol green 26

1.13 Molecular structure of ritodrine hydrochloride 27

1.14 Molecular structure of chloramphenicol palmitate 28

1.15 Molecular structure of guaifenesin 30

1.16 X-ray amorphous halo collected from a sample of anhydrous raffinose 33

Chapter 4

4.1 Supramolecular synthons observed in carbamazepine co-crystals 55

4.2 Evidence of radiation damage to a sample of CBZ:GLY co-crystal 64

4.3 Hydrogen bonded interactions in the CBZ: HNA co-crystal 67

4.4 Packing diagram for the CBZ: HNA co-crystal 68

4.5 Final Rietveld plot for the CBZ: HNA co-crystal 69

4.6 Hydrogen bonded interactions in the CBZ: CAM co-crystal 70

4.7 Packing diagram for the CBZ: CAM co-crystal 71

4.8 Final Rietveld plot for the CBZ: CAM co-crystal 72

4.9 Hydrogen bonded interactions in the CBZ: BEN co-crystal 73

4.10 Packing diagram for the CBZ: BEN co-crystal 74

4.11 Final Rietveld plot for the CBZ: BEN co-crystal 75

4.12 Hydrogen bonded interactions in the CBZ: SAL co-crystal 76

4.13 Packing diagram for the CBZ: SAL co-crystal 77

4.14 Final Rietveld plot for the CBZ: SAL co-crystal 78

4.14 Overlay of the single crystal and refined powder structure of the CBZ: HNA co-crystal 81

Chapter 5

5.1 Molecular structure of propoxyphene napsylate 86

5.2 Molecular structure of salmeterol xinafoate 86

5.3 Molecular structure of salbutamol base 88

5.4 Molecular structure of salbutamol hemisulphate 88

5.5 Molecular structures of the acids used to form salbutamol salts 91

5.6a DSC trace of salbutamol butyrate 97

5.6b DSC trace of salbutamol acetate 97

5.6c DSC trace of salbutamol formate 98

5.6d DSC trace of salbutamol nicotinate 98

5.6e DSC trace of salbutamol saccharinate 99

5.6f DSC trace of salbutamol xinafoate 99

5.7 The effects of heating a sample of salbutamol butyrate overnight 100

5.8 Hydrogen bonded interactions in salbutamol acetate 104

5.9 Formation of alternating layers of ions in salbutamol acetate 105

5.10 Packing diagram for salbutamol acetate 106

5.11 Final Rietveld plot for salbutamol acetate 107

5.12 Packing diagram for salbutamol butyrate 108

5.13 Final Rietveld plot for salbutamol butyrate 109

5.14 Packing diagram for salbutamol formate 111

5.15 Final Rietveld plot for salbutamol formate 112

5.16 Hydrogen bonded interactions in salbutamol nicotinate 113

5.17 Packing diagram for salbutamol nicotinate 114

5.18 Final Rietveld plot for salbutamol nicotinate 115

5.19 Hydrogen bonded interactions in salbutamol saccharinate 116

5.20 Final Rietveld plot for salbutamol saccharinate 117

5.21 Packing diagram for salbutamol xinafoate 118

5.22 Final Rietveld plot for salbutamol xinafoate 119

5.23 Overlay of the refined crystal structure with the CASTEP optimised structure of salbutamol acetate 121

Chapter 6

6.1 The molecular structure of AMG 517 126

6.2 The molecular structure of indomethacin 130

6.3 Amorphous haloes observed during laboratory XRPD experiments 135

6.4 Typical DSC trace for melt-quenched CBZ 137

6.5 Effect of annealing an amorphous sample of CBZ at 96°C for 15 minutes 139

6.6 Total scattering and total scattering pair distribution function data collected from CBZ at beamline ID-11-B 142

6.7 Comparison of TS-PDFs from melt-quenched CBZ and attenuated TS-PDF data (4.5nm domain size) 144

6.8 Total scattering diffraction patterns and TS-PDF data collected from IND 146

6.9 TS-PDF data collected from melt-quenched and crystalline CBZ form III 149

Chapter 7

7.1 The molecular structure of stearic acid 155

7.2 The molecular structure of azelaic acid 156

List of Tables

Chapter 1

1.1 Solubility differences of different solid forms of carbamazepine in simulated duodenal fluid 5

1.2 FWHM values for data collected from a sample of carbamazepine: 1-hydroxy-2-naphthoic acid co-crystal in the laboratory and at a synchrotron radiation source 12

1.3 Indexing figures of merits for data collected from a sample of carbamazepine: 1-hydroxy-2-naphthoic acid co-crystal collected in the laboratory and at a synchrotron radiation source 13

1.4 Some computer programs used to solve crystal structures from powder diffraction data by global optimisation methods 17

1.5 Z-matrix description of the nicotinate ion used as an input model for structure solution of salbutamol nicotinate 19

Chapter 3

3.1 Compound names and molecular formulae for compounds throughout the experimental chapters 42

3.2 Instrument configuration for laboratory XRPD experiments 43

3.3 Mean values for the amine and ammonium portions in known structures chemically similar to salbutamol 47

3.4 An example of a ".rgd" file for rigid-body Rietveld refinement in TOPAS 49

Chapter 4

4.1 Simulated annealing protocol for CBZ co-crystals 60

4.2 Results from indexing the powder data in DICVOL06 62

4.3 Results of simulated annealing runs for CBZ co-crystals 63

4.4 Melting point of the CBZ co-crystals 65

4.5 Refined unit cell parameters for the co-crystal single crystal structures 79

4.6 Refined unit cell parameters for the co-crystal powder structures 79

4.7 Hydrogen bond distances for CBZ co-crystals solved from powder data 80

4.8 Hydrogen bond distances for single crystal CBZ co-crystal structures 80
4.9 RMSD values between single crystal and powder structures 81

Chapter 5

5.1 The frequency of occurrence of the 10 most common pharmaceutical salts 87
5.2 Solubility and log P data for salbutamol base and salbutamol hemisulphate 88
5.3 pKa values of salbutamol and the pharmaceutically acceptable acids 92
5.4 Sources of the acid anion input models for the salbutamol salts 93
5.5 Simulated annealing protocol for the salbutamol salts 94
5.6 Melting points of the salbutamol salts 96
5.7 Crystallographic data for the salbutamol salts 101
5.8 Hydrogen bond geometries of the ammonium group in the salbutamol salts 102
5.9 Conformation of C-C-N-C chain of the salbutamol ion in each of salts 103
5.10 Simulated annealing results using two half-occupancy butyrate ion Z-matrices 110
5.11 RMSD between the experimental and simulated structures 120

Chapter 6

6.1 Thermal properties of melt-quenched CBZ 136
6.2 Correlation co-efficients between the solid forms of CBZ 143
6.3 Correlation co-efficients between the solid forms of IND 146
6.4 Maximum ranges for laboratory diffractometers to yield TS-PDF data 148

Chapter 7

7.1 Degrees of freedom in potential CBZ: AZL co-crystals 156
7.2 Crystallographic data for the salbutamol fatty acid salts 157

Chapter 1

Introduction

1.1 Background

In the pharmaceutical industry, an enormous amount of time and money are spent in developing a new drug with estimates that it takes 12 years and up to £232 million to bring a new drug onto the market. Given the significant costs involved, the speed with which a drug can be taken from initial synthesis to marketed product is of vital importance. An important part of drug development is physical form selection, where the most appropriate polymorph, salt or solvate of the drug is chosen for subsequent development. Characterisation of crystalline forms is of paramount importance in physical form selection, and the ability to solve the crystal structure of a given crystalline form of the drug gives an unambiguous description of that form.

The definitive method for crystal structure solution is single crystal X-ray diffraction (SXD). However, there is no guarantee that a compound of interest will form suitable single crystals for SXD. In such cases, X-ray powder diffraction (XRPD) can be used in lieu of SXD, and structure determination from powder diffraction data (SDPD) is a powerful technique which has risen to prominence over the past few years (David *et al.*, 2002). XRPD has traditionally been used in pharmaceutical development to study polycrystalline solids; uses of the technique include fingerprinting polycrystalline samples obtained from crystallisation screens and tracking structural changes in a sample via the evolution of a new powder pattern as a function of temperature or relative humidity. Figure 1.1 shows an overlay of XRPD fingerprints of carbamazepine form III and carbamazepine dihydrate.

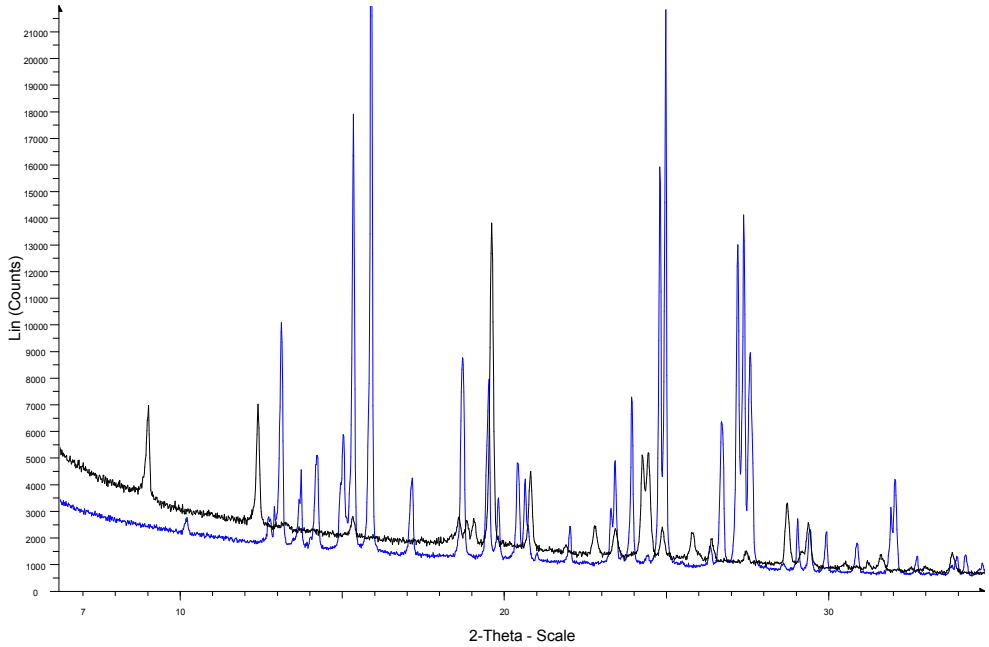

Figure 1.1 XRPD fingerprints of carbamazepine form III (blue) and carbamazepine dihydrate (black). These two solid forms are readily distinguished from each other by the differences in peak positions and intensity.

The use of SDPD is impacted by the inevitable loss of information due to the collapse of the 3-dimensional crystal lattice to the single dimension of a powder diffraction pattern. The resultant peak overlap makes the extraction of intensities and subsequent calculation of reliable structure factors much more difficult than for SXD and traditional Direct Methods are therefore not appropriate (ref) That said, Global optimisation methods for solving structures provide an effective tool. The crystal structures of small organic compounds (molecular and ionic) with less than 21 degrees of freedom (DOF) can be solved 'routinely' from XRPD data using a global optimisation method (Florence *et al.*, 2005, David *et al.*, 1998).

The maximum size of problem that can be successfully tackled by SDPD i.e. where global optimisation approaches can successfully locate the global minimum is difficult to define in absolute terms. It is dependent on a number of factors that include: the conformational and

crystallographic complexity of the structure in terms of total number of DOF comprising internal (conformational flexibility of each fragment) and external (position and orientation of each fragment) DOF; the accuracy of intensity estimates obtained from powder diffraction data; the effectiveness of the global optimisation method in locating the global minimum. Significantly, the improvement in instrumentation (high sensitivity solid-state X-ray detectors, new third generation synchrotron radiation sources) in recent years means that high quality data and therefore accurate reflection intensity estimates are accessible, adding to the favourable aspects for tackling relatively complex structures routinely from XRPD data

1.2 Pharmaceuticals and the solid state

Well over half of the drugs used in medicine are administered orally in the form of tablets or capsules. It is essential to fully characterise the solid state form, including polymorphs, of a drug which is intended for oral administration, as dissolution rate and therefore bioavailability can vary significantly for different forms. For example, it has been shown that different polymorphic forms of chloramphenicol palmitate, mefenamic acid and oxytetracycline all have different dissolution and absorption profiles in humans (Singhal & Curatolo, 2004). It has also been shown that different polymorphic forms of the anti epileptic drug carbamazepine have different bioavailabilities. This was demonstrated using an artificial stomach-duodenum model and it was found that the most stable form of carbamazepine also has the highest bioavailabilty (which is unusual), as confirmed by the concentrations in simulated duodenal fluid (Carino *et al.*, 2006). These results are shown in Table 1.1.

Table 1.1 Solubility differences of different solid forms of carbamazepine in simulated duodenal fluid (from Carino *et al.,* 2006)

CBZ solid form	concentration in duodenal fluid (mg/mL)
CBZ form I	0.98
CBZ form III	1.24
CBZ dihydrate	0.69

Solvates, which are multi component solids in which one component is normally a liquid are also common; aminophylline (theophylline ethylenediamine 2:1 solvate), cabazitaxel acetone solvate and warfarin sodium isopropanol solvate (Sheth *et al.*, 2002) are examples of pharmaceutically acceptable solvates (www.drugbank.ca). The most acceptable solvate in pharmaceutical terms is water, which makes the multi-component crystal a hydrate. Several pharmaceutical hydrates are used in clinical practice, examples include: ampicillin trihydrate; gadodiamide hydrate; cephalexin hydrate; cevimeline hydrochloride hydrate; vidarabine; cilazapril (www.drugbank.ca) Also, many orally administered drugs are presented as highly crystalline salts, which may be preferred for various reasons including the ability to control the solubility of the drug, improved physical stability, reduced toxicity and reduced hygroscopicity are all attractive benefits of salt formation (Haynes *et al.*, 2005).

There has also been considerable interest in amorphous drugs, due to their potential to yield superior dissolution rate and bioavailability. Examples of marketed amorphous drugs include: nelfinavir mesylate; paromycin sulphate; rosuvastatin calcium; anhydrous warfarin sodium and zafirlukast (www.drugbank.ca). Amorphous drugs are, however, thermodynamically unstable (due to the higher free energy relative to the crystalline counterparts) and there is often a strong tendency for spontaneous recrystallisation, possibly as a metastable polymorph, which could result in unreliable doses of the drug in the bloodstream. Since the crystalline drug is also less soluble than its amorphous counterpart, it can be difficult to routinely formulate amorphous drugs so that the benefits of higher dissolution are maintained

for long periods of time due to their limited stability. XRPD is useful in the identification of drug samples as 'X-ray' or 'diffraction' amorphous, due to the characteristic lack of Bragg peaks. Stability studies can therefore be carried out, and the crystallinity of the sample as a function of time and storage conditions can readily be examined by XRPD measurements. For example, the anti-asthmatic drug zafirlukast is formulated as the amorphous form A, but it has been shown that at high relative humidity and temperature, the drug can recrystallise as the unstable hydrate, form B which is difficult to handle during formulation (Goldring *et al.*, 2004). The structure of zafirlukast is shown in Figure 1.2

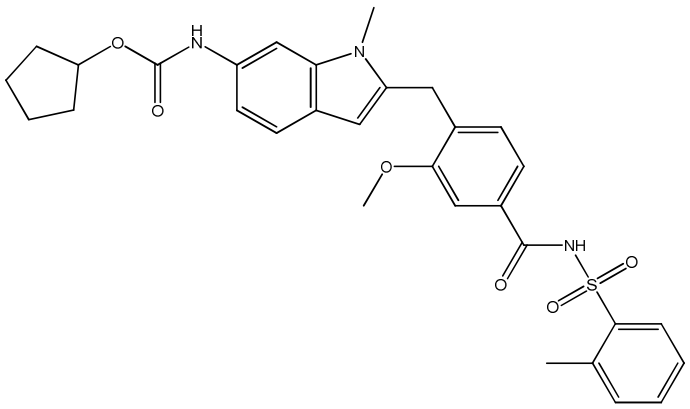

Figure 1.2 Molecular structure of zafirlukast.

The various solid forms described above are commonly prepared during solid form screens during preclinical drug development. The screening experiments are often extensive, as it is important to characterise all solid forms (salts, solvates, co-crystals, polymorphs or amorphous forms) of a compound as early as possible in the development process. Typically, solid forms are generated by; traditional solution crystallisation from various solvents, slurry experiments, neat grinding, solvent assisted grinding, cryomilling, spray drying, melt-quenching or desolvation of a solvate. There is a chance that only polycrystalline samples will be obtained from screening experiments, single crystals are not immediately available

from grinding or slurrying experiments, in these cases, the first step is to attempt to obtain single crystal samples of the material

1.3 Crystal structure

Crystalline material is characterised by a high degree of internal order. Crystals are composed of groups of atoms (the structural motif, which can be a molecule or an ion) repeated at regular intervals in 3 dimensions. Each group of atoms can be represented by a single imaginary point, and the collection of points is the crystal lattice, which extends infinitely in 3 dimensions. The basic building block of a crystal is the unit cell, which is an imaginary parallelepiped characterised by the 3 vectors, a, b and c and the angles α, β and γ. The high degree of internal order characteristic of crystalline materials gives rise to favourable characteristics, such as a well defined melting point, high chemical purity and good physical and chemical stability

1.4 The amorphous state

In an amorphous solid, there is no long range three dimensional translational order, which is characteristic of crystalline materials. Instead, the molecules simply pack in such a way that the local free energy is minimised. There are, however, 'nearest neighbour' and 'next nearest neighbour' interactions between the molecules. The lack of long-range order means that no structural information is immediately available from a powder diffraction experiment due to the lack of constructive interference; instead, a characteristic 'halo' is observed in the measured pattern. The use of pair distribution function (PDF) analysis, however, can enable structural information on local packing and microstructure in solid state pharmaceuticals to be obtained from an otherwise X-ray amorphous sample. In a pharmaceutical context, PDF

analysis has been carried out to confirm the miscibility of amorphous drug-polymer dispersions (Newman *et al.*, 2008, Bates *et al.*, 2006) and to study structural changes in raffinose pentahydrate as a function of hydration state, since anhydrous raffinose is X-ray amorphous (Bates *et al.*, 2007). The structure of raffinose is shown in Figure 1.3

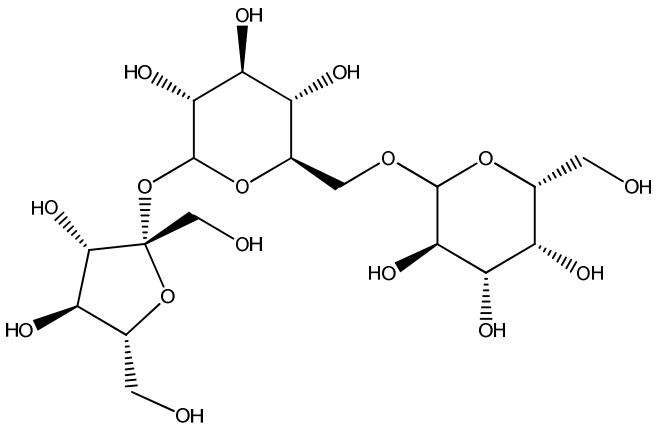

Figure 1.3 Molecular structure of raffinose

1.5 Overview of structure determination using single crystal methods

Traditionally, single crystal structures are solved by direct methods. The central dogma of direct methods is that the observed reflection intensities contain structural information. In the simplest terms, equation 1.1 shows the relationship between observed reflection intensity, I, and structure factor moduli F

$$I \propto \left|F^2\right| \qquad 1.1$$

X-rays are scattered by the electron density in the structure, when 2θ is zero, the electrons in an atom scatter in phase, and the scattering factor (f) for the atom is simply the atomic

number. However, as 2θ is increased, the amplitude of the scattering factor falls, due to destructive interference in the scattered X-rays. The entire crystal structure diffracts the incident X-ray, which means the scattering factors of all atoms in the structure must be considered. The structure factor is a calculation which takes scattering by groups of atoms into account. The structure factor is a complex number, with both an amplitude and a phase. For reflections from the Miller planes (h, k, l planes) of the crystal lattice, the structure factor can be found by equation 1.2, where the summation is over every atom (j) in the unit cell, and also over all fractional coordinates (x,y,z) in the unit cell (Glusker *et al.*, 1994).

$$F_{hkl} = \sum_j f \exp(2\pi i[hx_j + ky_j + lz_j]) \qquad 1.2$$

In order to solve the structure, electron density must be taken into account. The structure factor shown in equation 1.2 can be considered to represent diffraction from electron density within the unit cell. Electron density is the number of electrons per unit volume, and in structure solution attempts, Fourier transformation is normally carried out. A Fourier transformed structure factor is shown in equation 1.3, the triple summation is because the calculation is over all values of h, k and l respectively.

$$\rho(xyz) = \frac{1}{V} \sum_h \sum_k \sum_l F(hkl) \exp(-2\pi i[hx + ky + lz]) \qquad 1.3$$

The above expression is used to prepare Fourier maps, which can then be used to solve the structure of interest (Glusker *et al.*, 1994). The central problem in crystallography is the phase problem, which must be solved or the structure solution attempt will fail. To carry out

the calculation shown in equation 1.3, the structure factors are required. However, only the magnitude is known, the phase angle is not, and must be calculated. The phase angle is calculated as shown in equation 1.4

$$\rho(xyz) = \frac{1}{V}\sum_{h}\sum_{k}\sum_{l}\left|F(hkl)\right|\exp[-2\pi i(hx + ky + lz) - \phi(hkl) \qquad 1.4$$

From the above equation, the calculated phase angle (ϕ) can be applied to the observed structure factors. If the resulting structure appears reasonable, the structure can be refined.

1.6 X-ray powder diffraction

It is possible to obtain structure factors for a crystalline material where no single crystal is available. However, the process of obtaining these structure factors is much more difficult than for single crystal techniques, due to the reflection overlap in the powder diffraction pattern, which becomes increasingly severe at high angle. Form factor fall-off at high angle also reduces the intensity information that can reliably be extracted from a powder diffraction pattern. The loss of information in a powder diffraction pattern makes the data: parameter ratio much less favourable than for a single crystal sample. In a single crystal sample, there are typically thousands of observed intensities (I_{obs}), but in a typical powder diffraction pattern typically there are only hundreds of I_{obs}. In order to determine independently a structure containing 12 atoms requires (12x3) co-ordinates and 12 isotropic atomic displacement parameters, giving a total of 48 independent parameters. If a data: parameter ratio of at least 10:1 can be obtained, and if data to atomic resolution (1Å) are available then Direct Methods would work very well. Unfortunately, these conditions are very difficult to

achieve from powder diffraction data, although this can be obtained the structure under study is very simple, and high resolution synchrotron data are available

Another complication of powder diffraction is preferred orientation, which can also complicate the estimation of intensities. That said, light grinding of the sample, use of capillary transmission geometry and rotation of the sample during data collection can all but eliminate preferred orientation. It is sometimes necessary to mathematically model preferred orientation (Rietveld, 1969, Dollase, 1986) to get the best possible fit to the experimental powder data.

1.6.1 Laboratory X-rays vs. synchrotron radiation

Synchrotron radiation is produced at central facilities such as Diamond Light Source (DLS), the European Synchrotron Radiation Facility (ESRF) and the Advanced Photon Source (APS) at Argonne National Laboratory, and is typically highly intense and tuneable. These characteristics are markedly different to the radiation obtained from metal anodes in a commercial laboratory instrument. The spatial and angular resolution of data collected at a synchrotron source is much better than that available from a laboratory instrument. As an example, Table 1.2 shows the average FWHM in data collected from a sample of carbamazepine: 1-hydroxy-2-naphthoic acid co-crystal in the laboratory and at a synchrotron radiation source.

Table 1.2 Full Width Half Maximum **(**FWHM) values (°2θ) for data collected from a sample of carbamazepine: 1-hydroxy-2-naphthoic acid co-crystal in the laboratory and at a synchrotron radiation source

Dataset	FWHM/°
Laboratory	0.071
Synchrotron	0.016

Furthermore, due to the high brilliance of the synchrotron radiation, peaks which are relatively weak in laboratory data are much more intense, and the peak positions in general are more accurately located which can have a significant impact on the success of pattern indexing. Another advantage of synchrotron data is the use of multiple crystal analysers, which provide excellent 2θ coverage, thus allowing very rapid data collection. Table 1.3 shows the results of indexing data collected from a sample of carbamazepine: 1-hydroxy-2-naphthoic acid collected on a laboratory instrument and at a synchrotron source.

Table 1.3 Indexing figures of merit for data collected from a sample of carbamazepine: 1-hydroxy-2-naphthoic acid co-crystal in the laboratory and at a synchrotron radiation source.

Dataset	M_{21}
Laboratory	24.5
Synchrotron	52.7

The improvement in intensity and resolution that can be obtained at synchrotron sources is shown in Figure 1.4. The data were collected from a pharmaceutical sample in the laboratory and at a synchrotron radiation source. The difference is obvious at higher angle.

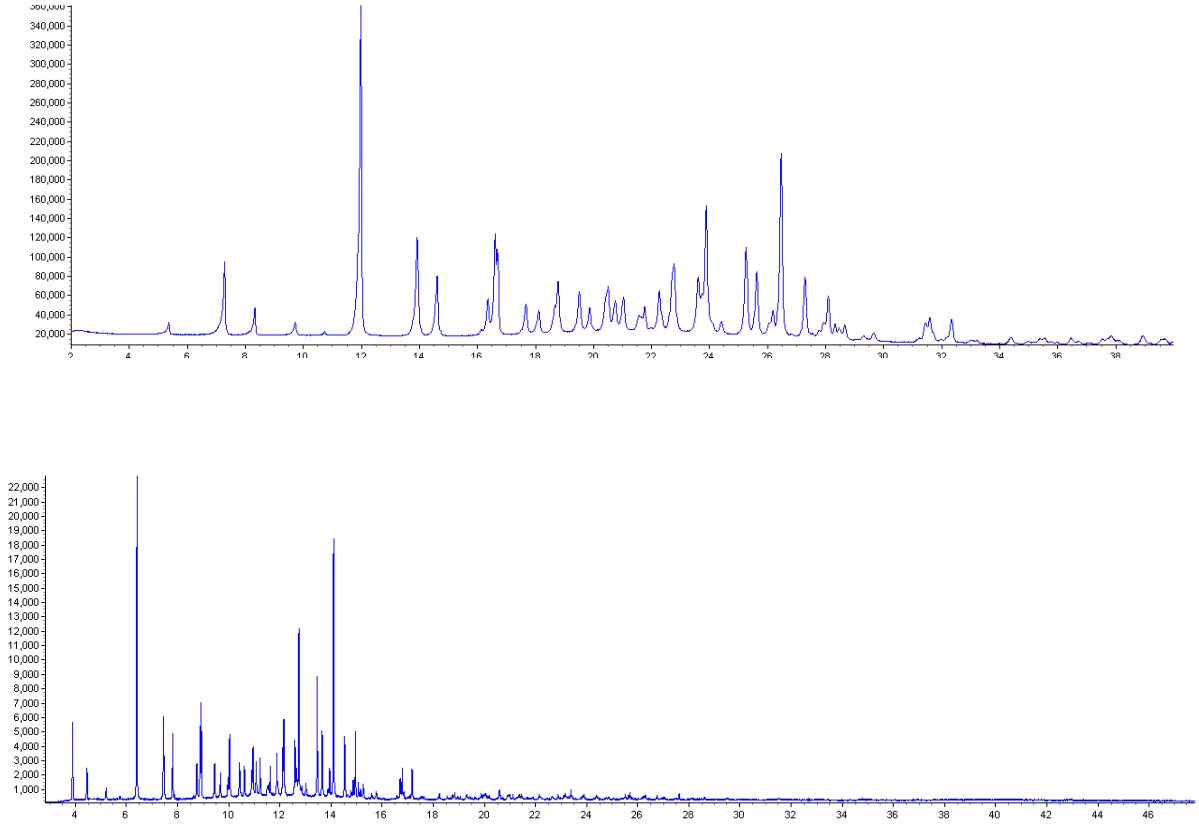

Figure 1.4 Laboratory (top) vs. synchrotron (bottom) data collected from a sample of carbamazepine: 1-hydroxy-2-naphthoic acid co-crystal. The weak reflections at low angle are much more intense in the synchrotron dataset, which aided indexing attempts

Typically, only modestly complex crystal structures can be routinely solved and refined from powder data (Fernandes *et al.*, 2007, Florence *et al.*, 2005, Shankland *et al.*, 1997, David *et al.*, 1998). However, the availability of synchrotron data has made it possible to index and successfully solve the crystal structures of biomacromolecules from powder diffraction data, ranging from 1,3-distearoyl-2-oleoylglycerol ($C_{57}H_{108}O_6$) found in cocoa butter to the second SH3 binding domain of ponsin. (Margiolaki *et al.*, 2007, Margiolaki & Wright, 2008, Wright *et al.*, 2008, Peschar *et al.*, 2004). Such complex crystal structures are an impressive demonstration of the capabilities of high resolution powder diffraction data.

A downside to the use of high intensity synchrotron radiation is the potential for radiation damage, which organic molecules can be prone to (Beukes *et al.*, 2007, Wright *et al.*, 2008). Radiation damage can cause peak broadening, peak shifting and the appearance of new peaks in the diffraction pattern making indexing and structure solution impossible. Nevertheless, synchrotron radiation is an extremely powerful tool for powder diffraction studies where the enhanced accuracy, resolution and count times are required.

1.7 Structure determination from powder diffraction data (SDPD)

1.7.1 Direct methods

If accurate intensity data to ca. 1.0Å resolution is available, the application of direct methods is normally straightforward and successful. Unfortunately, the difficulties associated with meeting these criteria from a powder diffraction pattern mean that in practice, the application of traditional direct methods to powder diffraction data is not suitable. That said, direct methods have been used to successfully solve crystal structures from powder data, despite the

difficulties (Altomare *et al.*, 2002, Altomare *et al.*, 2008) for example, the crystal structure of clomipramine hydrochloride. The structure of clomipramine hydrochloride is shown in Figure 1.5. It is also possible to use the technique of differential thermal expansion to obtain more accurate intensity estimates. However, this approach requires extensive experimental effort, which is not justified, given the ease with which global optimisation procedures can be used to solve the crystal structure of organic compounds.

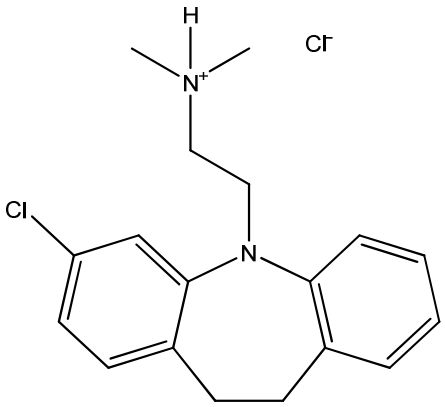

Figure 1.5 Molecular structure of clomipramine hydrochloride. Monoclinic; $P2_1/c$; a = 15.506Å, b = 8.605Å, c = 14.031Å, α = γ = 90°, β = 96.69° Z' = 1 Z = 4

1.7.2 Structure solution by global optimisation

1.7.2.1 General

Unlike the traditional Direct and Patterson methods which are routinely applied to single crystal diffraction data, global optimisation (GO) methods do not seek to identify electron density from first principles, but to match electron density with atomic positions in a trial crystal structure. This approach is particularly useful for crystal structure solution of molecular organic compounds for which it has previously been stated that the application of direct or Patterson methods are not routine. The principle advantage of global optimisation is

the fact that the limited information from the powder diffraction pattern can be supplemented by the use of prior chemical knowledge (David *et al.*, 2002) thus improving the data: parameter ratio which makes successful structure solution much more likely. One of the easiest and most convenient forms of chemical knowledge to exploit is the known molecular topology and coordination of the system under study (David *et al.*, 2002) which can be conveniently represented by a Z-matrix. Global optimisation aims to find the trial structure with the lowest possible R-factor, which corresponds to the global minimum, by optimisation of the position and orientation of the input molecular model within the unit cell.

In principle, any global optimisation method can be used to solve crystal structures from powder diffraction data, and successful structure solution has been achieved using parallel tempering (van Mechelen *et al.*, 2008, Seijas *et al.*, 2009), genetic algorithms (Harris *et al.*, 1998, Immirzi *et al.*, 2009), simulated annealing (Derollez *et al.*, 2010, Maccaroni *et al.*, 2010, Shankland *et al.*, 2002, David *et al.*, 1998) and hybrid Monte Carlo (Johnston *et al.*, 2002, Markvardsen *et al.*, 2005) approaches. Although there is a wide range of global optimisation techniques implemented in various computer programs, the global optimisation method used during the course of this work was simulated annealing, using the DASH structure solution package (David *et al.*, 2006). Therefore, only simulated annealing will be discussed further. Table 1.4 lists other computer programs which use global optimisation methods to solve crystal structures from powder diffraction data.

Table 1.4 Some computer programs used to solve crystal structures from powder diffraction data by global optimisation methods

program	GO method	reference
FOX	parallel tempering	Favre-Nicolin & Cerny, 2002
GEST	genetic algorithm	Feng & Dong, 2007
PowderSolve	simulated annealing	Engel *et al.*, 1999
TOPAS	simulated annealing	Coelho, 2000

1.7.2.2 The structural fragment

Each trial structure can be represented by a minimum number of variables which describe the position, orientation and conformation of the fragment. All fragments have six variables which describe the position and orientation of the fragment. These six variables are; x, y and z which describe the position of the fragment, and θ, ϕ and ψ which describe the orientation of the fragment. When a number, n, of torsion angles is added to the six variables describing the position and orientation, we obtain $'6 + n'$ which is also known as the degrees of freedom (DOF) in the structural fragment. For example, the diuretic drug, hydrochlorothiazide (Figure 1.6) only has one flexible torsion, resulting in a total of seven DOF.

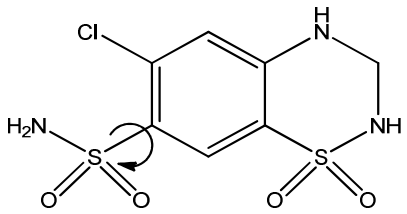

Figure 1.6 Molecular structure of hydrochlorothiazide. The arrow shows the flexible torsion angle.

However, the anti-angina drug verapamil hydrochloride (Figure 1.7) contains twenty-one DOF; three describe the position of the chloride anion, six describe the position and

orientation of the verapamil cation, and the remaining twelve describe the conformation of the verapamil cation

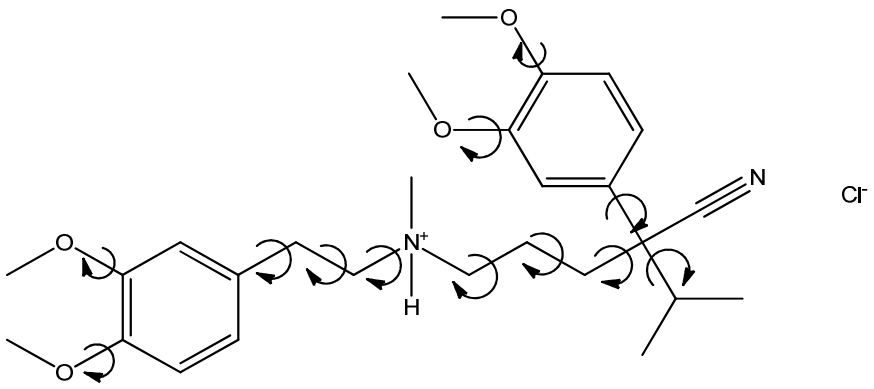

Figure 1.7 Molecular structure of verapamil hydrochloride. Flexible torsions are denoted with arrows.

1.7.2.3 The molecular Z-matrix

One straightforward way to represent the structural fragment is as a series of bond lengths, bond angles and torsion angles. Given that for most organic moieties bond lengths and angles can be accurately estimated by analysis of polymorphs or related crystal structures in the Cambridge Structure Database (CSD) (Allen, 2002), it is possible to generate a three-dimensional molecular description, where the only unknowns are the values of any torsion angles. Inserting different values for the torsion angle into the Z-matrix generates different trial structures. As an example, the input Z-matrix for the nicotinate ion (Figure 1.8) in salbutamol nicotinate is described in Table 1.5.

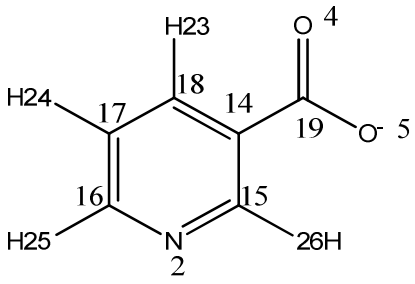

Figure 1.8 Molecular structure of the nicotinate ion showing the numbering used in Table 1.5

Table 1.5 Z-matrix description of the nicotinate ion used as an input model for structure solution of salbutamol nicotinate.

number	atom	length		angle		torsion		bond to	angle with	torsion with
14	C	0	0	0	0	0	0	0	0	0
15	C	1.42	0	0	0	0	0	14	0	0
18	C	1.39	0	116.59	0	0	0	14	15	0
19	C	1.53	0	120.63	0	177.8	0	14	15	18
2	N	1.31	0	123.59	0	3.74	0	15	14	18
23	H	0.95	0	118.14	0	179.82	0	15	14	2
17	C	1.37	0	118.70	0	-3.69	0	18	14	15
26	H	0.95	0	120.50	0	-179.72	0	18	14	17
4	O	1.23	0	118.86	0	6.57	1	19	14	15
5	O	1.27	0	117.70	0	179.58	0	19	14	4
16	C	1.30	0	118.06	0	-1.41	0	2	15	14
25	H	0.95	0	120.27	0	-178.36	0	17	18	14
24	H	0.95	0	118.31	0	179.22	0	16	2	15

In Table 1.5, the values of 0 and 1 after the length, angle and torsion columns tell us which parameters are being optimised during the structure solution attempt. In this case, only a single torsion angle (corresponding to the conformation of the carboxylate group) is being varied. Thus, the nicotinate anion in the crystal structure of salbutamol nicotinate can be described using only 7 independent variables rather than the 39 required to describe the anion if an individual atom approach were used. As a further check, the accuracy of the bond lengths and angles in the nicotinate ion were checked against similar moieties using MOGUL.

1.7.2.4 Structure solution by simulated annealing

Of all the available global optimisation methods, simulated annealing (SA) is the most commonly used for SDPD due to the ease of use of the technique (David *et al.*, 2002). In the SA technique, random trial models are generated by a Monte-Carlo procedure, by making random stepwise increments to the structural parameters being varied. The random models may yield a better fit ('downhill') or worse fit ('uphill') between the observed and calculated powder diffraction patterns. In the early stages of an SA run, it is important that uphill as well as downhill moves are allowed, since uphill moves early in the run allow the search to escape from local minima. These principles are best understood by analogy with the process of cooling a melt to form a solid. There are two routes of doing this; one route is to quench the melt, thus trapping a random atomic conformation in the form of a glass. The other route is to cool the melt slowly, in which case the system has the opportunity to fully explore the energy space and thus adopt the energetically most favourable (crystalline) conformation. In terms of SDPD, the atoms in the melt are substituted with the structural parameters of the system under study (atomic co-ordinates, bond lengths, angles and torsions) and the energy of the system is substituted for a figure of merit (χ^2) function (David *et al.*, 2002). The technique has been used to solve the crystal structures of flexible materials from powder diffraction data, ranging from poly (ethylene oxide) complexes of triflate salts (Lightfoot *et al.*, 1993) to pharmaceutical compounds such as capsaicin (David *et al.*, 1998), verapamil hydrochloride (Florence *et al.*, 2005) and benfluorex hydrochloride (Maccaroni *et al.*, 2010). The structures of capsaicin and benfluorex hydrochloride are shown in Figures 1.9 and 1.10 respectively

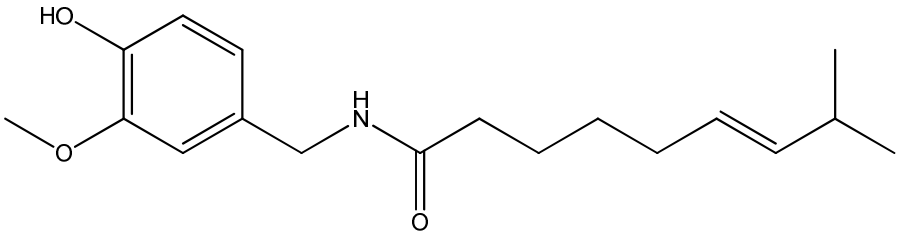

Figure 1.9 Molecular structure of capsaicin

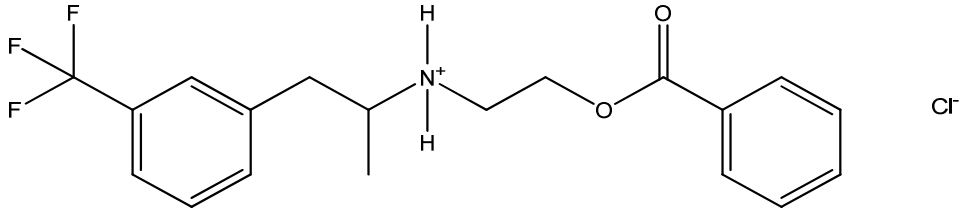

Figure 1.10 Molecular structure of benfluorex hydrochloride

Although SA is a powerful technique for SDPD, the success of this approach depends upon the complexity of the system under study (hence the challenge for the global optimisation step) and data quality available. For example, it has been shown that if data resolution is low, then the final structure obtained by SA will be much less accurate than structures solved from higher resolution data. This was clearly demonstrated from the solution of the crystal structure of famotidine form B (Shankland *et al.*, 2002). That said, collection of good data in the laboratory is more than capable of circumventing this problem.

1.8 The SDPD process

The SDPD process is a systematic sequence of events, where each step can have an influence on the outcome of subsequent steps. Therefore, it is important to give careful consideration to each step of the process in order to maximise the chances of successfully solving the crystal structure of the compound of interest accurately and reliably. The remainder of this section details the SDPD process.

1.8.1 Sample preparation and data collection

This is the first step in the process, and is perhaps the most important, since all subsequent steps depend on the ability to collect good data. Ideally, powder diffraction data should be sharp (low FWHM). In the laboratory, the best possible data can be achieved by: light grinding of the sample and rotating the capillary during data collection to help reduce PO effects; collecting the data at low temperature to obtain more accurate intensity data at high angle (provided, of course, that the sample does not undergo a phase transition at low temperatures) the optimum data can be collected using a laboratory equipped with a primary monochromator and a position sensitive detector (PSD) and the spatial resolution in the dataset should be ca. 2.5Å or better. Recrystallisation of the sample can help to sharpen the powder diffraction pattern, and collecting data out to ca. 40-50° 2θ provides sufficient spatial resolution for SDPD attempts using CuKα_1 radiation. Data should also be collected using monochromatic radiation, with the instrument operating in Debye-Scherrer geometry. It is convenient to collect two datasets from a sample of interest. The first is a long-count (typically 8 seconds per step) for good signal: noise at low angles to see weak peaks essential for pattern indexing. The second pattern collected is a variable count time (VCT) dataset to

approx. 70° 2θ (1.5Å resolution). This second pattern is required for Rietveld refinement where the maximum possible information is required from the experimental powder diffraction pattern.

1.8.2 Powder pattern indexing

The next step is indexing of the powder diffraction pattern to determine the unit cell parameters, crystal system and space group of the material via the observed peak positions. Assuming high quality powder diffraction data has been collected, there are several indexing programs which can be used to index the pattern, such as; DICVOL (Boultif & Louer, 1991), DICVOL06 (Louer & Boultif, 2007), TREOR (Werner *et al.*, 1985), N-TREOR09 (Altomare *et al.*, 2009), X-cell (Neumann, 2002). However, sometimes indexing attempts fail, which ends the SDPD process, as indexing is a crucial step, so without success at this point structure solution is impossible. However, there are a wide range of methods which can be tried when the more traditional indexing methods fail. For example, singular-value decomposition (SVD) has been shown to be effective when the data is noisy or when the unit cell is large (Coelho, 2003). Also, the presence of impurities or the presence of severe peak overlap in the powder diffraction pattern can also have a negative impact on indexing attempts, but should indexing attempts fail due to severe overlap or impurities, the problem may be overcome by: recollecting the data at a different temperature, recollecting the data using a longer count time, using a narrower capillary or recrystallisation the sample

1.8.3 Space group determination

Having determined the unit cell parameters and crystal system, the next step is to determine the space group. The principle of this is comparison of systematic absences in the diffraction data. This can be done manually, by comparing the diffraction data with the calculated reflection positions generated from the unit cell parameters and each of the space group symbols in the assigned crystal system. This approach is, however, tedious and can be error prone; particularly in the case of orthorhombic systems where the number of possible space groups is large. A much more reliable way of determining the space the space group is to use a probabilistic method, such as the method implemented within DASH (Markvardsen *et al.*, 2001).

1.8.4 Pawley refinement

The next step in the process involves fitting the powder diffraction to extract individual intensities associated with each reflection. As has been stated previously, the reflections in a powder diffraction pattern are often overlapped, especially at high angle. Therefore, a robust method of extracting intensities from overlapped reflections is required. Intensity extraction is carried out by carrying out a Pawley fit (Pawley, 1981) in DASH, but other methods are also useful for intensity extraction, and the Le Bail method is also popular (Le Bail, 1980). Pawley refinement is a model independent refinement, in which the unit cell, zero point, background, peak shape and the extracted intensities are refined. Overlapped peaks tend to be equipartitioned across the corresponding reflection

1.8.5 Model building

Having successfully indexed the powder diffraction pattern, determined the correct space group and extracted individual intensities from the powder pattern, the stage is set for structure solution. To maximise the chances of successfully solving the crystal structure of the material of interest, it is imperative that an accurate input model is used for SA. If the material under study is a polymorph, salt, solvate or co-crystal of a compound with a known crystal structure, the best input model to use is a modified (renumbered, X-ray normalised) crystal structure, since the molecular geometry of the input model has been verified. The molecular geometry can be checked for any 'unusual' parameters by carrying out a MOGUL check, which compares all parameters (bond lengths and angles to those of similar fragments in the CSD (Bruno *et al.*, 2002) and altering the values of any unusual parameters to lie within normal ranges.

If the compound under study does not have a known crystal structure, then obtaining the best possible input model is a bit more challenging. One possible method of obtaining a good input model is to alter the crystal structure of a close structural analogue. For example, there is no published crystal structure for bromocresol green, but the crystal structure of a very close analogue, bromophenol blue, has been published, with the CSD reference code CEKNEL (Veerapandian *et al.*, 1984). The structures of bromophenol blue and bromocresol green are shown in Figures 1.11 and 1.12 respectively.

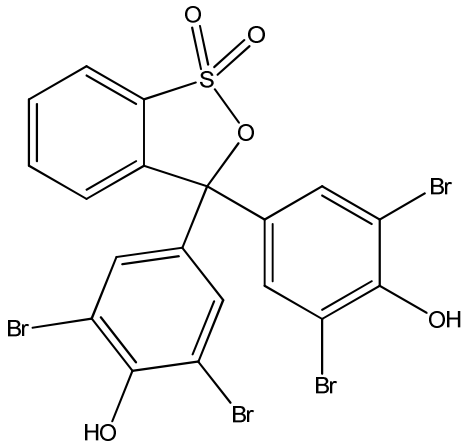

Figure 1.11 Molecular structure of bromophenol blue

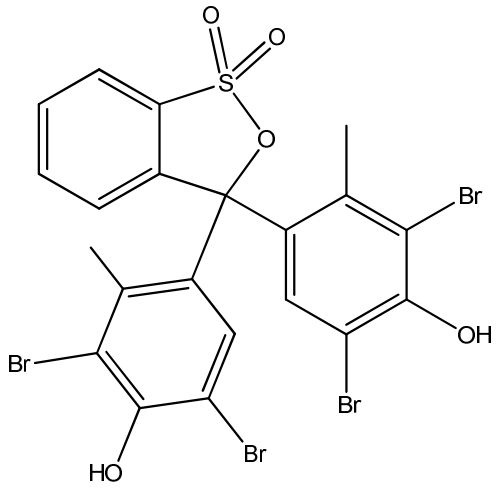

Figure 1.12 Molecular structure of bromocresol green. Monoclinic; C2/c a = 32.921Å b = 9.289Å c = 14.892Å, $\alpha = \gamma = 90°$ $\beta = 94.665°$ Z' = 1, Z = 8 (unpublished work)

An accurate input model for bromocresol green can readily be prepared by manually adding methyl groups and phenolic hydrogen atoms to the dibromophenol moieties, followed by normalisation of the C-H and O-H bond lengths to the values of 0.95Å and 0.9Å respectively, and correcting any unusual geometric parameters flagged up by a MOGUL geometry check. This can be readily implemented using Mercury CSD 2.0 (Macrae *et al.*, 2008).

If it is not possible to alter the crystal structure of a similar compound to obtain an input model, a possible option is to use an energy optimised input model. For example, there is no known crystal structure for the tocolytic drug ritodrine hydrochloride, and it is not straightforward to simply edit an analogous crystal structure to obtain an input model. The molecular structure of ritodrine hydrochloride is shown in Figure 1.13.

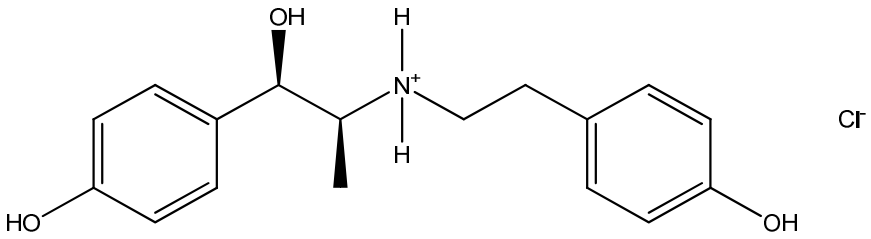

Figure 1.13 Molecular structure of ritodrine hydrochloride. Orthorhombic; Pbca a = 11.265Å b = 8.272Å c = 31.356Å $\alpha = \beta = \gamma = 90°$ Z' = 1, Z = 8 (unpublished work)

An input model for the ritodrine cation can, however be obtained by carrying out geometry optimisation of the freebase, then manually protonating the base and making the appropriate corrections for ionisation, guided by CSD searches for similar structural fragments. There are several options available for generating geometry optimised input models such as; semi-empirical methods (Stewart, 1990).

1.8.6 Simulated annealing structure solution

Having decided on the optimum verified input model, the next step is to optimise the model against the observed powder diffraction data. The exact cooling regimen used depends upon the complexity of the system under study. The crystal structures of small, rigid molecules,

such as hydrochlorothiazide can easily be solved using relatively fast cooling rates. However, if the molecule of interest is conformationally flexible, as is the case with the antibiotic chloramphenicol palmitate (CP, Figure 1.14), then the chances of successfully solving the crystal structure are greatly increased if the cooling rate is decreased, and/or the starting temperature is increased, this allowis a much more thorough search of the space and increasing the chances of successfully locating the global minimum in the hypersurface.

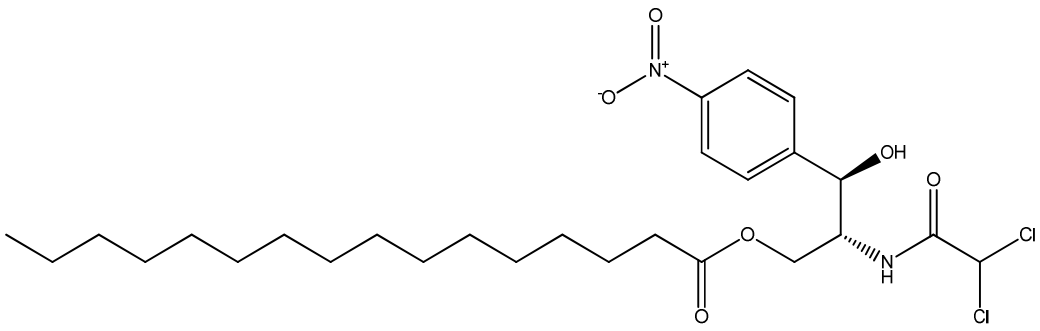

Figure 1.14 Molecular structure of chloramphenicol palmitate. Orthorhombic; $P2_12_12_1$ a = 7.805Å b = 52.503Å c = 7.414Å $\alpha = \beta = \gamma = 90°$ Z' = 1 Z = 4

In addition to altering the cooling rate or starting temperature, the search for the global minimum can be simplified by the use of modal constraints during the simulated annealing runs (Bruno *et al.*, 2004). Modal constraints do not reduce the total DOF in the structure solution attempt, but they do restrict the space searched during the runs, rather than searching the 360° that need to be searched if the runs are carried out unconstrained. For example, a C – C bond in an alkyl chain typically has a bimodal distribution around 180° as shown in Figure X. A crystal structure can be considered solved if the ratio $\chi^2_{profile} : \chi^2_{Pawley}$ is less than 10 (Florence *et al.,* 2005). Structures with ratios higher than 10 may also be essentially correct, but there may be other factors to take into account. For example, the structure may be

disordered, or preferred orientation may need to be taken into account, but the structure may otherwise make good sense.

1.8.7 Rietveld refinement

In a Rietveld refinement the structural and profile parameters are varied in a least squares refinement to yield the best possible fit to the experimental powder diffraction data (Rietveld, 1969). To that end, Rietveld refinement can be viewed as a method of increasing the accuracy of the final crystal structure from simulated annealing. Given the limited data available from a powder diffraction pattern, it is not normally possible to refine a crystal structure totally unconstrained. If there are a large number of structural parameters, the data-parameter ratio can be improved by carrying out a restrained Rietveld refinement, where bond lengths and angles are allowed to vary within a defined range (applying prior chemical knowledge) and the isotropic temperature factors of equivalent atom types (e.g. non-hydrogen atoms) are set to be equivalent.

Another method of carrying out a Rietveld refinement is to carry out a rigid body Rietveld refinement. The aim of rigid body Rietveld refinement is to further reduce the structural parameters which are to be varied during the refinement process, thus further improving the data-parameter ratio and consequently the accuracy of the final structure. The structural parameters can be reduced by treating the molecular fragments as a rigid body in which the bond lengths and angles do not vary. This is reasonable, because many organic compounds have rigid moieties in their structures (Kaduk, 2007). For example, fixing the bond lengths and angles in an aromatic ring to 1.39Å and 120° respectively reduces the number of parameters which must be varied in the Rietveld refinement. Any variation in restrained

Rietveld refinement against lab data are not reflecting actual changes in the fine detail in the chemical structure or bonding. This approach has been demonstrated successfully in the refinement of the crystal structure of the expectorant guaifenesin which was solved from powder diffraction data (Kaduk, 2007). The structure of guaifenesin is shown in Figure 1.15.

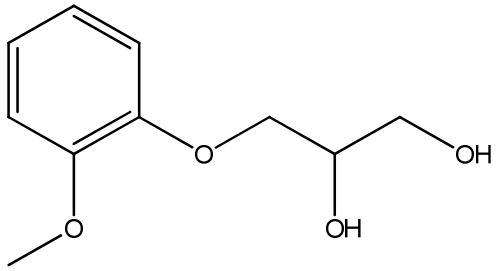

Figure 1.15 Molecular structure of guaifenesin. Orthorhombic; $P2_12_12_1$ a = 7.657Å b = 25.670Å c = 4.979Å $\alpha = \beta = \gamma = 90$ Z' = 1, Z = 4

During the refinement of the guaifenesin crystal structure, only the values of the torsion angles in the flexible side chain were allowed to vary, thus reducing the number of structural parameters. During a rigid body refinement, typically the only parameters being varied are; the background parameters, the scale factor, 3 parameters describing the position of each structural fragment, 3 parameters describing the orientation of each structural fragment, the values of any flexible torsion angles in the structure and the non-hydrogen isotropic temperature factor (ITF). Given the fact that the objective of Rietveld refinement is to accurately locate the global minimum on the χ^2 hypersurface, it is important to assess how well the structure fits the observed experimental data. There are several indicators of the quality of the crystal structure including; statistical (R_{wp}), graphical (fit to the experimental data) and chemical sense.

1.8.8 Crystal structure verification

1.8.8.1 Interactions and molecular geometry

Since the aim of SDPD is to obtain accurate crystal structures in the absence of a suitable single sample, it is important to confirm that the structures returned from SA and Rietveld refinement do indeed make good chemical sense. The first, and perhaps most obvious, verification procedure is to make sure that all hydrogen bond donors at acceptors are satisfied and that the molecular geometry makes sense, by comparison with similar structural fragments . The hydrogen atoms attached to the hydrogen bond donors may not point exactly at the acceptor, due to the difficulties in accurately locating hydrogen atoms using X-rays, but the interactions should nevertheless make good sense.

1.8.8.2 Unconstrained refinement

If the crystal structure has been solved successfully, the molecular geometry should be reasonably well conserved if all of the atom positions are allowed to vary in an unconstrained Rietveld refinement. The structure may distort, but the connectivity (excluding the hydrogen atoms) should still make good chemical sense.

1.8.8.3 DFT analysis of the structure

Another step in the structure verification process can be to carry out Density Functional Theory (DFT) calculations to confirm that the χ^2 minimum against the diffraction data is also an energy minimum. The accuracy of the location of the heavy atom positions in a crystal structure solved from powder diffraction is often excellent. However, the precise location of hydrogen atoms is much more difficult, given the low contribution of hydrogen atoms to the

scattering from the entire structure. If it is absolutely essential to obtain accurate hydrogen atom positions, then neutron diffraction experiments can be carried out, as this method allows the accurate location of hydrogen atoms directly from the diffraction data. If the positions of the hydrogen atoms in the structure are not of vital importance, DFT calculations can be used to locate the positions of the hydrogen atoms much more accurately than SA structure solution alone. This was demonstrated by the location of the hydrogen atoms in the sulphonamide group in hydrochlorothiazide form II by DFT calculation (Florence *et al.*, 2009) using CASTEP (Clark *et al.*, 2005)

1.9 Study of amorphous structure

1.9.1 General

It has already been said that there is growing interest in the development of X-ray amorphous dose forms of drugs, particularly for drugs where the solubility and bioavailability are low. The problem is, when the long range order associated with the crystalline state breaks down, as is the case with amorphous or nanocrystalline materials, traditional powder diffraction techniques cannot be used to characterise the material, due to the lack of Bragg diffraction from the sample. Instead, a characteristic broad amorphous 'halo' is observed. A typical amorphous halo is shown in Figure 1.16.

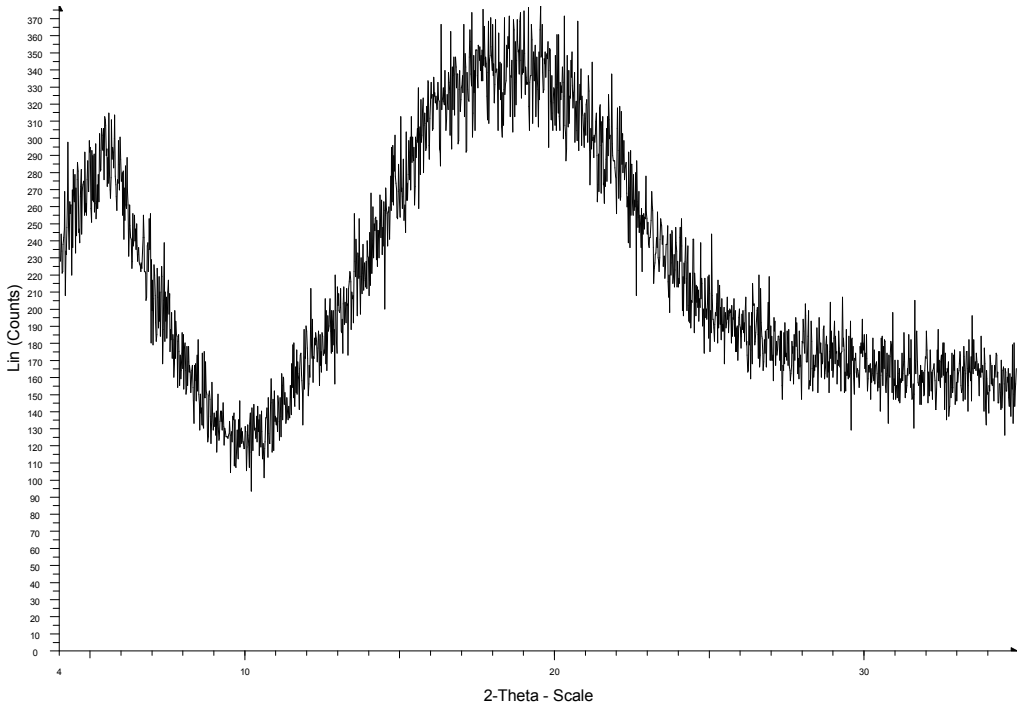

Figure 1.16 X-ray amorphous halo collected from a sample of anhydrous raffinose

Although powder diffraction is of limited use in the laboratory for the characterisation of X-ray amorphous materials, there are several techniques that can be used to characterise the samples at the macroscopic level; thermal and spectroscopic techniques have been used to characterise X-ray amorphous systems for some time, and both approaches will be discussed in the following sections.

1.9.2 Thermal analysis of amorphous pharmaceuticals

A characteristic of X-ray amorphous solids is the tendency for recrystallisation, given the thermodynamic instability of the amorphous state. Prior to recrystallisation, the molecules in the amorphous solid must begin to re-orientate and re-order themselves. This happens at the glass transition temperature (T_g), above which there is sufficient molecular mobility to allow spontaneous recrystallisation. Knowledge of the glass transition temperature and

crystallisation temperature (T_c) are important for the development of amorphous dose forms, since it is essential to prevent recrystallisation as far as practicable. Differential Scanning Calorimetry (DSC) measurements are a very useful method of determining the T_g and T_c for an amorphous pharmaceutical compound (Bhugra *et al.*, 2008, Feth *et al.*, 2008, Zhou *et al.*, 2008).

1.9.3 Spectroscopic analysis of amorphous pharmaceuticals

Spectroscopic methods such as FTIR, ATR and Raman are powerful methods for studying structural changes in the sample and have been used extensively to study changes in hydrogen bonding and other molecular interactions in the samples. For example, FTIR has been used to study structural differences between the crystalline and amorphous states of the structurally related analgesic drugs celecoxib, valdecoxib, rofecoxib and etoricoxib (Kaushal *et al.*, 2008). Amorphous drugs are often formulated as molecular dispersions of the amorphous drug with a pharmaceutically acceptable hydrophilic polymer, such as polyvinylpyrrolidone (PVP). The polymer increases the T_g and consequently the T_c of the amorphous drug, whilst increasing the wetability. Spectroscopic techniques are useful for studying the drug-polymer interactions in such systems (Taylor & Zografi, 1997a, Taylor & Zografi, 1997b, Tobyn *et al.*, 2009, Fini *et al.*, 2008, Patel & Patel, 2008, Xu *et al.*, 2007).

1.9.4 Total scattering and PDF analysis

A very useful approach which is becoming more widely used is total scattering coupled with PDF analysis, which has been widely applied to liquids and amorphous materials. Total scattering refers to the fact that all structure relevant scattering from a sample is collected

(Bragg and diffuse scattering) over a wide range of reciprocal space where coherent scattering exists (Billinge, 2008). The PDF is obtained when the corrected, normalised total scattering signal is Fourier transformed to real space.

The atomic PDF, or G(r) is defined as shown in equation 1.5, where ρ(r) is the atomic pair density, ρ_0 is the average atomic number density and r is the radial distance

$$G(r) = 4\pi r[\rho(r) - \rho_0] \qquad 1.5$$

The PDF yields the probability of finding pairs of atoms separated by distance r. It is obtained by a sine Fourier transformation of the reciprocal space total scattering structure function, S(Q), according to equation 1.6.

$$G(r) = \frac{2}{\pi}\int_0^\infty Q[S(Q) - 1]\sin Qr dQ \qquad 1.6$$

Where S(Q) is the corrected, normalised diffracted intensity from the sample, and Q is the scattering vector, which is calculated as shown in equation 1.7, where λ is the radiation wavelength.

$$Q = (4\pi \sin\theta)/\lambda \qquad 1.7$$

It is important to collect data over a wide Q-range. Low real-space resolution, which is a consequence of measurements made over a limited Q-range is often good enough for glasses and liquids. For more structured, nanocrystalline materials, there are definite advantages of having the best real-space resolution possible, and Q-ranges up to Q_{max} values of 30-50Å^{-1} are desirable, but this requires either neutrons or short wavelength X-rays. Neutrons have a natural advantage, due to the fact that there is no intensity fall-off at high Q, but the high flux which is available at synchrotron sources is more than able to compensate for intensity loss at high angle.

In the PDF, the peak position corresponds to a bond length or atom-atom spacing (assuming that an atom pair can be assigned). The peak width corresponds to thermal motion and any static disorder which may be present. The intensity is a measure of the multiplicity and type of atoms involved in the bond (Billinge, 2008). The technique has been widely applied to nanocrystalline inorganic systems in order to solve crystal structure at the nanoscale (Billinge *et al.*, 2005, Petkov *et al.*, 2000, Shatnawi *et al.*, 2007) but less success has been reported for molecular organic compounds. PDF analysis has been carried out on X-ray amorphous organic compounds, including pharmaceutically relevant compounds (Bates *et al.*, 2007, Bates *et al.*, 2006, Newman *et al.*, 2008), but in these cases, PDF analysis was a 'fingerprinting' technique to confirm miscibility of amorphous drug-polymer dispersions (Newman *et al.*, 2008), or to assess the validity of calculated crystal structures for the unstable compound raffinose trihydrate (Bates *et al.*, 2007). However, more recently, the PDF method was applied to the analgesic and anti-epileptic drug, carbamazepine, and structural characterisation of this drug at the nanoscale was accomplished (Billinge *et al.*, 2010).

1.10 Summary

The following experimental chapters will explore SDPD of pharmaceutically relevant samples using an SA approach and verification that the experimental structures are indeed correct. The benefits and disadvantages of synchrotron vs. laboratory X-ray powder diffraction will be discussed in detail, and significant challenges for SDPD using laboratory data and an SA approach will be discussed. Finally, structure solution of nanocrystalline materials using a PDF approach will be discussed.

Chapter 2

Aims and Objectives

2.1 Aims

The principal aim of this project is to investigate crystal structure determination from laboratory X-ray and synchrotron powder diffraction data. Within this context, particular emphasis is placed on structural complexity. This includes *ab initio* structure determination of pharmaceutical salts and co-crystals, as well as a systematic study of the limits of structural complexity that can be solved by global optimisation methods. The project also aims to characterise X-ray amorphous materials using a total scattering PDF approach using synchrotron and laboratory TS-PDF data.

2.2 Objectives

Pharmaceutically acceptable co-crystals of the anti-epileptic drug carbamazepine (CBZ) will be prepared by published methods. The co-crystals will be characterised in the laboratory, then selected co-crystals will be examined on the high-resolution powder diffraction beamline (beamline I11) at Diamond Light Source (DLS) in Oxfordshire.

Structural complexity will be further increased by the preparation of several pharmaceutically acceptable salts of the β_2 adrenoceptor agonist salbutamol. The salts will range from small carboxylic acid through to fatty acid and bile acid salts, which corresponds to a systematic increase in structural complexity in the salbutamol system. The salts will be prepared by a number of different methods; solution crystallisation, manual grinding, mechanical grinding, crystallisation from the amorphous and crystallisation by the use of a suitable anti-solvent. The crystal structures of these salts will be solved directly from X-ray powder diffraction data (XRPD) and subsequently refined by rigid body Rietveld refinement. The application of density functional theory (DFT) calculation to structure verification will then be assessed

X-ray amorphous, nanocrystalline samples of pharmaceutical compounds will be examined at beamline ID-11-B at the Advanced Photon Source (APS) at Argonne National Laboratory, Argonne, Illinois using a Total Scattering Pair Distribution Function (TS-PDF) approach. The compounds of interest are CBZ and the non-steroidal anti-inflammatory drug (NSAID) indomethacin (IND). All known polymorphs of the drugs will also be characterised as crystalline reference samples. Drug amorphisation by melting then quenching in liquid nitrogen and thermal characterisation will be carried out in the laboratory to provide a baseline characterisation. Recrystallisation kinetics will also be studied in the laboratory prior to carrying out experiments at beamline ID-11-B to assess the stability of the amorphous materials. Due to the thermodynamic instability of the amorphous state, X-ray amorphous samples will be prepared at the beamline immediately before analysis. The resultant data will be used to assess structural similarity (of the local packing) with known crystalline forms i.e. for structural fingerprinting of the X-ray amorphous samples.

Chapter 3

Materials and methods

3.1 Materials

The materials used in the experimental work are listed in Table 3.1. All compounds except indomethacin and salbutamol were obtained from Sigma Aldrich Poole, UK. Indomethacin was obtained from Roig Farma, Barcelona, Spain. Salbutamol was obtained from Ind. Chimica Farmaceutica Italiana, Bergamo, Italy. The molecular structures of the compounds are shown throughout the experimental chapters

Table 3.1 Compound names and molecular formulae for the compounds throughout the experimental chapters

Compound	Molecular formula
acetic acid	$C_2H_4O_2$
butyric acid	$C_4H_8O_2$
benzoic acid	$C_7H_6O_2$
camphoric acid	$C_{10}H_{16}O_4$
capric acid	$C_{10}H_{20}O_2$
carbamazepine	$C_{15}H_{12}N_2O$
formic acid	CH_2O_2
glycolic acid	$C_2H_4O_3$
1-hydroxy-2-naphthoic acid	$C_{11}H_8O_3$
indomethacin	$C_{19}H_{16}ClO_4$
lauric acid	$C_{12}H_{24}O_2$
maleic acid	$C_4H_4O_4$
nicotinic acid	$C_6H_5NO_2$
oxalic acid	$C_2H_2O_4$
saccharin	$C_7H_5NO_3S$
salbutamol	$C_{13}H_{21}NO_3$
salicylic acid	$C_7H_6O_3$
stearic acid	$C_{18}H_{36}O_2$

3.2 Methods

3.2.1 Laboratory XRPD

To maximise the chances of successfully and accurately solving a crystal structure from laboratory XRPD data, it is essential that the following requirements are addressed: accurate measurement of reflection positions and intensities, high angular resolution (small FWHM), high spatial resolution (≈2Å or better), good signal-to-noise ratio across the entire pattern and minimal preferred orientation (PO) effects. These criteria are all best achieved by mounting the sample in a rotating capillary, and collecting the data in transmission mode using monochromated radiation. Such a setup was used in the laboratory, and the instrument configuration is shown in Table 3.2.

Table 3.2 Instrument configuration for laboratory XRPD experiments

Instrument configuration	
System	D8 Advance θ/2θ
Generator	50kV, 40mA
Measuring diameter	435mm
Radiation	Cu Kα1 λ = 1.54056Å
Monochromator	primary, focusing curved Ge 111
Geometry	Transmission
Sample mount	borosilicate glass or Kapton capillaries
Detector	Bruker Lynxeye
Alignment sample	NIST SRM 640c Si

3.2.2 Synchrotron powder diffraction

3.2.2.1 Beamline I11 at DLS

Samples were lightly ground and packed into 1.0mm borosilicate glass capillaries. The capillaries were mounted in the diffractometer using a magnetic holder, and the capillaries were rotated during the data collection. Data were collected at 298 and 150K using X-rays of wavelength 0.82628Å. Low temperature was achieved using a cryostream device using liquid nitrogen. Data were collected using 5 MAC (multiple analyser crystal) detector arms, containing 9 Si 111 analyser crystals, thus 45 powder patterns were collected simultaneously, drastically speeding up data collection time.

3.2.2.2 Beamline ID-11-B at APS

Beamline ID11-B at APS is used for TSPDF experiments. The beamline was set up to allow to RA-PDF (rapid acquisition PDF) experiments to be carried out. Samples were sealed in 1 mm diameter kapton capillaries and irradiated with x-rays of wavelength = 0.1370 Å. A large area 2D image plate detector (MAR345) was placed centered on and perpendicular to the incident beam 198 mm behind the sample. The short wavelength was necessary to obtain data over a sufficiently high *Q*-range, which is necessary to get sufficiently good resolution in real-space. To obtain sufficient statistics in the high-*Q* range multiple exposures of the image plate were made, exposing for 300 s, between 5 and 8 times for each data-point. The separate exposures were summed together before further processing, resulting in an integrated exposure time of 30 minutes per sample.

Under these conditions data were obtained that could be reliably used up to a Q_{max} = 20 $^{o}A^{-1}$ 1D powder diffraction pattern was obtained by integrating around the Scherrer rings in the

images from the image plate, correcting for beam polarization effects. All samples were initially examined at 100K. Crystallisation of the amorphous samples was induced by heating the samples using a Cryostream device

3.2.3 Standard Structure Solution Sequence (SSSS)

Having collected powder diffraction data, the next steps are structure solution and refinement. In order to make SDPD truly routine, it is important to adopt a standard method of structure solution to maximise the chances of success for each structure. Indexing, space group determination, Pawley refinement, simulated annealing and Rietveld refinement have all been incorporated into a standard workflow sequence and will be discussed below.

3.2.3.1 Pattern indexing and space group determination

Powder patterns were indexed using DICVOL06 (Louer & Boultif, 2007) implemented in DASH. This procedure allowed the unit cell parameters and crystal system to be determined. The space group was then determined using a probabilistic method (Markvardsen *et al.*, 2001). Unit cell parameters and space groups were confirmed by also indexing the powder pattern in TOPAS 4.1 (Coelho, 2003). Indexing in TOPAS was also useful when DICVOL calculation times were long, as is often the case with triclinic crystal structures. Confidence in the unit cell parameters was greatly increased by using two different indexing methods to obtain the same (or very similar) unit cell parameters. After indexing, the unit cell parameters were converted to the conventional setting in PLATON (Spek, 2003). Also, the unit cell and space group settings were confirmed by consideration of molecular volumes of fragments

3.2.3.2 Pawley refinement

The next step in the structure solution process is to fit the powder diffraction pattern to allow the extraction of individual integrated intensities associated with each reflection. This can be difficult due to the high degree of peak overlap in a powder diffraction pattern, thus a robust method of dealing with the overlap is required. The Pawley method (Pawley, 1981) is used in DASH. Individual peaks were selected in the powder pattern, to provide a set of non-overlapped ("single crystal") intensities for structure solution. Pawley fitting was also carried out in TOPAS to assess the fit to the unit cell parameters to the experimental data. Pawley fitting in TOPAS uses an ASCII input ("inp") file. The refined profile and unit cell data are easily viewed in the corresponding output (".out") file.

3.2.3.3 Model building and Z-matrix preparation

The chances of finding the correct conformation of the structure of interest by chance are vanishingly small. In order to maximise the chances of successfully solving the crystal structure of the material of interest using a simulated annealing approach, it is therefore important to use the most accurate input model possible. The most accurate input models are prepared by obtaining accurate bond lengths and bond angles for the system under study. The conformation of the structure cannot be determined a *priori* and is found by the SA method.

The input models for the carbamazepine co-crystals were ab initio gas phase optimised, using the program Gaussian. The level of theory used to generate the models was MP2 631-G (d,p). Models for optimisation were obtained from the CSD. In the case of the salbutamol salts, the input models were derived from structures in the CSD. The crystal structure of salbutamol hemisulphate is known, (CSD refcode SALBUT) but the structure contains disorder. The crystal structure of salbutamol base (CSD refcode BHHPHE) was therefore chosen as the starting model for the salbutamol cation. The salbutamol cation input model was prepared by

manually adding a proton to the amine group of salbutamol in Mercury. The resulting cation was then subjected to a geometry check in Mogul (ref), and it was found that the new model had 'unusual' geometric parameters, namely; a shorter than expected C-N bond (1.464Å) and a wider than expected C-C-N angle (112.93°). These abnormalities in the model were due to the fact that changes in these parameters due to ionisation had not been taken into account. Table 3.3 shows the average C-N bond length and C-C-N angle for similar neutral and ionised compounds obtained in Mogul.

Table 3.3 Mean values for the amine and ammonium portions in structures chemically similar to salbutamol

ionisation state	C-N bond length	C-C-N angle
amine	1.453 Å	110.671°
ammonium	1.498 Å	109.469°

The C-H, O-H and N-H bond distances in all of the input models were set to the X-ray normalised values of 0.95Å, 0.9Å and 0.9Å respectively. Z-matrices describing the molecular connectivity were then automatically created by importing the model into DASH. The Z-matrix for the salbutamol cation was updated to take into ionisation into account. As a final adjustment, the C-C-C angles of the tert butyl group of salbutamol were changed to the value of 109° to more accurately reflect the geometry of this moiety. The C –C –C angle does not vary during simulated annealing, so in order to get the most accurate crystal structure, it is essential that the input model is as chemically accurate as possible. The final modification was to give each atom in the structural fragments a unique atom label. The Z-matrices were then used for simulated annealing.

3.2.3.4 Simulated annealing structure solution

Simulated annealing runs were carried out in batch mode using either GDASH (Griffin *et al.*, 2009a) or MDASH (Griffin *et al.*, 2009b). Batches of runs carried out using GDASH consisted of 800 runs, with 25 million moves per run. Batches of runs carried out using MDASH consisted of 20 runs. The cooling rate during the simulated annealing runs was typically 0.01K, due to the relative complexity of the materials under study. Modal constraints for flexible torsion angle were applied via MOGUL (Bruno *et al.*, 2004) to reduce the search space during the simulated annealing runs

3.2.3.5 Rigid body Rietveld refinement

As has been stated previously, Rietveld refinement of the model is carried out to obtain the best possible fit between the structural model and the diffraction data. It has also been said previously that rigid-body Rietveld refinement is a powerful method for further reducing the parameters which must be varied during the refinement, consequently improving the data: parameter ratio whilst still retaining chemical sense in the model. All of the crystal structures solved during this work were refined by rigid body Rietveld refinement.

3.2.3.5.1 Preparation of the rigid bodies

The input Z-matrices for simulated annealing were updated so that the values of any flexible torsion angles matched the values in the best crystal structure returned from the simulated annealing step. The altered Z-matrices were then converted to the TOPAS rigid body format ".rgd" using jEdit v4.2. The atomic labels in the rigid body were appended with a "Z" label to make it easier to differentiate the rigid body atoms from the real atoms in the structure. An example of a ".rgd" file is shown in Table 3.4

Table 3.4 An example of a .rgd file for rigid-body Rietveld refinement in TOPA

```
 rigid
z_matrix C14Z
z_matrix C15Z  C14Z     1.5042982
z_matrix H23Z  C14Z     0.9499708   C15Z   109.556102
z_matrix H25Z  C14Z     0.9500263   C15Z   109.808805  H23Z  -116.950904
z_matrix H24Z  C14Z     0.9499667   C15Z   107.898362  H23Z   124.358139
z_matrix O4Z   C15Z     1.2572487   C14Z   117.093897  H23Z    73.792774
z_matrix O5Z   C15Z     1.2389144   C14Z   118.618126  O4Z   -177.446553
```

The rigid bodies were then included in the "inp" file for Rietveld refinement, in which the position and orientation of the rigid bodies, background parameters, scale factor, non-hydrogen ITF and any flexible torsion angles were allowed to refine. A TOPAS rigid-body Rietveld refinement ".inp " file is shown in Appendix 2.

3.2.3.5.2 Unconstrained Rietveld refinement

After the Rietveld refinement has been completed, a good check that the structure is correct is to allow all of the atomic positions to refine freely. This is done by flagging the "macro ref_flag" for refinement, but deleting all of the definitions after the coordinate block in the inp file. If the structure is indeed correct, the geometry is typically well conserved. The fit to the data will improve, but the hydrogen atom geometry is lost. However, the non-hydrogen atoms retain their connectivity (although there may be some movement in these atoms) which confirms that the structure is at a minimum.

3.2.3.5.3 DFT calculations

First-principles DFT calculations were performed on the experimental SDPD structures using CASTEP v.4.3 and v.5.0 using the materials studio interface. The unit cell parameters and space group symmetry were fixed at the experimental values for all calculations for better computational efficiency and because DFT does not deal with dispersion forces accurately. A generalised gradient approximation, Perdew-Burke-Ernzerhof functional (GGA-PBE) was used to describe the exchange-correlation potential, with a plane-wave basis set cut-off of 435eV. Medium convergence criteria, tolerances of energy, maximum force and maximum displacements were 2.0×10^{-5} eV/atom, 0.05eV/Å and 2.0×10^{-3} Å respectively. Ultrasoft pseudopotentials were used for core electrons to allow the calculations to be carried out at the lowest possible cut-off energy for the plane wave basis set. DFT calculations were also used to assist with the Rietveld refinement of the structures, particularly for the accurate location of the hydrogen atoms, which cannot be reliably done using X-ray data alone, so relevant torsion angles were read from the CASTEP optimised structures and input into the rigid body. Although the difference this made to the final fit was small, the structural model made

much more sense due to the chemically correct hydrogen bond interactions. Excluding the hydrogen atom positions, a given structure was considered to be at a minimum if the CASTEP calculations successfully converged, and there were no significant movements in the heavy atom positions following CASTEP calculation (i.e. the experimental crystal structure and the CASTEP optimised structure are superimposable).

Chapter 4

Crystal structures of pharmaceutically acceptable carbamazepine co-crystals solved from synchrotron and laboratory X-ray powder diffraction data

4.1 Introduction

Many pharmaceuticals contain either an amine or carboxylic acid functional group in the molecule. In these cases, it is relatively simple to screen for crystalline salts, which can increase the solubility of the parent drug. However, it is becoming increasingly common for poorly soluble, weakly or non-ionisable compounds to be screened for biological activity during high throughput screening experiments (HTS) (Lipinski *et al.*, 2001). The practice of dissolving such compounds in DMSO means that such compounds do interact with the receptor of interest during the HTS experiments, and some extremely poorly soluble compounds can show excellent *in vitro* activity, but very poor *in vivo* activity due to the poor water solubility of the compound (Bak *et al.*, 2008).

An area of intense research in the pharmaceutical industry to circumvent the problems associated with poor solubility of an API is the concept of co-crystal formation. Pharmaceutical co-crystals are typically formed by crystallising the API from solution in the presence of a suitable co-crystal former. The co-crystal formers must be pharmaceutically acceptable, and range from acids and bases typically used to screen for salt formation, to food additives. The co-crystals formed by the above method often have unique physicochemical and biopharmaceutical characteristics, and it has been shown that the formation of pharmaceutical co-crystals can lead to vastly improved plasma concentrations of poorly soluble drugs *in vivo*. (Hickey *et al.*, 2007, McNamara *et al.*, 2006, Bak *et al.*, 2008). There is no guarantee that a co-crystal will form, but the chances of forming a co-crystal can be maximised by using a crystal engineering approach (Vishweshwar *et al.*, 2005, Blagden *et al.*, 2007, Basavoju *et al.*, 2008). That is, taking advantage of the hydrogen bond donors and acceptors in the pharmaceutical molecule, and choosing co-crystal formers which have

complementary hydrogen bonding groups. Co-crystals designed in this manner are held together by supramolecular synthons, which are purely non-bonded interactions between hydrogen bond donors and acceptors.

The well-established analgesic and anti-epileptic drug carbamazepine (CBZ) is a poorly soluble, non-ionisable drug. CBZ has been extensively studied in the solid state, and crystal structures of 4 polymorphs and several solvates and co-crystals have been deposited in the CSD.

This compound is an excellent model for co-crystal formation; the carboxamide group is un-ionisable, so it is impossible to form a CBZ salt. Also, the molecule possesses both hydrogen bond donors and acceptors, which are essential for synthon formation. Indeed, CBZ has been shown to form co-crystals with a number of different classes of co-crystal formers, such as carboxylic acids, quinones, sulfimides and carboxamides. The synthons formed between CBZ and the various classes of co-crystal formers are shown in Figure 4.1 (Fleischman *et al.*, 2003, Hickey *et al.*, 2007). It has also been shown that the saccharin co-crystal of CBZ can result in higher plasma concentrations of the drug when compared with the marketed drug (Hickey *et al.*, 2007).

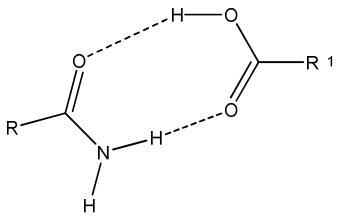

1

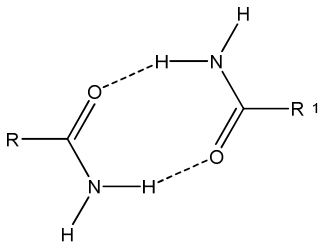

2

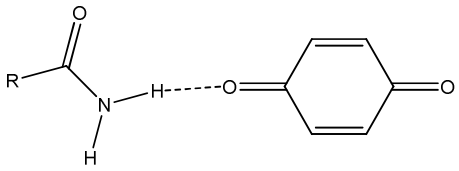

3

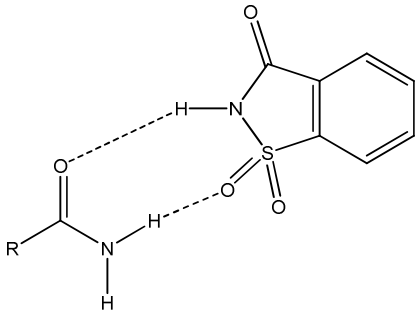

4

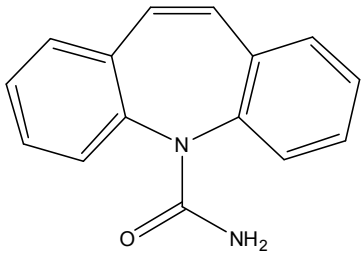

CBZ

Figure 4.1 Supramolecular synthons observed in CBZ co-crystals. 1 = carboxamide-carboxyl synthon. 2 = carboxamide-carboxamide synthon. 3 = carboxamide-quinone synthon. 4 = carboxamide-sulfimide synthon. In the above Figure, R = 5H-dibenzo[b,f]azepine ring system and R^1 is an organic residue. In the case of carboxamide-quinone and carboxamide-sulfimide synthons, the only known examples for CBZ are the CBZ-benzoquinone co-crystal and the CBZ-saccharin co-crystal.

A co-crystal screen involving CBZ and pharmaceutically acceptable carboxylic acids resulted in the formation of several novel co-crystals the formation of which was confirmed by XRPD, Raman spectroscopy and DSC data (Childs *et al.*, 2008). At the time this work was carried out, no crystal structures had been published for any of the CBZ co-crystals.

Samples of six of the co-crystals were prepared for SDPD attempts, four of which were prepared specifically to assess the capabilities of the newly commissioned high-resolution beamline (beamline I11) at Diamond Light Source (DLS). The co-crystals prepared for the SDPD attempts were; CBZ: 1-hydroxy-2-naphthoic acid (CBZ:HNA), CBZ: (+)-camphoric acid (CBZ:CAM), CBZ: oxalic acid (CBZ:OXA), CBZ: glycolic acid (CBZ:GLY) CBZ: benzoic acid (CBZ:BEN) and CBZ: salicylic acid (CBZ:SAL). The samples of CBZ: BEN and CBZ: SAL were examined in the laboratory only, the other co-crystals were examined in the laboratory and at beamline I11 (see §4.4). However, whilst work was ongoing on preparing the crystal structures of the CBZ co-crystals solved from powder diffraction data for publication, the single crystal structures of these co-crystals were published (Childs *et al.*, 2009).

4.2 Diamond Light Source (DLS)

Diamond light source in Oxfordshire is the UK national synchrotron facility. DLS is a third generation synchrotron radiation source. In third generation synchrotron radiation sources, the incident radiation beam is attenuated by the use of insertion devices (multipole wigglers or undulators) which offer significant advantages in the quality and nature of the data obtained. The Materials Science Beamline (X04SA) at the Swiss Light Source (SLS) and the high resolution powder diffraction beamline (ID31) at the European Synchrotron Radiation

Facility (ESRF) make use of such devices, and provide X-ray beams of brightness and incident flux at the sample that is 2-3 orders of magnitude higher than at older synchrotron sources (Thompson *et al.*, 2009). High brightness is essential to achieve the highest possible *d*-spacing resolution which is extremely useful for accurate indexing of the unit cell.

Previously, a major disadvantage in performing powder diffraction experiments at a synchrotron source was the long experimental time required to scan a large angular range (in 2θ) using small steps. These long experimental times significantly increase the risk of radiation damage to the sample under investigation. However, a solution to this problem is the use of multiple crystals located systematically in the scattering plane (Thompson *et al.*, 2009). There are two basic designs for such a set up; (i) multiaxis instruments with one crystal mounted on each axial assembly distributed around the 2θ circle and (ii) single-axis instruments with a multianalysing crystal (MAC) assembly with a fixed, prealigned angular offset between each crystal. Beamline I11 uses a hybrid of the above designs combining the intensity recovery characteristics of the MAC concept with the short angular scan range of the multiple axis approach. The hybrid approach gives high resolution diffraction data with high peak-to-background ratios with short data collection times and high sample throughput. Beamline I11 became operational in 2009 (Thompson *et al.*, 2009), and since then several organic (Brandao-Neto *et al.*, 2010), inorganic (Kellici *et al.*, 2010) and organometallic (Mowat *et al.*, 2009, Stylianou *et al.*, 2010) compounds have been examined on the beamline, but, at the time of the experiment, the CBZ co-crystals were the first organic pharmaceutically relevant samples to be examined on the beamline.

4.3 Preparation of polycrystalline materials

All of the co-crystals except the CBZ:GLY co-crystal were prepared from solution according to a previously published method (Childs *et al.*, 2008). The CBZ: GLY co-crystal was prepared by "reaction crystallisation" where a filtered, saturated solution of GLY was saturated with CBZ. The CBZ: GLY co-crystal was the least soluble compound in this system, and precipitated from solution.

4.4 X-ray powder diffraction

4.4.1 Laboratory X-ray powder diffraction

Samples were lightly ground and packed into 0.7 mm borosilicate glass capillaries. Data were then collected as described in §3.2.1. In the case of CBZ: HNA and CBZ: CAM, laboratory data were collected to confirm the purity of the co-crystal samples and to assess the quality of the diffraction data. However, in the case of CBZ: BEN and CBZ: SAL, good quality laboratory XRPD data was required for structure solution.

4.4.2 Synchrotron X-ray powder diffraction

Samples were lightly ground and packed into 1.0 mm borosilicate glass capillaries. Data were then collected as described in § 3.2.2. This data was used for structure solution attempts.

4.5 Indexing and choice of space group

The powder diffraction patterns (both laboratory and synchrotron) were indexed in DASH, using DICVOL06. The first 21 peaks in the diffraction patterns were used for indexing. The space group for each co-crystal was tentatively assigned using a probabilistic method, and confirmed by successful Pawley refinement of the unit cell parameters in the chosen space

group. As a further check, indexing was also carried out using TOPAS 4.1 to confirm that the unit cell parameters and space group were correct. The unit cell parameters were transformed to the standard setting and a final Pawley refinement was then carried out in preparation for structure solution.

4.6 Thermal analysis

Finely ground samples of the co-crystals (ca. 5mg) were added to 25µl aluminium DSC pans. The pans were sealed with a pierced lid. Samples of CBZ: HNA and CBZ: CAM co-crystal were heated under a nitrogen purge from 20°C - 250°C at a rate of 10K min^{-1}. At beamline I11, samples of CBZ:HNA and CBZ:CAM co-crystal were examined at 150K and at 298K. No new peaks were observed in the powder diffraction patterns on cooling the samples, which showed that no polymorph transitions occurred upon cooling the samples. A sample of CBZ: BEN co-crystal was heated from -50°C - 200° to confirm that no low temperature polymorph transitions are observed in the co-crystal. A sample of CBZ: SAL co-crystal was heated from -50°C - 250°C in order to confirm that no low temperature polymorph transitions are observed in the co-crystal. The DSC runs were ended at different temperatures (i.e. 200 and 250°C) because the samples tended to decompose, and the end temperature was chosen to avoid potentially damaging the DSC instrument by allowing compounds to decompose in the instrument.

4.7 Model building and Z-matrix preparation

Molecular models of CBZ and each of the co-crystal formers were prepared using an *ab initio* approach in the Gaussian molecular modelling software (as described in §3.2.3.3). The level of theory used to generate these models was 6-31G (d,p). This gave accurate models of most

of the compounds, but in CAM, one of the carboxyl groups was in the wrong conformation relative to the single crystal structure (CSD refcode HUSVOG). It was, however possible to correct this by altering the molecular Z-matrix. The C-H, O-H and N-H bond lengths were normalised to X-ray values of 0.95Å, 0.9Å and 0.9Å respectively. Molecular Z-matrices were generated automatically in DASH.

4.8 Simulated annealing structure solution

Simulated annealing was carried out using the program GDASH (Griffin *et al.*, 2009a) which allowed large numbers of simulated annealing runs to be carried out overnight. MOGUL was used to constrain the torsional search space during the simulated annealing. The simulated annealing protocol is shown in Table 4.1

Table 4.1 Simulated annealing protocol for CBZ co-crystals

N_{runs}	moves per run	cooling rate	χ^2 multiplier
800	$2.5x10^7$	0.01K	1

The best crystal structures for each batch of simulated annealing runs were checked in Mercury to confirm that there were no bad contacts (unusually short or chemically nonsensical contacts) and that the molecular conformation of each structural fragment was acceptable. After these checks had been carried out, the structures were subjected to rigid-body Rietveld refinement.

4.9 Rigid-body Rietveld refinement

Rigid body descriptors of the structural fragments were derived from the input Z-matrices, but with the values of the flexible torsions updated to match the experimental values exactly. These torsion angles were then refined along with the background, scale factor, position, orientation and non-hydrogen isotropic temperature factor (ITF).

4.10 Density functional theory (DFT) calculations

DFT calculations were carried out on the refined crystal structures, to confirm that the molecular conformation was correct and to lend confidence that the global minimum had been reached.

4.11 Results

4.11.1 Indexing results

Four of the co-crystals were indexed successfully. The unit cell parameters returned from indexing in DICVOL06 are shown in Table 4.2.

Table 4.2 Results from indexing the powder data in DICVOL06

Co-crystal	a (Å)	b (Å)	c (Å)	α°	β°	γ°	V (Å^3)	$M_{(21)}$	$F_{(21)}$
CBZ:HNA	16.69	5.13	24.58	90	99.27	90	2075.38	56.1	295.5
CBZ:CAM	12.58	13.14	14.47	90	105.7	90	2303.88	25.4	155.2
CBZ:BEN	28.74	5.22	24.82	90	103.4	90	3623.68	5.6	16.3
CBZ:SAL	5.19	19.85	18.35	90	97.9	90	1872.24	13.8	42.2

As can be seen from the above table, the majority of the co-crystals could be indexed convincingly, the only exception being the CBZ:BEN co-crystal, which had the lowest figures of merit from indexing attempts. Nevertheless the unit cell parameters were successfully obtained from powder data. The advantage of synchrotron radiation vs. laboratory X-rays is clear from Table 4.2, where confidence in the unit cell parameters is much higher for the co-crystals examined on beamline I11 (CBZ:HNA and CBZ: CAM) than for those examined in the laboratory (CBZ: BEN and CBZ: SAL).

4.11.2 Results from simulated annealing structure solution

With the exception of CBZ: CAM, the CBZ co-crystals represent the mid-point of complexity that can be routinely tackled using a simulated annealing approach (Florence *et al.*, 2005). The CBZ: CAM co-crystal represents a significant challenge for simulated annealing, but it

has been shown that more complex structures can be solved from powder diffraction data using simulated annealing (Fernandes *et al.*, 2007). The results of the simulated annealing runs are summarised in Table 4.3.

Table 4.3 Results of simulated annealing runs for CBZ co-crystals

Co-crystal	Pawley χ^2	Profile χ^2 range	Z'	N_{solved} [a]	$\%_{solved}$ [b]	Total DOF
CBZ:HNA	5.47	11.35-160.85	1	638	79.75	14
CBZ:CAM	3.57	13.13-105.94	2	58	7.25	30
CBZ:BEN	14.53	33.99-598.06	1	787	98.38	14
CBZ:SAL	9.75	29.68-381.75	1	769	96.13	14

[a]In the above table, N_{solved} was determined by the sum of the structures where the ratio $\chi^2_{profile}/\chi^2_{Pawley}$ is less than 10.[b] $\%_{solved}$ is this number expressed as a percentage of the total number of runs.

Unsurprisingly, the CBZ: CAM co-crystal, which had the highest total DOF was the structure which was most difficult to solve, and even with the application of MOGUL constraints, the success rate was very low due to the increased complexity of the search. However the improved data quality in the synchrotron dataset undoubtedly helped in the structure solution attempt due to increased angular and spatial resolution in the data and more accurate intensity estimates when compared to laboratory data.

4.11.3 CBZ: OXA and CBZ: GLY co-crystals

Although samples of CBZ: OXA and CBZ: GLY were successfully prepared, it was not possible to index these powder patterns. Data collected in the laboratory were extremely broad with extensive, which made indexing impossible, and when the samples were examined on beamline I11, there was evidence of radiation damage; new peaks appeared in the powder patterns, and there was significant peak shift and peak broadening, all of which is

consistent with radiation damage. Figure 4.2 shows the radiation damage that occurred to a sample of CBZ: GLY during data collection. For comparison, data collected in the laboratory, using CuKα_1 radiation is included. The differences between the diffraction datasets is strong evidence of radiation damage, which is a problem that organic, light atom materials are prone to when exposed to high energy radiation produced at synchrotron radiation sources.

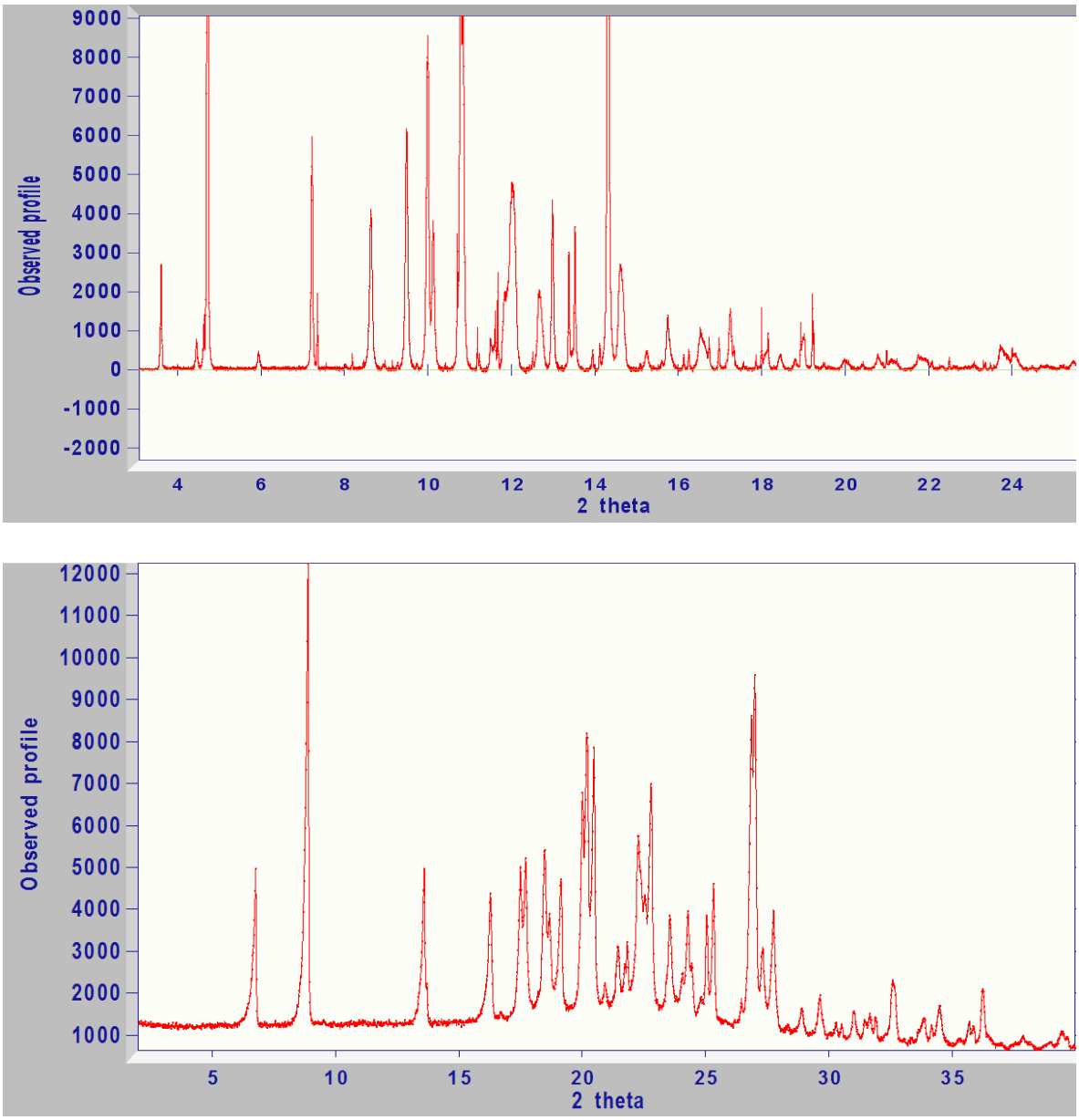

.**Figure 4.2** Evidence of radiation damage to a sample of CBZ: GLY co-crystal. Top: XRPD data collected from a sample of CBZ:GLY co-crystal on beamline I11 at DLS. Bottom: XRPD data collected from a sample of CBZ:GLY co-crystal on a laboratory powder

diffractometer. The appearance of several weak reflections, peak splitting and peak broadening, particularly in the range 10-12° 2θ in the synchrotron dataset are all indicators of potential radiation damage.

4.11.4 Thermal analysis results

All of the co-crystals prepared for these powder studies displayed a single endotherm corresponding to melting of the co-crystal, with no other thermal events (desolvation, polymorph transitions) observed. The melting points of each of the co-crystals were very close to the reported melting points for the co-crystals (Childs *et al.,* 2008). The DSC traces for the CBZ co-crystals can be found in Appendix 3. Table 4.4 shows the observed and reported melting points of each of the CBZ co-crystals.

Table 4.4 Melting points of the CBZ co-crystals

co-crystal	observed melting point (°C)	reported melting point (°C) [a]
CBZ: HNA	173.8	173.6
CBZ: CAM	156.4	156.1
CBZ: BEN	112.7	112.5
CBZ: SAL	160.1	159.2

[a] These melting points are the melting points quoted in Childs *et al.,* 2008 where the co-crystals were first reported.

4.11.5 The crystal structures of the CBZ co-crystals

All of the CBZ co-crystals are formed by hydrogen bonding between the carboxyl group of the co-crystal former and the amide group in the form of robust $R_2^2(8)$ heterosynthons. The CBZ: CAM and CBZ: SAL co-crystals also form structurally important $D_1^1(2)$ interactions.

4.11.5.1 CBZ: 1-hydroxy-2-naphthoic acid (CBZ: HNA) co-crystal

The asymmetric unit contains one CBZ molecule and one HNA molecule. The molecules in the asymmetric unit form a robust $R_2^2(8)$ heterosynthon (Etter *et al.*, 1990) between the carboxyl and amide groups. Additionally, HNA forms a $D_1^1(2)$ intramolecular hydrogen bonded interaction between the hydroxyl group and the carbonyl oxygen of the carboxyl group. The hydrogen bonding interactions in the CBZ: HNA co-crystal are shown in Figure 4.3.

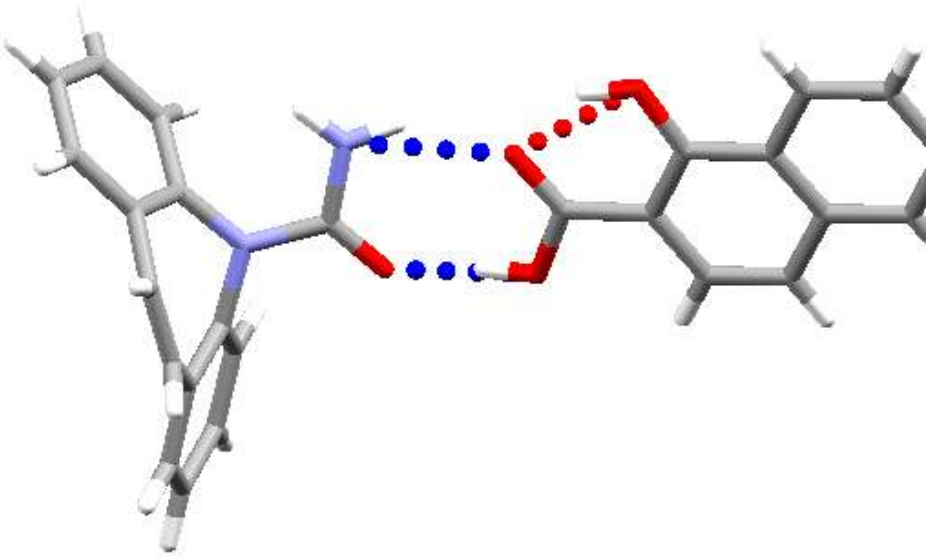

Figure 4.3 The hydrogen bonding interactions in the CBZ: HNA co-crystal. The blue dashed lines show the $R_2^2(8)$ heterosynthon (Etter *et al.,* 1990). The red dashed line shows the $D_1^1(2)$ intramolecular hydrogen bond, but this bond is not important in forming the co-crystal.

The unit cell of the CBZ: HNA co-crystal contains 4 CBZ molecules and 4 HNA molecules. The packing in the unit cell results in formation of "translation stack" motifs between the CBZ molecules (Childs *et al.,* 2009). Translation stack motifs are one-dimensional (rod) motifs. A packing diagram of CBZ: HNA co-crystal is shown in Figure 4.4.

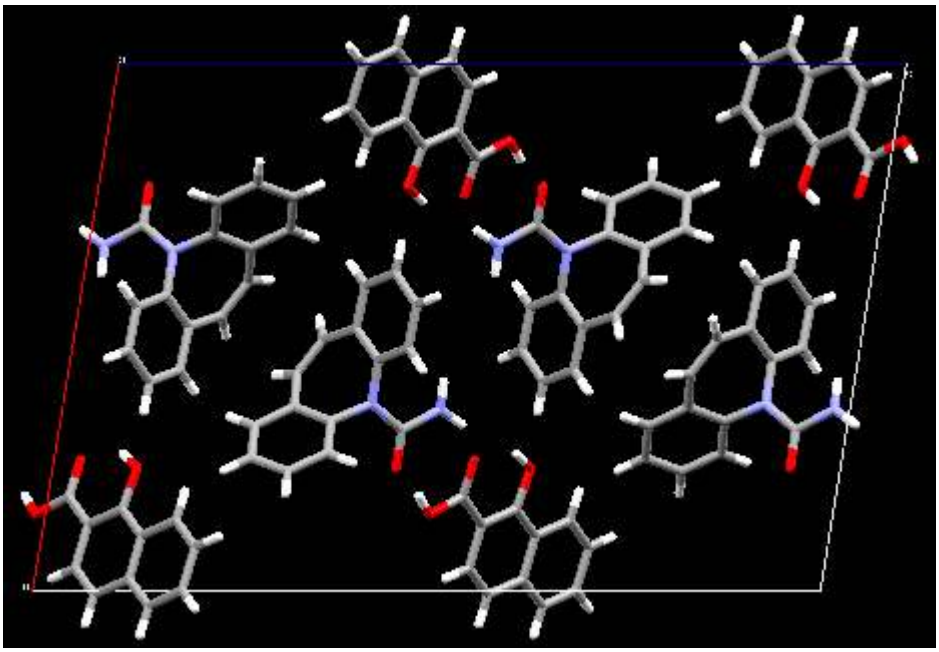

Figure 4.4 Packing diagram for CBZ: HNA co-crystal showing the formation of a translation stack between the CBZ molecules in the unit cell. The view is along the b axis.

In addition to the hydrogen bonding interactions between the amide and carboxyl groups, the structure is further stabilised by short (2.893Å) C-H...C interactions between phenyl rings of adjacent CBZ molecules and short (2.701Å) C-H...O interactions between the phenyl ring of CBZ and the carbonyl oxygen atom of HNA.

An excellent fit to the data was achieved after rigid-body Rietveld refinement. The Rietveld plot is shown in Figure 4.5

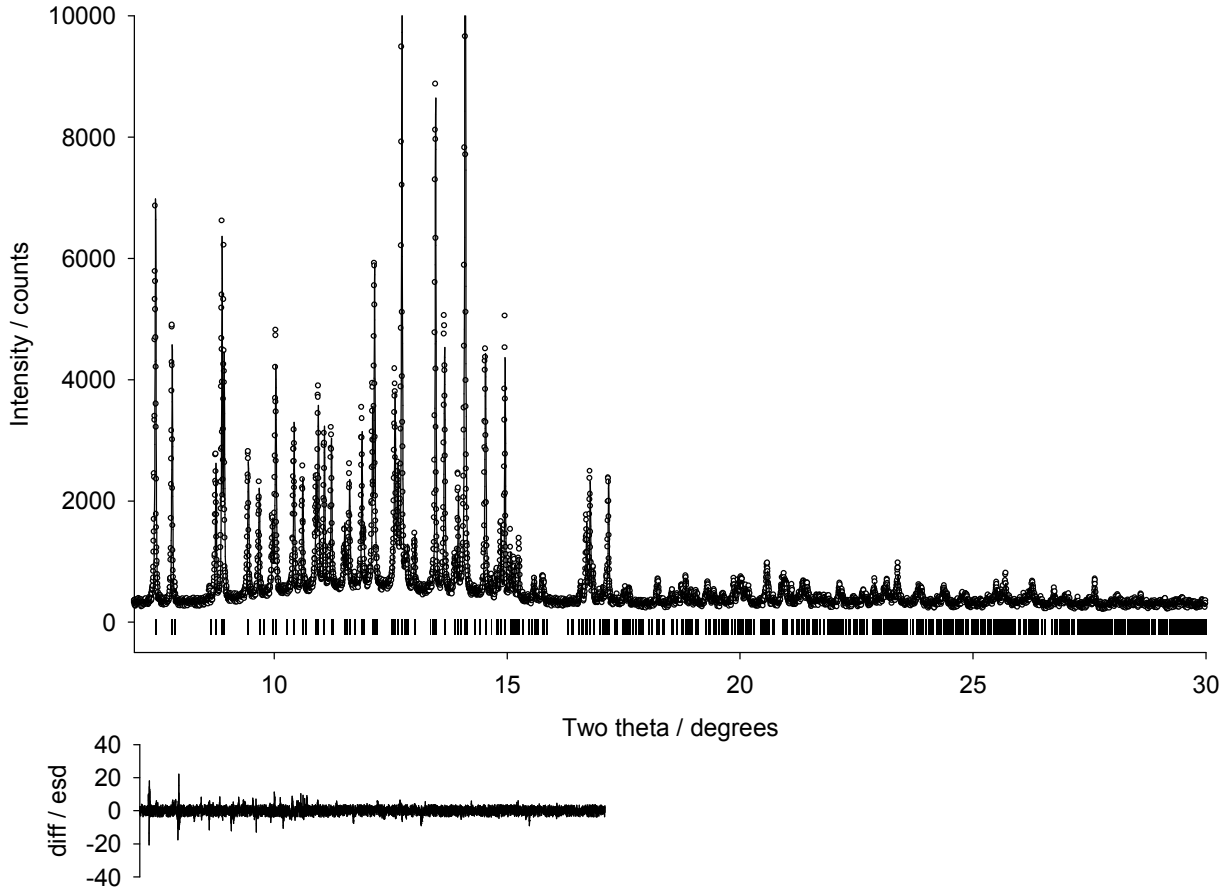

Figure 4.5 Observed profile (circles), calculated profile (line) and difference [(y_{obs} – y_{calc})/σ(y_{calc}) plot for the rigid body Rietveld refinement of the CBZ: HNA co-crystal from data collected on beamline ID11 at DLS. The final R_{wp} for this structure is 8.825.

4.11.5.2 CBZ: (+)-camphoric acid (CBZ: CAM) co-crystal

The asymmetric unit contains two CBZ molecules and two CAM molecules. Being a dicarboxylic acid, CAM forms a $R_2^2(8)$ heterosynthon with CBZ with one carboxyl group, and an $R_2^2(8)$ homosynthon with a carboxyl group in an adjacent CAM molecule. This pattern is propagated by formation of $D_1^1(2)$ interactions between the NH_2 group of CBZ and the CAM: CAM homosynthon. The hydrogen bonded interactions in the CBZ: CAM co-crystal are shown in Figure 4.6

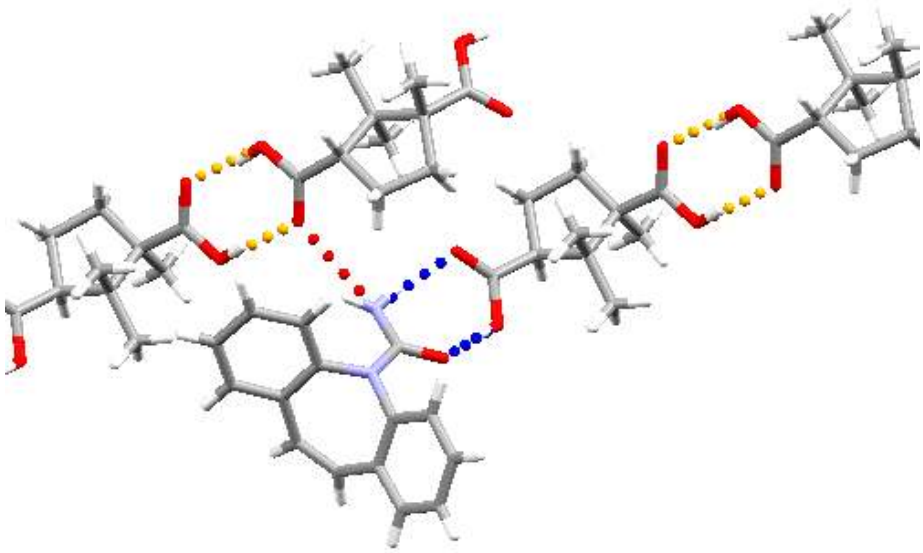

Figure 4.6 Hydrogen bonding interactions in the CBZ: CAM co-crystal. Blue lines show the $R_2^2(8)$ heterosynthon, orange lines show the $R_2^2(8)$ homosynthon and the red line shows the $D_1^1(2)$ interaction.

The unit cell of the CBZ: CAM co-crystal contains 4 CBZ molecules and 4 CAM molecules. The packing in the unit cell results in formation of "inversion cup" motifs between the CBZ molecules. Inversion cups are dimer motifs. Figure 4.7 shows the packing of CBZ: CAM co-crystal, showing the inversion cup motif in the co-crystal.

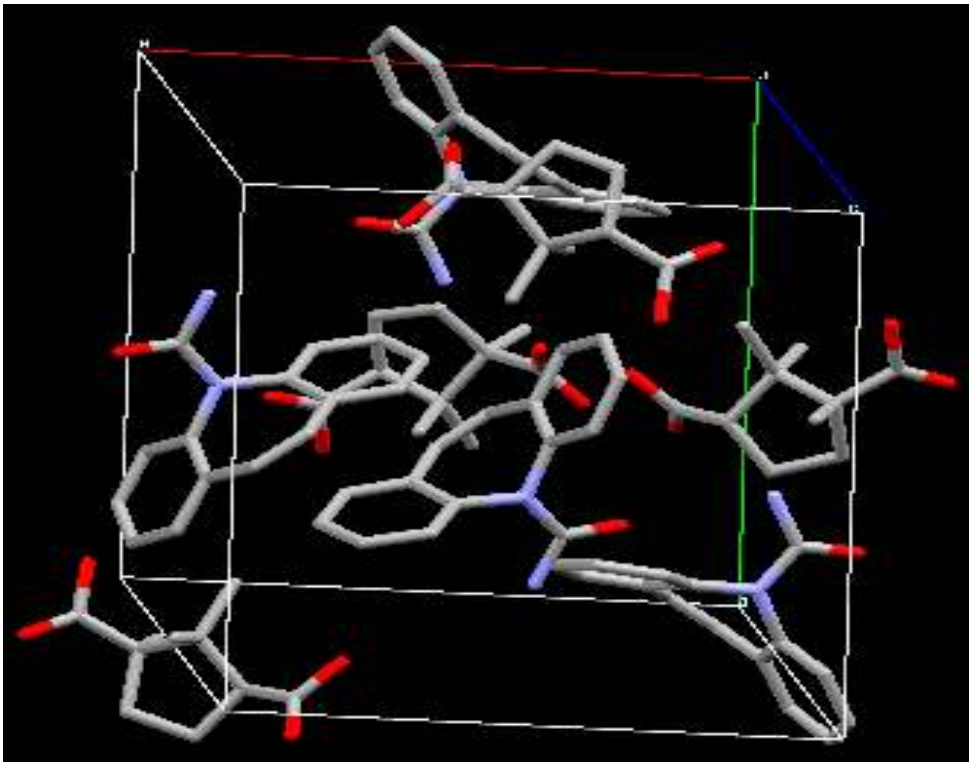

Figure 4.7 Packing diagram for CBZ: CAM co-crystal showing the formation of an inversion cup motif between the CBZ molecules. The view has been orientated to highlight the formation of the inversion cup. Hydrogen atoms have been omitted for clarity.

An excellent fit to the data was obtained after rigid-body Rietveld refinement. The Rietveld plot is shown in Figure 4.8

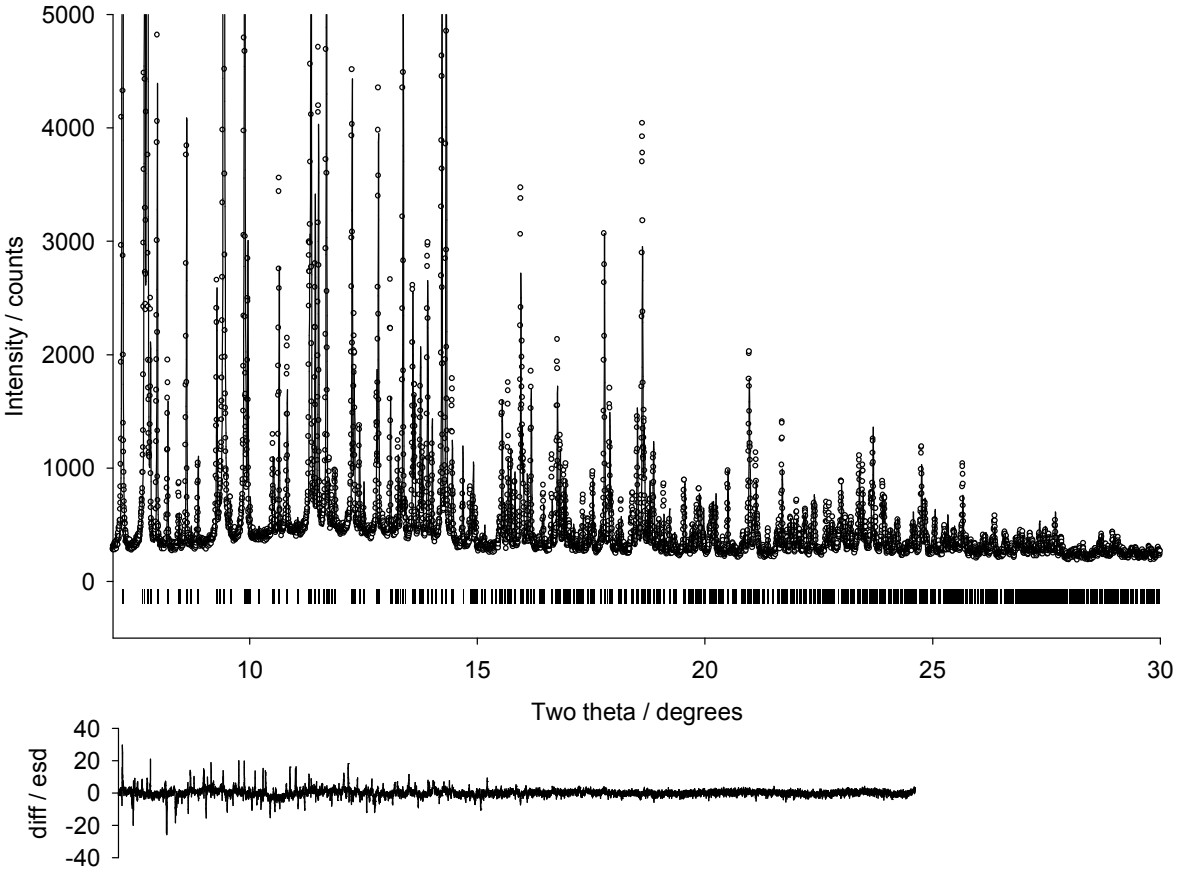

Figure 4.8 Observed profile (circles), calculated profile (line) and difference [(y_{obs} − y_{calc})/σ(y_{calc}) plot for the rigid body Rietveld refinement of the CBZ: CAM co-crystal from data collected on beamline ID11 at DLS. The final R_{wp} for this structure is 5.262

4.11.5.3 CBZ: benzoic acid (CBZ: BEN) co-crystal

The asymmetric unit contains one CBZ molecule and one BEN molecule. The molecules in the asymmetric unit form a robust $R_2^2(8)$ heterosynthon between the carboxyl and amide groups, as shown in Figure 4.9

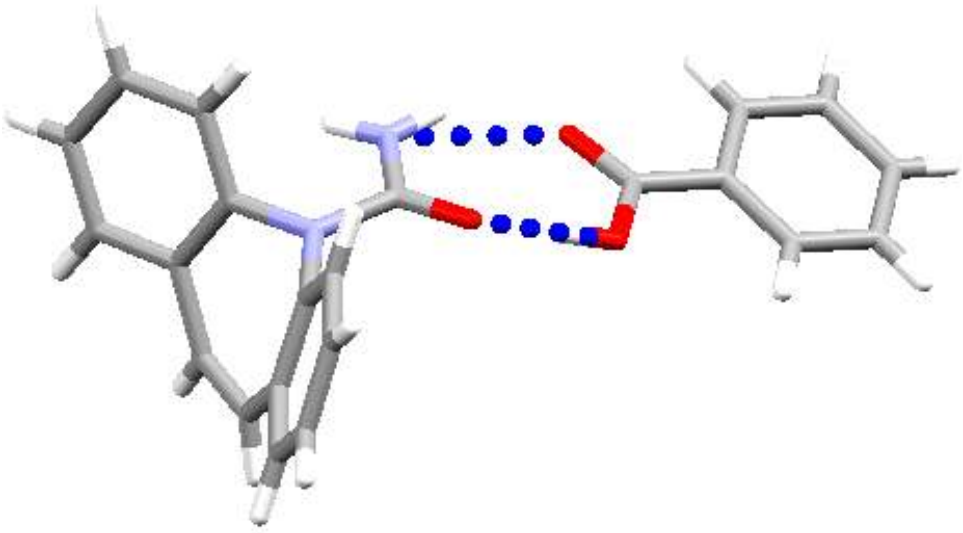

Figure 4.9 Hydrogen bonding in the CBZ: BEN co-crystal the blue dashed lines show the formation of a $R_2^2(8)$ heterosynthon in the co-crystal.

The unit cell of the CBZ: BEN co-crystal contains 8 CBZ molecules and 8 BEN molecules. The packing in the unit cell results in formation of translation stack motifs between the CBZ molecules. The translation stack motifs observed in the CBZ: BEN co-crystal are identical to those observed in the CBZ: HNA co-crystal. A packing diagram of the CBZ: BEN co-crystal is shown in Figure 4.10

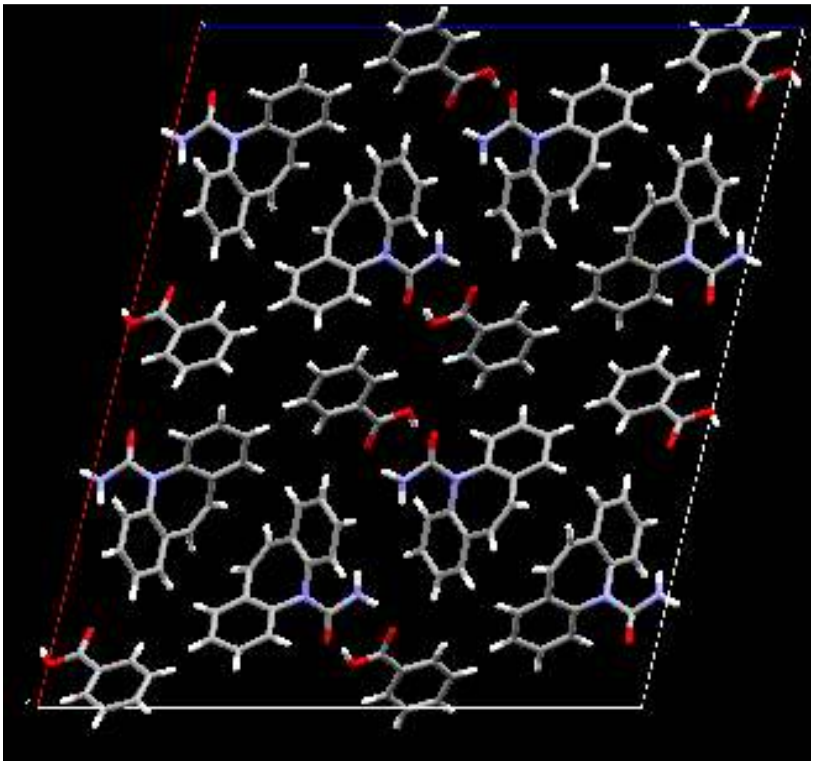

Figure 4.10 Packing diagram for CBZ: BEN co-crystal showing the formation of a translation stack between the CBZ molecules in the unit cell. The view is along the b axis.

In addition to the hydrogen bonding interactions between the amide and carboxyl groups, the structure is further stabilised by short (2.840Å) C-H...C interactions between phenyl rings of adjacent CBZ molecules, short (2.867Å) N-H...C interactions between the phenyl ring of CBZ and the NH_2 of adjacent CBZ molecules and short (2.681Å) C-H...O interactions between the phenyl ring of BEN and the carbonyl oxygen atom of CBZ.

A reasonable fit to the data was obtained after rigid-body Rietveld refinement. The Rietveld plot is shown in Figure 4.11. The R_{wp} for this structure is 6.075

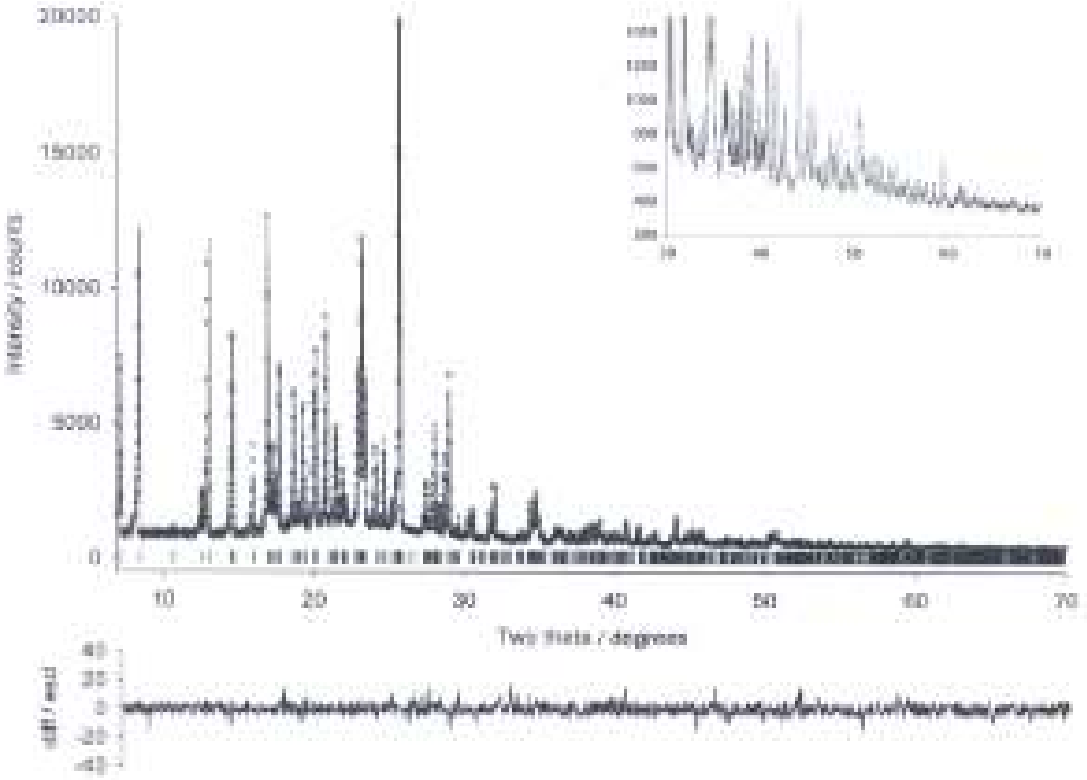

Figure 4.11 Observed profile (circles), calculated profile (line) and difference [(y_{obs} − y_{calc})/σ(y_{calc}) plot for the rigid body Rietveld refinement of the CBZ: BEN co-crystal from data collected on a laboratory powder diffractometer in the range 2-70° 2θ. Inset: high-angle data 30-70° 2θ.

4.11.5.4 CBZ: salicylic acid (CBZ: SAL) co-crystal

The asymmetric unit contains one CBZ molecule and one SAL molecule. As with all the other co-crystals, the CBZ amide group forms a $R_2^2(8)$ heterosynthon with the SAL carboxyl group. These heterosynthons are linked by $D_1^1(2)$ interactions between the NH_2 group of CBZ and the carbonyl oxygen of the carboxyl group of SAL. The hydrogen bonding interactions in the CBZ: SAL co-crystal are shown in Figure 4.12

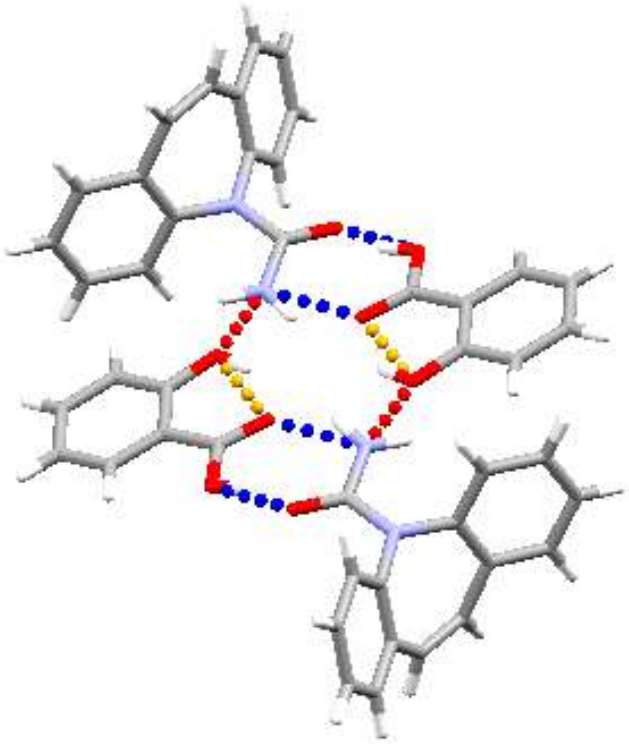

Figure 4.12 Hydrogen bonding in the CBZ: SAL co-crystal. The blue dashed lines show $R_2^2(8)$ heterosynthon interactions. The red dashed lines show the intermolecular $D_1^1(2)$ interactions and the orange dashed lines show intramolecular $D_1^1(2)$ interactions.

The unit cell of the CBZ: SAL co-crystal contains 4 CBZ molecules and 4 SAL molecules. The packing in the unit cell results in the formation of translation stack motifs. A packing diagram of the CBZ: SAL co-crystal is shown in Figure 4.13

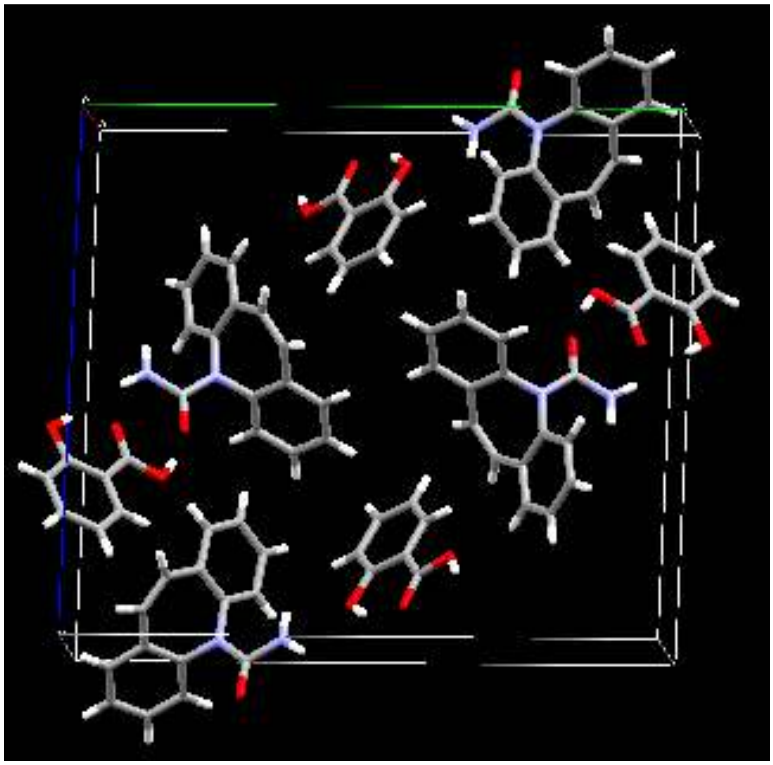

Figure 4.13 Packing diagram for CBZ: SAL co-crystal showing the formation of a translation stack between the CBZ molecules in the unit cell. The view is along the a axis.

An excellent fit to the data was obtained after rigid-body Rietveld refinement. The Rietveld plot is shown in Figure 4.14. The R_{wp} for this structure is 3.667

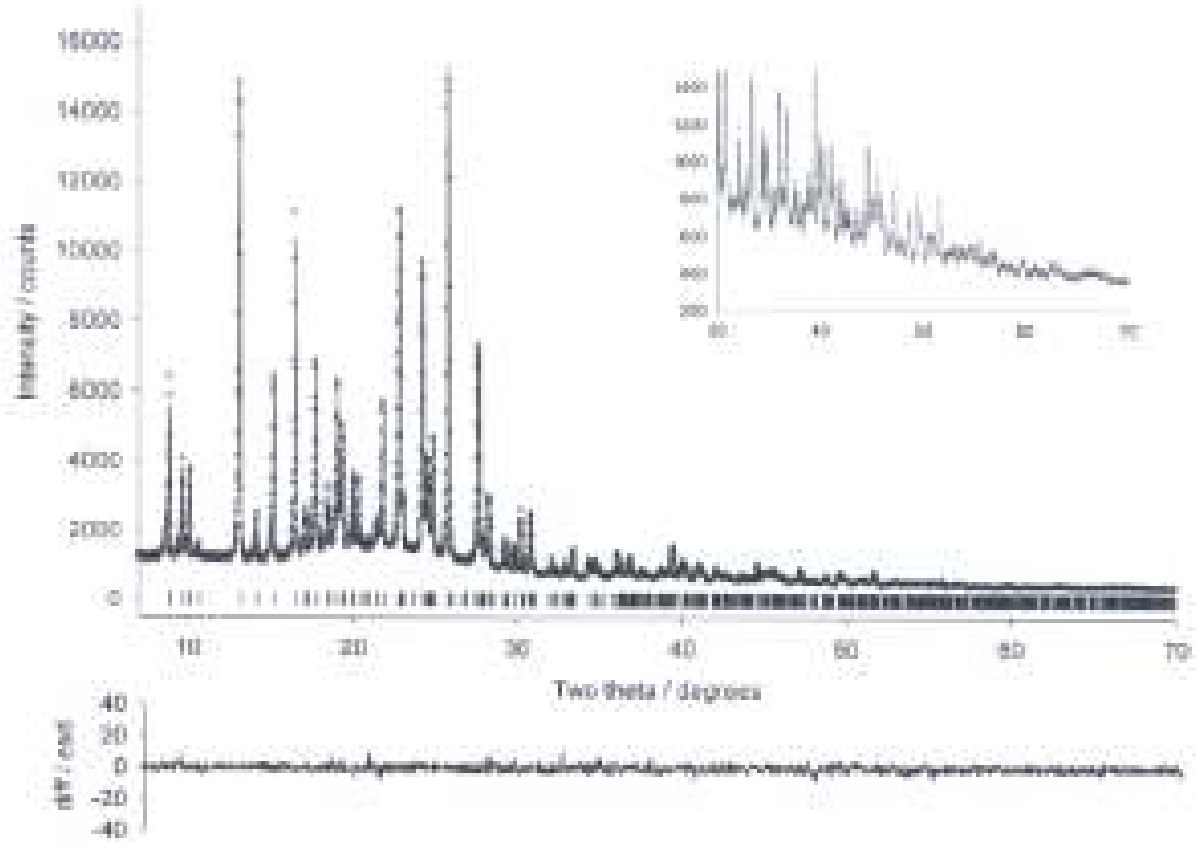

Figure 4.14 Observed profile (circles), calculated profile (line) and difference (y_{obs}-y_{calc})/$\sigma(y_{calc})$ plot for the rigid body Rietveld refinement of the CBZ: SAL co-crystal structure solved from data collected on a laboratory powder diffraction data in the range 2-70° 2θ. Inset: high-angle data 30-70° 2θ.

Based on the information obtained from the 4 CBZ co-crystals studied, it appears that the co-crystal former has an impact on the motifs formed between the CBZ molecules in the co-crystals. More specifically, it appears that planar, aromatic co-crystal formers seem to favour the formation of translation stack motifs, and this observation is in good agreement with published data (Childs *et al.,* 2009).

4.12 Comparison of single crystal structures and powder structures

The refined unit cell parameters for the single crystal structures are shown in Table 4.5 and the refined unit cell parameters for the structures from powder diffraction data are shown in Table 4.6.

Table 4.5 Refined unit cell parameters for the single crystal structures (data collected at 150K, Childs *et al.,* 2009)

Co-crystal	a (Å)	b (Å)	c (Å)	α°	β°	γ°
CBZ:HNA	16.641(13)	5.033(5)	24.493(2)	90	99.062(6)	90
CBZ:CAM	12.589(6)	13.145(6)	14.482(7)	90	105.742(2)	90
CBZ:BEN	28.516(18)	5.161(4)	24.736(15)	90	103.448(4)	90
CBZ:SAL	5.106(4)	19.783(2)	18.328(2)	90	97.903(7)	90

Table 4.6 Refined unit cell parameters for the co-crystal powder structures (data collected at 298K)

Co-Crystal	a (Å)	b (Å)	c (Å)	α°	β°	γ°
CBZ:HNA	16.689 (16)	5.127 (46)	24.574 (22)	90	99.274 (79)	90
CBZ:CAM	12.589 (94)	13.149 (68)	14.483 (95)	90	105.724 (59)	90
CBZ:BEN	28.730 (51)	5.222 (96)	24.801 (46)	90	103.411 (15)	90
CBZ:SAL	5.187 (87)	19.843 (32)	18.344 (33)	90	97.902 (13)	90

The agreement between the unit cell parameters in the above tables is excellent. The very small differences which are observed are due to the slight contraction of the crystal lattice at the low temperatures used in the single crystal experiments. The accuracy of the crystal structures solved from powder diffraction data is also clear if the hydrogen bonding interactions are taken into account. Table 4.7 shows the hydrogen bond distances in the co-crystal structures solved from powder diffraction data. Table 4.8 shows the equivalent hydrogen bond distances in the co-crystal single crystal structures.

Table 4.7 Hydrogen bond distances for CBZ co-crystals solved from powder diffraction data

CBZ co-crystal	CBZ:HNA	CBZ:CAM	CBZ:BEN	CBZ:SAL
[a]D N-H_{amide}...$O_{carboxyl}$	2.121 Å	2.123 Å	2.120 Å	2.203 Å
[a]D O-$H_{carboxyl}$...O_{amide}	1.667 Å	2.022 Å	1.679 Å	1.677 Å
[b]D N-H_{amide}...O	n/a	2.855 Å	n/a	2.715 Å

[a] These interactions make up the $R_2^2(8)$ heterosynthon which is observed in all of the CBZ co-crystals. [b] These interactions make up the $D_1^1(2)$ interactions which are observed in the CBZ: CAM and CBZ: SAL co-crystals only. In the case of the CBZ: CAM co-crystal, the oxygen atom involved in this interaction is a carbonyl oxygen atom in a carboxyl group of (+)-camphoric acid. In the case of the CBZ: SAL co-crystal, the oxygen atom involved in this interaction is the hydroxyl oxygen atom in salicylic acid.

Table 4.8 Hydrogen bond distances for CBZ co-crystal single crystal structures

CBZ co-crystal	CBZ:HNA	CBZ:CAM	CBZ:BEN	CBZ:SAL
[a]D N-H_{amide}...$O_{carboxyl}$	1.994 Å	2.074 Å	2.004 Å	2.063 Å
[a]D O-$H_{carboxyl}$...O_{amide}	1.796 Å	1.715 Å	1.785 Å	1.723 Å
[b]D N-H_{amide}...O	n/a	2.364 Å	n/a	2.510 Å

As can be seen from Tables 4.6 and 4.7, the hydrogen bond lengths between the amide group of CBZ and the carboxyl group of the carboxylic acids are very similar, which indicates that the hydrogen bond strength is the same in each of the co-crystals. This is unsurprising, as identical hydrogen bonded interactions should be of identical strength. It is also clear from Tables 4.6 and 4.7 that there are very slight differences in the hydrogen bond lengths in the single crystal structures compared to the structures solved from powder diffraction data. For example, if we consider the CBZ: HNA co-crystal, the N-$H_{amide...}O_{carboxyl}$ hydrogen bond length is 0.127Å longer in the crystal structure solved from powder diffraction data than in the single crystal structure. However, the O-$H_{carboxyl}$...O_{amide} hydrogen bond length is 0.129Å shorter in the crystal structure solved from powder diffraction data than in the single crystal structure. This phenomenon is due to the anisotropic nature of the lattice contraction on cooling the single crystals.

In addition to the excellent agreement between the unit cell parameters and hydrogen bond lengths, further confidence in the accuracy of the co-crystal structures solved from powder diffraction data was gained by overlaying the powder structures with the corresponding single crystal structures. The agreement between the structures was excellent for each of the co-crystals, as shown by very small RMSD (root mean squared deviation) between the structures. Table 4.9 shows the RMSD values for the CBZ co-crystals.

Table 4.9 RMSD values between single crystal and powder structures of the CBZ co-crystals

Co-crystal	RMSD (Å)	PXRD similarity	molecules in common
CBZ:HNA	0.094	0.995	15 out of 15
CBZ:CAM	0.147	0.999	8 out of 15
CBZ:BEN	0.648	0.941	5 out of 15
CBZ:SAL	0.097	0.995	15 out of 15

As can be seen from the above table, the co-crystals crystal structures solved from powder diffraction data match the single crystal structures well. Figure 4.15 shows an overlay of the powder structure of CBZ: HNA vs. the single crystal structure.

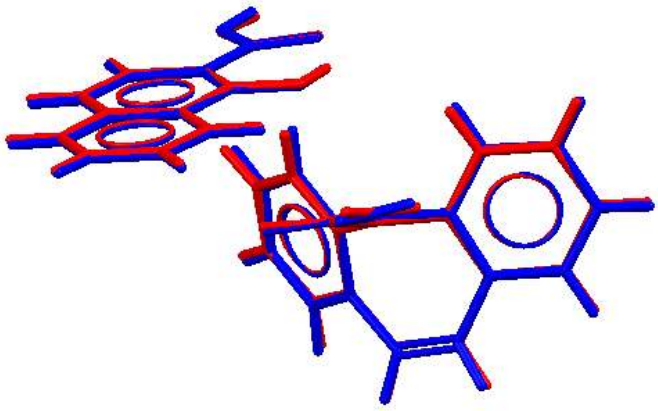

Figure 4.15 Overlay of the single crystal (blue) and refined powder (red) structures of CBZ:HNA co-crystal showing the excellent agreement between the two structures (RMSD = 0.094Å)

The exception to this is the CBZ: BEN co-crystal. In all cases, the powder patterns calculated from the single crystal structures and the observed powder patterns for the same material are extremely similar. The reason for the poor agreement between the CBZ: BEN co-crystal structures could be due to several factors, such as; an inadequate input model for simulated annealing or inadequate data (poorly estimated reflection intensities). Both of these factors would complicate SDPD attempts. Another possibility is that the sample of CBZ: BEN prepared for these studies was mixed phase. However, the melting point (112.7°C) of the sample of CBZ: BEN co-crystal prepared for these studies was very close to the reported melting point of 112.5°C for CBZ: BEN co-crystal (Childs *et al.,* 2008) which suggests that the sample of CBZ: BEN prepared for structure solution attempts was pure. Furthermore, the DSC trace of the CBZ: BEN co-crystal prepared during this work showed no thermal events other than melting of the co-crystal. The DSC trace for CBZ: BEN co-crystal is shown in Appendix 3. Therefore, it seems unlikely that impurities (different polymorphs or unreacted starting materials) are responsible for the poor agreement between the CBZ: BEN co-crystal structures. Nevertheless, the crystal structure was indeed solved, as confirmed by the chemically plausible hydrogen bond interactions and successful Rietveld refinement of the structural model.

The DFT calculations confirmed that the structures solved from powder diffraction data were low energy, and that no lower energy conformations lie close to the co-crystal structures. This helped to confirm the correctness of the crystal structures. The positions of the hydrogen atoms involved in the supramolecular synthons were also more accurately described in the CASTEP optimised structures.

4.13 Summary

The CBZ co-crystals were a good test case for structure solution on beamline I11, as they represent moderately complex systems typical of pharmaceutical samples. The crystal structure of CBZ: CAM co-crystal, which is more complex (30 DOF, Z'=2) was solved successfully from data collected on beamline I11. The crystal structures of CBZ co-crystals could also be solved from laboratory powder diffraction data, but the unit cell parameters were much less precisely determined from laboratory data. Radiation damage was observed in some co-crystal samples, but this is unsurprising, as organic materials with light atoms are susceptible to radiation damage when exposed to synchrotron radiation and in all but one case, did not preclude successful structure determination. Nevertheless, beamline I11 allowed the rapid and accurate solution of the crystal structures of two novel CBZ co-crystals well before single crystal structures of the materials were reported, and the beamline shows great potential for the analysis of pharmaceutically relevant materials.

Chapter 5

Crystal structures of organic salbutamol salts from laboratory X-ray powder diffraction data

5.1 Introduction

Salt formation in the pharmaceutical industry gives the opportunity to modify the characteristics of the drug substance, thus allowing the development of a dosage form with good bioavailability, stability, manufacturability and patient compliance. Salts are most commonly prepared to increase the solubility of the drug (Banerjee *et al.*, 2005, Serajuddin, 2007); however the salt form also has an influence on other physicochemical properties, such as melting point (Bucci *et al.*, 1998), hydroscopicity (Zupancic *et al.*, 2010, Elder *et al.*, 2010) , chemical stability (Towler *et al.*, 2008, Telang *et al.*, 2009), dissolution rate, solution pH (Reddy *et al.*, 2009) and mechanical properties (David *et al.*, 2010) .

Poorly soluble drug salts can also be advantageous; examples of poorly soluble salts used to prolong drug action include olanzapine pamoate (Lindenmayer, 2010) and diltiazem pectate (Shah & Chafetz, 1994). Some drugs have an extremely bitter taste, which can lead to poor patient compliance. Formulating drugs with an unpleasant taste as poorly soluble salts reduces the solubility of the drug in saliva, thus alleviating the unpleasant taste. This approach has been used to form poorly soluble salts of clarithromycin, chlorpheniramine and aspirin (Gowthamarajan *et al.*, 2004). Some drugs, particularly the opioid analgesics can be prone to abuse by recreational users. Formulation of poorly soluble salts is a potential way of reducing the addiction and abuse potential of such drugs. For example, the abuse potential of propoxyphene was reduced by formulating the drug as a poorly soluble napsylate salt rather than the much more soluble hydrochloride salt (Fudala & Johnson, 2006). The structure of propoxyphene napsylate is shown in Figure 5.1

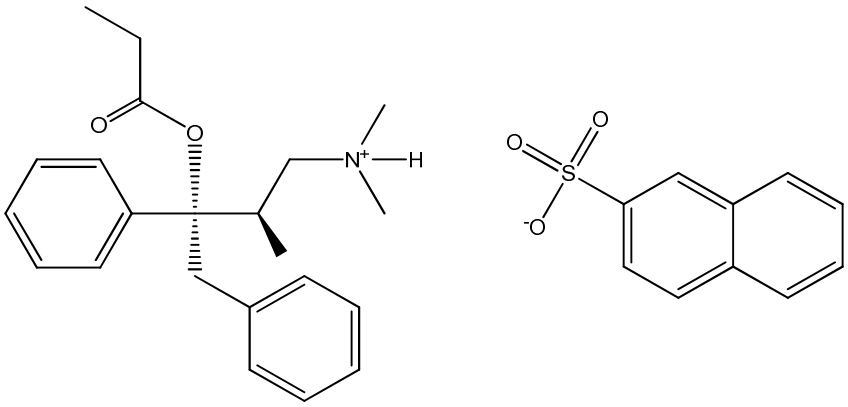

Figure 5.1 Molecular **s**tructure of propoxyphene napsylate

There is a wide range of pharmaceutically acceptable acids available for forming salts of a drug (P. & Wermuth, 2002), but the use of some of these acids is exceptionally rare. For example, only one drug, salmeterol, has ever been marketed as a xinafoate (1-hydroxy-2-naphthoate) salt. Salmeterol was formulated as the xinafoate salt to reduce the dissolution rate and solubility of the drug. The structure of salmeterol xinafoate is shown in Figure 5.2. Table 5.1 lists the frequency of occurrence of common pharmaceutical salts.

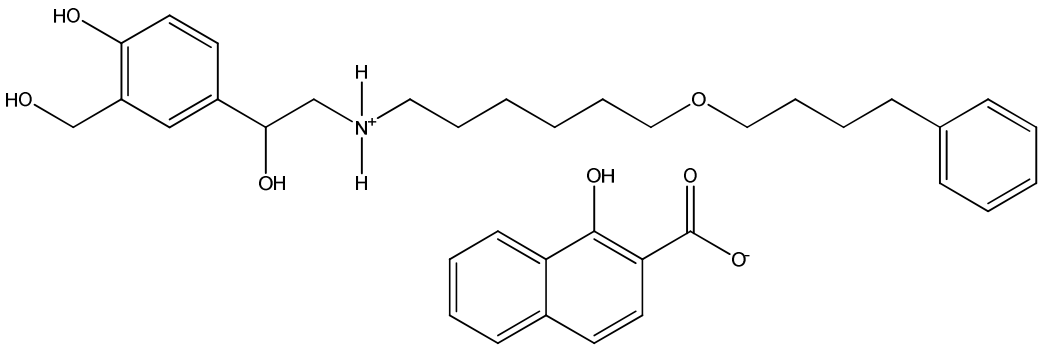

Figure 5.2 Molecular structure of salmeterol xinafoate

Although the use of some acids or bases is rare, provided that the counterion is non-toxic, or it can at least be proven that the benefits of the drug outweigh any risks associated with the use of a given acid or base used to form a salt, then the compound may be approved for use in a pharmaceutical product.. For example, the compound diethylamine is corrosive, but the diethylammonium salt of diclofenac has been approved as a pharmaceutical product (Voltarol®) which is used as a topical gel.

Table 5.1 The frequency of occurrence of counterions in the 10 most common pharmaceutical salts

salt	% prevalence	example
hydrochloride	43.99	methadone hydrochloride
sulphate	5.82	spectinomycin sulphate
bromide	3.79	ipratropium bromide
chloride	3.53	doxacurium chloride
mesylate	3.2	imatinib mesylate
maleate	3.14	chlorpheniramine maleate
citrate	2.81	sildenafil citrate
tartrate	2.68	alimenazine tartrate
phosphate	2.48	clindamycin phosphate
acetate	2.09	calcium acetate

The short acting β2 adrenoceptor agonist salbutamol (Figure 5.3) is indicated for the treatment of asthma and COPD by relieving the bronchospasm associated with these conditions. Salbutamol base is a Biopharmaceutical Classification System (BCS) class 2 drug (Eixarch *et al.*, 2010) which means that the drug exhibits low solubility and high permeability (Amidon *et al.*, 1995). Salbutamol base is administered *via* a nebuliser. The solubility of salbutamol is increased by formulation of the hemisulphate salt, which is available in forms suitable for administration as inhaled, oral solid and liquid and i.v injection forms. Salbutamol hemisulphate is a BCS class 3 drug (Kasim *et al.*, 2004) exhibiting high solubility

and low permeability. Table 5.2 shows the solubility and log P data for salbutamol base and salbutamol hemisulphate. The structure of salbutamol hemisulphate is shown in Figure 5.4

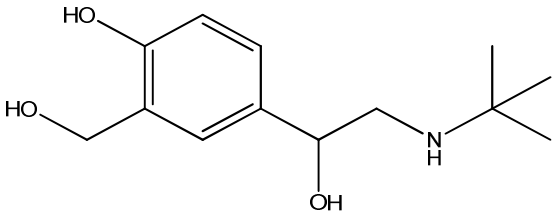

Figure 5.3 Molecular structure of salbutamol base

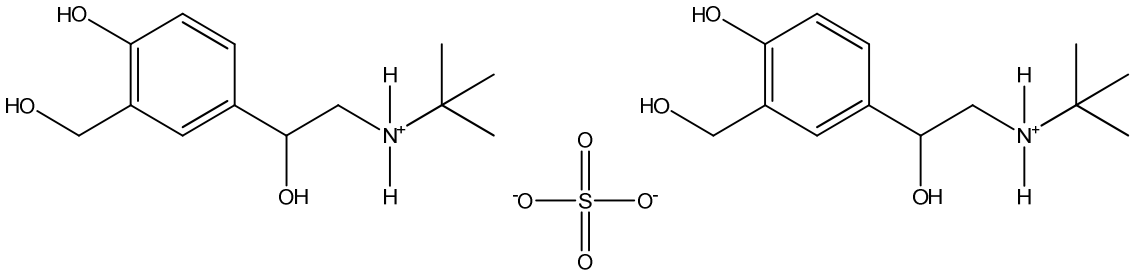

Figure 5.4 Structure of salbutamol hemisulphate

Table 5.2 Solubility and log P data for salbutamol base and salbutamol hemisulphate

Salbutamol form	log P	solubility (mg/ml)
freebase	1.4	3
hemisulphate	0.97	33

After inhalation of salbutamol, the bronchodilation effect exhibits a peak after 1-2 hours and can last for 4-5 hours. However, following oral administration, the bronchodilation effect exhibits a peak after 2-3 hours, which can last for 4-6 hours (Imboden & Imanidis, 1999).

However, there are currently no formulations of salbutamol which can provide immediate relief of an asthmatic episode. There is interest in formulation of salbutamol for sublingual administration for rapid relief (Caira *et al.*, 2002). In order to cross the sublingual mucosa, salbutamol would need to be formulated in such a way that the aqueous solubility is decreased, and the lipophilic character increased. One way of increasing the lipophilic character of salbutamol is to form salts with lipophilic counterions. Several organic salts of salbutamol have been reported in the literature, specifically with the intention of preparing poorly soluble salts to increase the lipophilicity of the drug (Penkler *et al.*, 1999, Brown *et al.*, 1993, Brown *et al.*, 1994) or to select the most appropriate salt to use in a dry powder inhaler (DPI) device (Harris *et al.*).

Traditionally, salt screening is solution based, with the acid and base allowed to react in solution to form a salt complex that precipitates. An attractive alternative to solution based salt screening is screening via mechanochemistry (grinding) methodology. Mechanochemical salt preparation has several advantages over the more traditional solution based approach. Firstly, there is no need to use large amounts of organic solvents for crystallisation, thus mechanochemistry is a 'green' approach to salt formation. That said, the addition of small amounts of solvent can enhance the kinetics of salt formation and depending on the class of solvent used (i.e. polar or non polar) different polymorphic forms of a material can be obtained (Trask *et al.*, 2004).

Secondly, salt formation using mechanochemical methods is quantitative, with complete conversion of reactants to products (Trask *et al.*, 2006). Thirdly, the novel salt can be obtained much faster by mechanochemical methods, as there is no need to wait for solvent

evaporation. Finally, it is possible to obtain novel materials by mechanochemical means that cannot be prepared from solution (Telang *et al.*, 2009, Fernandez-Bertran *et al.*, 1998).

When carrying out a salt screen, the pK_a of the drug and the pK_a of pharmaceutically acceptable acids and base are compared, and if the difference in pK_a values (ΔpK_a) is greater than 3 units, then salt formation is likely to occur. However, if the ΔpK_a between the drug and the potential salt former is less than 3 units, then co-crystal formation may take place rather than salt formation. This is the so-called "rule of 3", and is often used in the selection of counterions in salt screens. Although a useful indicator of the likelihood of salt formation, ΔpK_a values are not a guarantee that salt formation will occur, for various reasons. Firstly, pK_a values are determined in aqueous solution. Carrying out a salt formation in organic solvents will have an effect on the pK_a value of the drug and salt former respectively, so it may well be the case that a predicted salt may not form due to different dissociation behaviour of the reactants in non-aqueous solvents. Secondly, if salt formation is attempted by neat grinding, it is unlikely that dissociation takes place, as no solvent is present. Proton transfer in this case is by mechanical activation and associated lowering of the activation energy for salt formation.

Salbutamol was screened against pharmaceutically acceptable acids in an attempt to form novel salts. The screening experiments were carried out using both the traditional solution-based method and mechanochemical methods. The acids used in the screen were chosen based on previous literature reports of novel salbutamol salts, but the crystal structures of the salts were unknown (Harris *et al.*). The crystal structures of six of these salts were solved from laboratory powder diffraction data. It was possible to grow a single crystal of one of the salts, salbutamol xinafoate, which allowed a comparison of the powder structure and the

single crystal structure to be made; therefore giving an insight into the accuracy of the structures solved from powder diffraction data.

5.2 Preparation and characterisation of salbutamol salts

5.2.1 Solution based salt screening

100mg (0.42mmol) of salbutamol was dissolved in either acetonitrile or methanol and treated with 0.42mmol of each of the following acids; acetic acid, formic acid, butyric acid, nicotinic acid, saccharin and 1-hydroxy-2-naphthoic acid (Figure 5.5). The resulting twelve solutions (six acetonitrile and six methanol) were set aside for slow evaporation. The pK_a values of salbutamol and the acids are shown in Table 5.3.

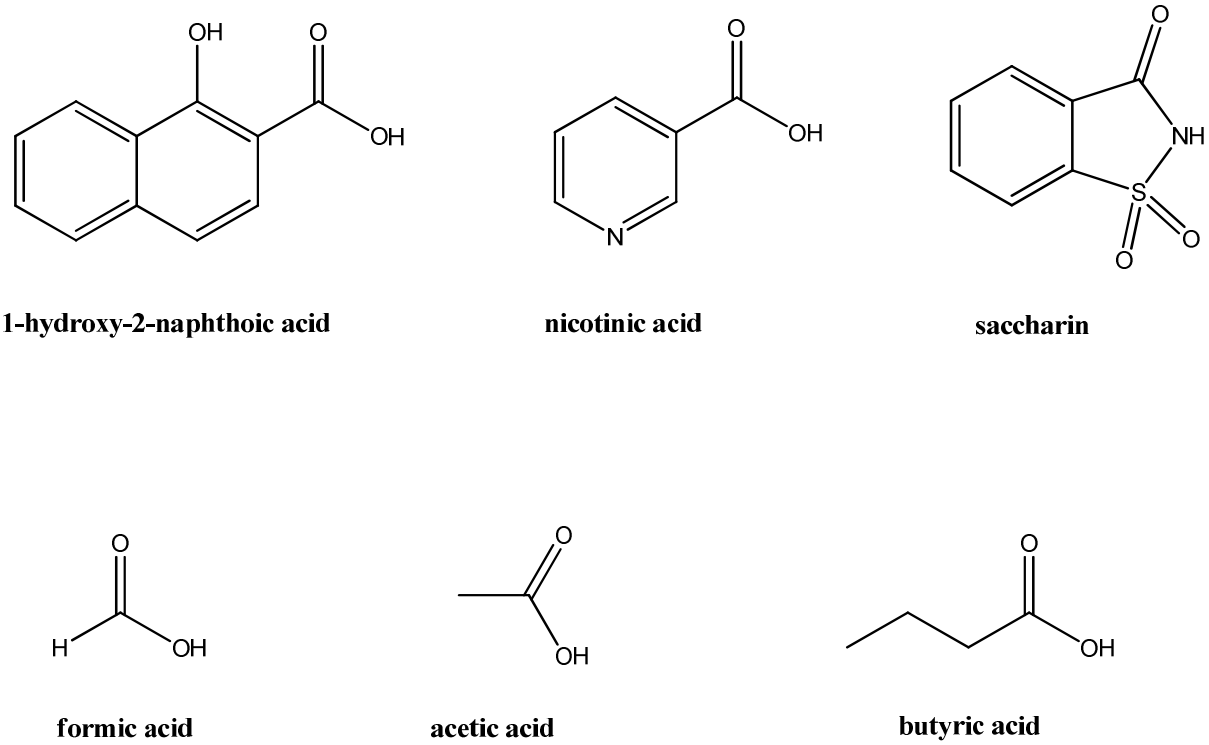

Figure 5.5 Molecular structures of the acids used to form salbutamol salts

Table 5.3 pK_a values of salbutamol and the pharmaceutically acceptable acids

compound	pK_a	ΔpK_a
salbutamol	10.30	0
acetic acid	4.79	5.51
butyric acid	4.82	5.48
formic acid	3.77	6.53
1-hydroxy-2-naphthoic acid	3.02	7.28
nicotinic acid	2.20	8.10
saccharin	2.32	7.98

5.2.2 Mechanochemistry based salt screening

100mg (0.42mmol) of salbutamol and 0.42mmol of each of the acids were ground together in an agate pestle and mortar for 15 minutes. In those cases where the acids were liquids at room temperature, the acid acted both as a solvent and a reactant. In those cases where the acids were solids at room temperature, 20µl of ethanol was added before grinding to facilitate the reaction.

5.2.3 Indexing of the salts

The first 21 peaks in the powder diffraction patterns were fitted in DICVOL06. Two of the salts were triclinic, which required long calculation times when indexed using DICVOL06, so to speed up the indexing process, TOPAS 4 SVD-Index method was used to find the unit cell parameters for the salts.

5.2.4 Thermal analysis of the salts

Approximately 5mg of each of the finely ground salts were placed in 25µl aluminium pans. The sample pans were then sealed with a pierced aluminium lid. Samples were then heated from 20°C to 250°C at a rate of 10K min^{-1} under a nitrogen purge.

5.2.5 XRPD data collection

Samples were lightly ground and filled into 0.7mm borosilicate glass capillaries. Data were then collected as described in §3.2.2

5.2.6 Model building and Z-matrix preparation

The salbutamol cation was generated by manual protonation of the crystal structure of salbutamol base (CSD ref code BHHPHE (Beale & Grainger, 1972)). The new structure was then renumbered and the hydrogen atom bond lengths were normalised to X-ray values. The models of the counterions (acetate, formate, butyrate, nicotinate, saccharinate and xinafoate) were generated from the crystal structures of salts found in the CSD. If the carboxylate input models had been generated by a geometry optimisation method, the C-O bond lengths would have been equal in the carboxylate anion input models, due to the fact that a carboxylate ion is resonance stabilised. However, in the solid state, the C-O bond lengths can be different, as is the case with sodium acetate trihydrate. Thus, the carboxylate ion input models were used without optimisation to make the C-O bond lengths equal. Table 5.4 shows the CSD reference codes for the counterions. The cations were deleted and the anions were renumbered and normalised in the same way as for the salbutamol cation.

Table 5.4 Sources of the acid anion input models for the salbutamol salts

counterion	salt structure	CSD refcode
acetate	trimethoprim acetate	FUWVAU
formate	calcium formate	CAFORM05
butyrate	dicyclohexylammonium butyrate	JEFYAV
nicotinate	pyrimethamine nicotinate	GINNIB
saccharinate	1,4-butanediammonium(bis)saccharinate	GEHWAS
xinafoate	remacemide xinafoate	MAPYOS

5.2.7 Simulated annealing structure solution

Simulated annealing structure solution was carried out in batch mode using GDASH to allow large numbers of jobs to be carried out overnight. MOGUL constraints were applied before the simulated annealing runs were carried out. The simulated annealing protocol is shown in Table 5.5.

Table 5.5 Simulated annealing protocol for the salbutamol salts

N_{runs}	moves per run	cooling rate	χ^2 multiplier
800	$2.5x10^7$	0.01K	1

The best crystal structures from the simulated annealing runs were checked in Mercury to confirm that there were no bad contacts (unusually short or chemically nonsensical contacts) and that the molecular conformation of each structural fragment was acceptable. After these checks had been carried out, the structures were subjected to rigid-body Rietveld refinement.

5.2.8 Rigid body Rietveld refinement

Rigid body descriptors of the structural fragments were derived from the input Z-matrices, but with the values of flexible torsions updated to match the experimental values exactly. These torsion angles were then refined along with the background, scale factor, position, orientation and non-hydrogen isotropic temperature factor (ITF) as described in §3.2.3.5.

5.2.9 DFT calculations

First-principles DFT calculations were performed on the experimental SDPD structures using CASTEP v.4.3 and v.5.0 as described in §3.2.3.5.4.

5.3 Results

5.3.1 Screening results

Only salbutamol xinafoate and salbutamol nicotinate could be prepared easily from solution. In the majority of cases, attempts to crystallise salbutamol salts from solution resulted in the formation of viscous oils, which formed polycrystalline material after 7-14 days. However, mechanochemical screening was much more productive, and polycrystalline salbutamol salts were obtained after 15 minutes of grinding. Salbutamol saccharinate was unique in the fact that this salt was crystallised from the amorphous state. Salbutamol saccharinate was prepared from the amorphous state because the manual grinding used to prepare the other salts failed to produce any reaction between salbutamol and saccharin. The decision was then taken to grind the materials together in a Retsch MM400 mechanical mixer mill at 25Hz for 25 minutes. The resulting material was confirmed as X-ray amorphous based on the absence of Bragg diffraction in the powder diffraction pattern and the characteristic T_g and recrystallisation events observed in the DSC trace of the material. Storing the amorphous material for two days at room temperature and 75% relative humidity (RH) induced crystallisation of the saccharinate salt.

5.3.2 Indexing results

All of the salbutamol salts were sharply diffracting and could be successfully indexed from laboratory XRPD data.

5.3.3 Thermal analysis of the salts

All of the salts showed a sharp melting endotherm, followed by decomposition of the salt. Salbutamol butyrate showed a small endotherm, significantly below the observed melting endotherm. This suggested that the salt may be polymorphic. However, when a sample of salbutamol butyrate was heated to 70°C, which is the temperature of the suspected polymorph transition, new peaks were observed in the powder diffraction pattern, but it was not possible to index the new powder pattern. The melting points of each of the salts are shown in Table 5.6. Figure 5.6 shows the DSC traces of the salbutamol salts.

Table 5.6 Melting point of the salbutamol salts. Salbutamol base melts at 160°C

Salbutamol salt	Melting point °C
acetate	176.69
butyrate	137.39
formate	151.88
nicotinate	269.36
saccharinate	172.01
xinafoate	163.23

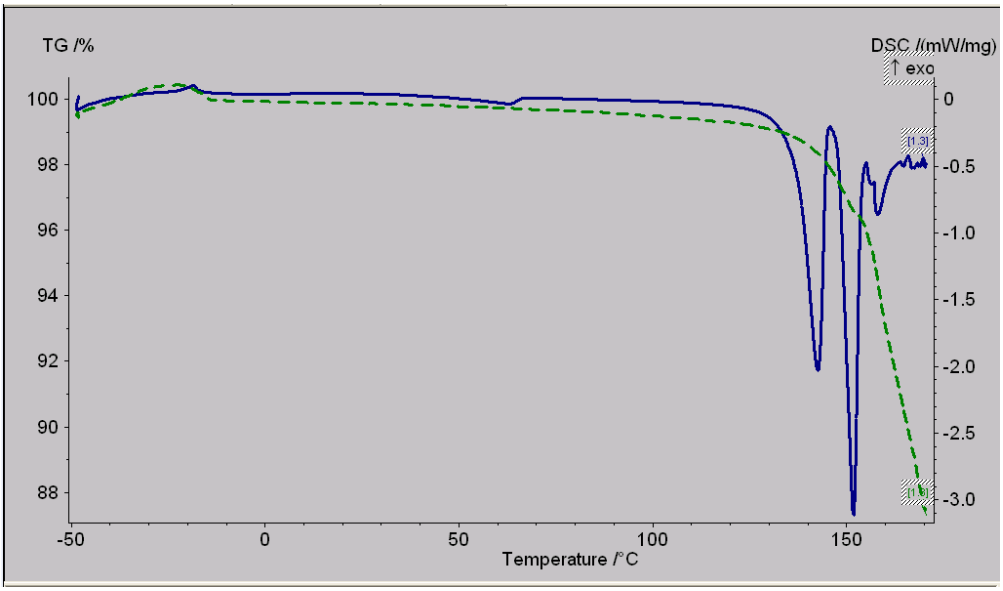

Figure 5.6a DSC trace of salbutamol butyrate in the range -50 - 200°C. The small endotherm at 70°C is evidence of possible polymorphism in this salt.

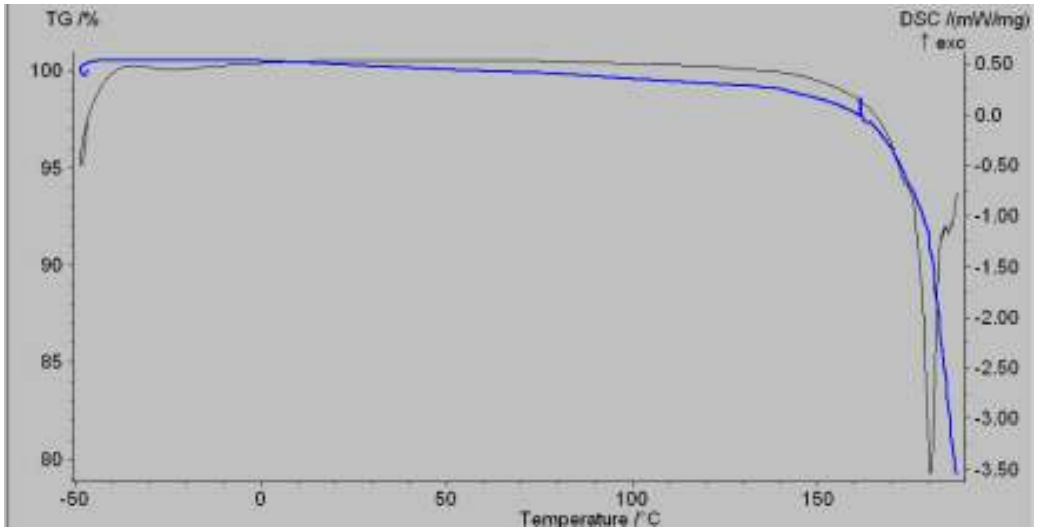

Figure 5.6b DSC trace of salbutamol acetate in the range -50 - 200°C. This salt melts and immediately decomposes.

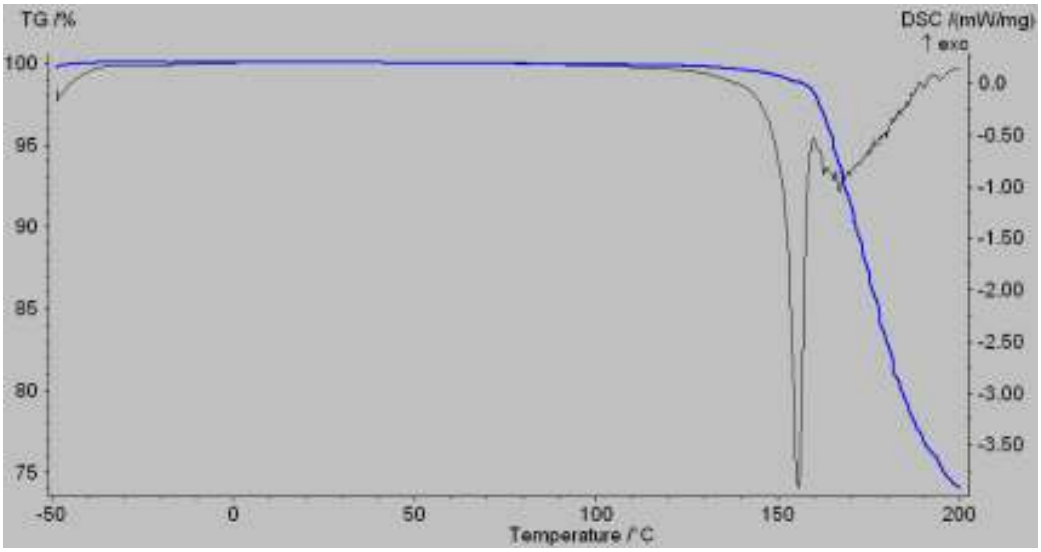

Figure 5.6c DSC trace of salbutamol formate in the range -50 - 150°C. This salt melts and immediately decomposes.

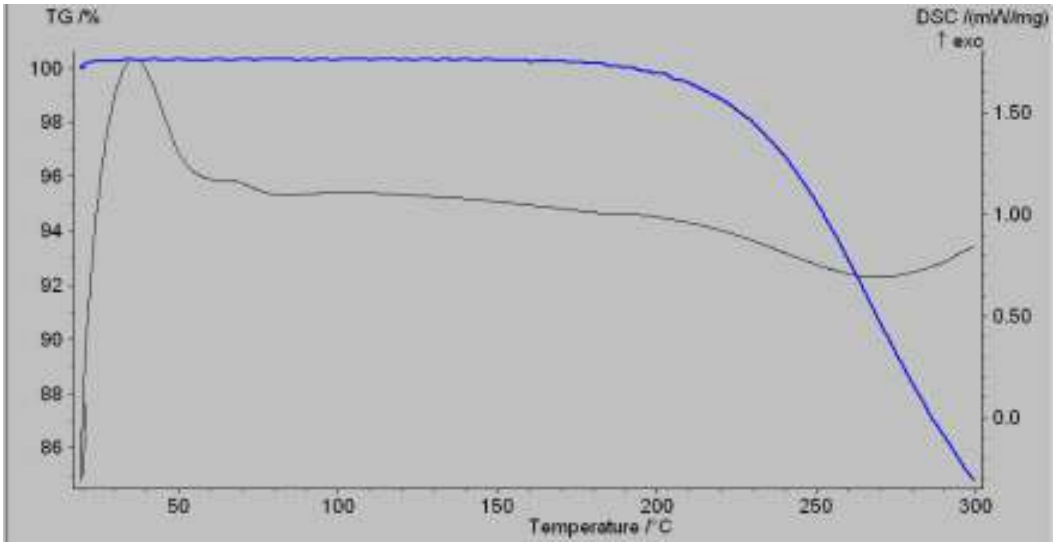

Figure 5.6d DSC trace of salbutamol nicotinate. The melting point of the salt is not easily discernible in the DSC trace, but the sample was molten at 269.39°C. Also, no thermal events were observed in the range -50 - 150°C.

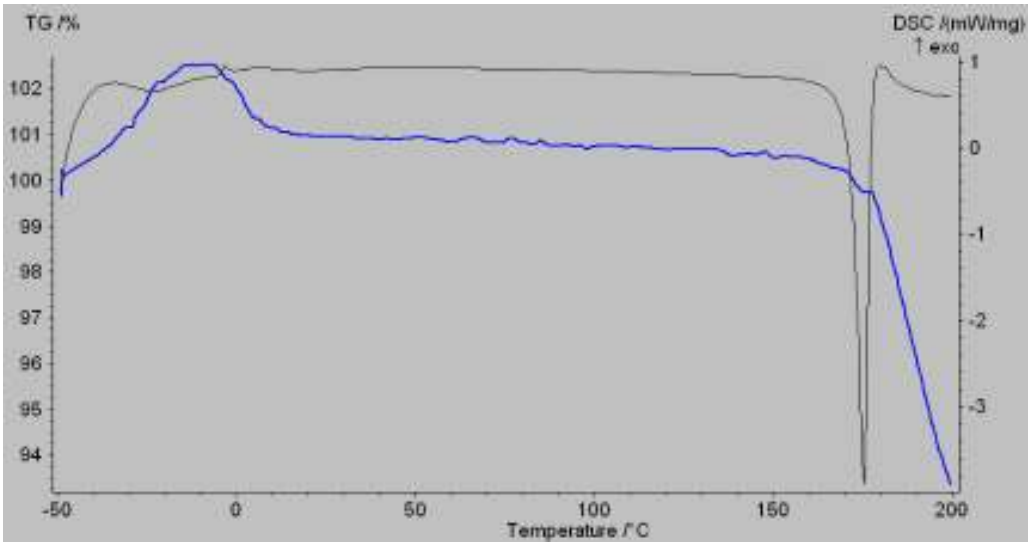

Figure 5.6e DSC trace of salbutamol saccharinate in the range -50 - 200°C. When this salt was prepared, it was X-ray amorphous. The salt recrystallised at -10°C, and melted with immediate decomposition.

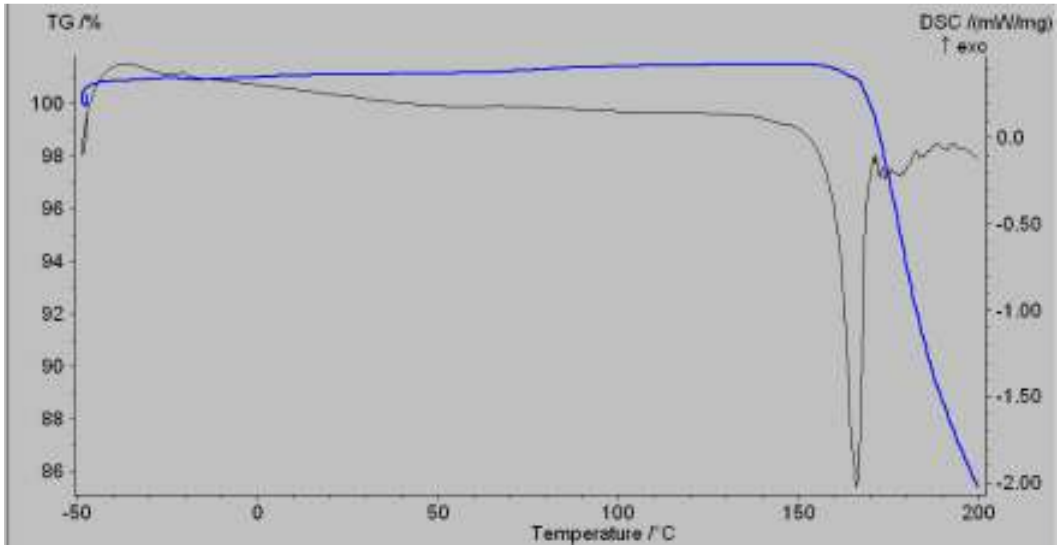

Figure 5.6f DSC trace of salbutamol xinafoate in the range -50 -200°C. The salt melts with immediate decomposition.

Based on the DSC evidence of potential polymorphism of salbutamol butyrate, a sample of this salt was heated to 80°C overnight then powder diffraction data was collected. New peaks were observed in the powder diffraction pattern, but it was not possible to index the data. This indicates that the new material may be a mixture of 2 different polymorphic forms of the

salt or that some degradation may have occurred during the overnight heating. The XRPD data are shown in Figure 5.7.

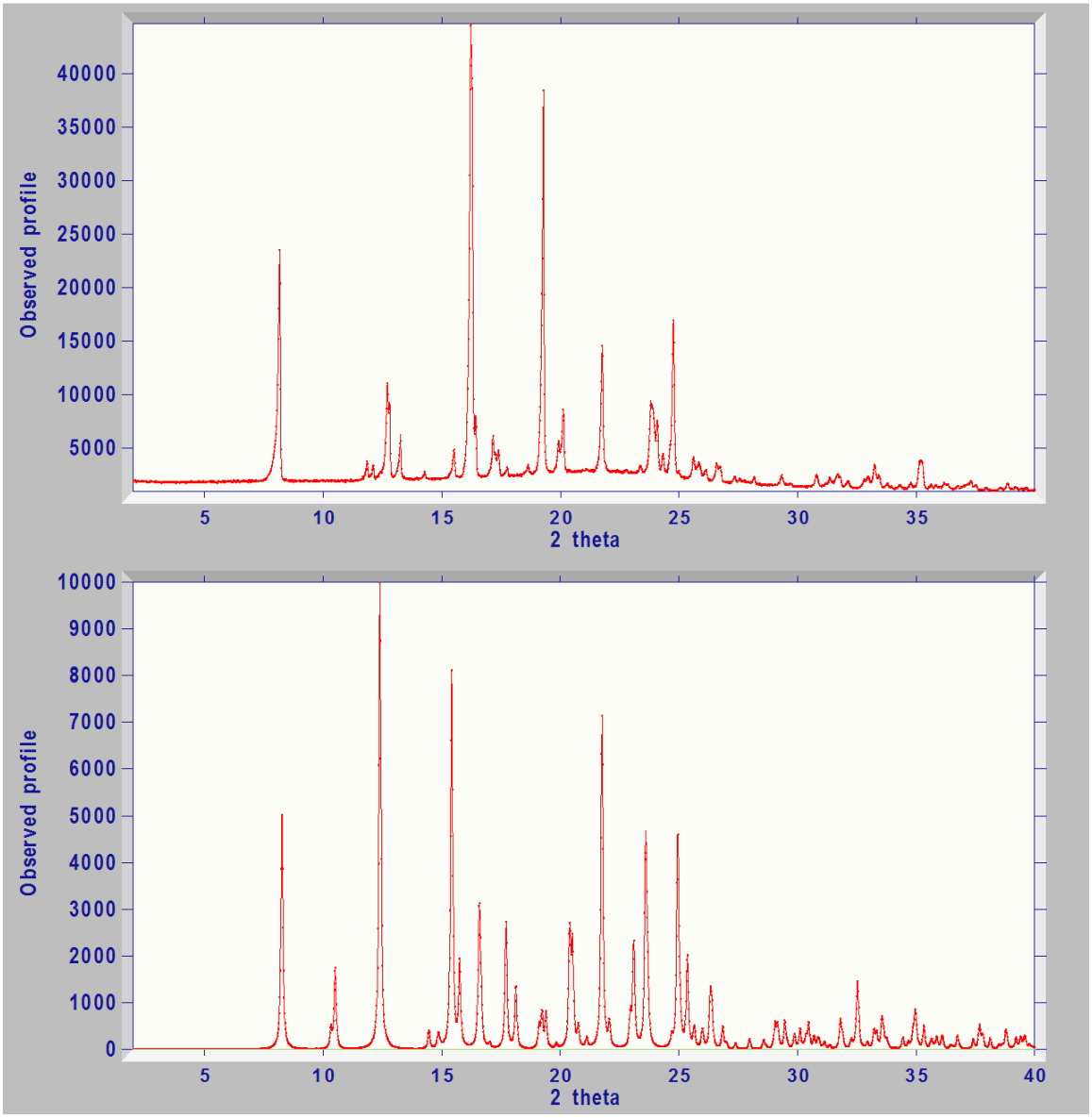

Figure 5.7 Effects of heating a sample of salbutamol butyrate at 80°C overnight. Top: sample after storage at 80°C overnight. Bottom: sample as prepared (by grinding). The evolution of a new XRPD pattern indicates that structural changes are taking place. For example after heating overnight, peaks found at 10.341° 2θ and 10.518° 2θ disappear from the sample prepared by grinding. Similarly, after heating overnight, new peaks are observed at 11.857° 2θ and 12.105° 2θ. However, it was not possible to index the new powder diffraction pattern.

5.3.4 Simulated annealing results

The crystal structures of each of the salbutamol salts were successfully solved from laboratory powder diffraction data. Table 5.7 shows the final refined crystallographic data for each of the salbutamol salts.

Table 5.7 Crystallographic data for the salbutamol salts

salbutamol salt	acetate	butyrate	formate	nicotinate	saccharinate	xinafoate
formula	$C_{15}H_{25}NO_5$	$C_{17}H_{29}NO_5$	$C_{14}H_{23}NO_5$	$C_{19}H_{26}N_2O_5$	$C_{20}H_{26}N_2O_6S$	$C_{24}H_{29}NO_6$
Mwt	299.36	327.42	285.34	362.42	422.50	427.29
crystal system	triclinic	orthorhombic	triclinic	orthorhombic	monoclinic	monoclinic
space group	$P\bar{1}$	*P*bca	$P\bar{1}$	$P2_12_12_1$	$P2_1/c$	$P2_1/c$
a/Å	9.315 (2)	21.365 (5)	9.299 (15)	6.159 (18)	9.44 (10)	12.972 (3)
b/Å	9.892 (2)	14.263 (2)	9.389 (13)	16.715 (4)	25.789 (4)	9.405 (19)
c/Å	9.900 (2)	11.918 (3)	9.851 (16)	18.297 (4)	8.777 (10)	18.924 (5)
α°	99.229 (2)	90.000	98.026 (1)	90.000	90.000	90
β°	111.835 (2)	90.000	104.839 (1)	90.000	94.339 (1)	103.142 (2)
γ°	104.830 (2)	90.000	109.778 (1)	90.000	90.000	90
V/Å^3	787.93 (3)	3635.475 (13)	758.206 (12)	1884.86 (4)	2130.92 (2)	2247.42 (2)
Z	2	8	2	4	4	4
N_{ref}	169	134	284	110	175	126
Pawley $\chi 2$	7.89	5.22	8.58	4.13	5.84	8.03
best DASH ratio	3.86	6.59	1.86	2.11	2.01	1.08
N_{solved}	413	140	297	695	657	566
$\%_{solved}$	51.63	17.5	37.13	86.88	82.13	70.75
total DOF	17	19	17	18	17	18
R_{wp}[a]	4.166	6.551	4.037	4.201	4.677	6.224

[a] The R_{wp} value is the final value obtained from rigid-body Rietveld refinement of the best DASH solution in TOPAS.

5.3.5 Crystal Structures of the salbutamol salts

The fact that each of the samples are indeed salts rather than co-crystals was confirmed by analysis of hydrogen bonded interactions and molecular conformations. Also, ΔpK_a considerations show that salt formation is far more likely than co-crystal formation. In the case of the nicotinate and xinafoate salts, there is a twist of the carboxylate group from the plane of the aromatic ring which is indicative of salt formation in these systems, as confirmed by Mogul searches for other salts containing nicotinate or xinafoate anions. The salts formed from carboxylic acids which are liquids at room temperature all have identical hydrogen bonding interactions between the ions, which leads to very similar packing of the ions to form layered structures. The identical hydrogen bonding interactions in the acetate, butyrate and formate salts suggests that the hydrogen bonds in these salts should be of similar strength. The other salts (nicotinate, saccharinate and xinafoate) have unique hydrogen bonding interactions, with no trends in hydrogen bond lengths observed in these salts. Table 5.8 shows the hydrogen bond geometries of the ammonium groups of the salbutamol salts.

Table 5.8 Hydrogen bond geometries of the ammonium groups of the salbutamol salts

salbutamol salt	acetate	butyrate	formate	nicotinate	saccharinate	xinafoate
D H...A	N1-H11...O4	N1-H11...O5	N1-H11...O5	N1-H11...O5	N1-H11...O6	N1-H11...O5
d(D-H)/Å	0.899	0.898	0.901	0.900	0.900	0.900
d(H...A)/Å	1.954	1.966	1.906	1.768	2.077	1.977
d(D...A)/Å	2.98	2.86	2.756	2.666	2.956	2.832
< DHA/°	139.45	172.85	156.72	175.32	165.16	158.1

The similarity of the acetate, butyrate and formate structures is also clear if the value of the torsion angle of the C-C-N-C chain in the salbutamol ion is taken into consideration. Small, aliphatic carboxylate ions induce very similar conformations of the salbutamol ion, which gives rise to very similar hydrogen bonding interactions and packing in these salts. Table 5.9 shows the conformations of the C-C-N-C chain of the salbutamol ion in each of the salts.

Table 5.9 Conformation of the C-C-N-C chain of the salbutamol ion in each of the salbutamol salts.

salbutamol salt	C-C-N-C torsion angle
acetate	-156.67°
butyrate	-152.06°
formate	-152.06°
nicotinate	174.73°
saccharinate	-163.01°
xinafoate	-176.06°

The crystal structures of each of the salbutamol salts will now be discussed.

5.3.5.1 Crystal structure of salbutamol acetate

The asymmetric unit contains one salbutamol cation and one salbutamol anion. The carboxylate group is planar with respect to terminal methyl group. Hydrogen bonding between the salbutamol and acetate ions forms a robust $R_2^2(9)$ heterosynthon. A $R_2^2(9)$ is also formed between neighbouring salbutamol ions. This pattern is propagated by $D_1^1(2)$ interactions between the salbutamol and acetate ions. The hydrogen bonding interactions in this salt are shown in Figure 5.8.

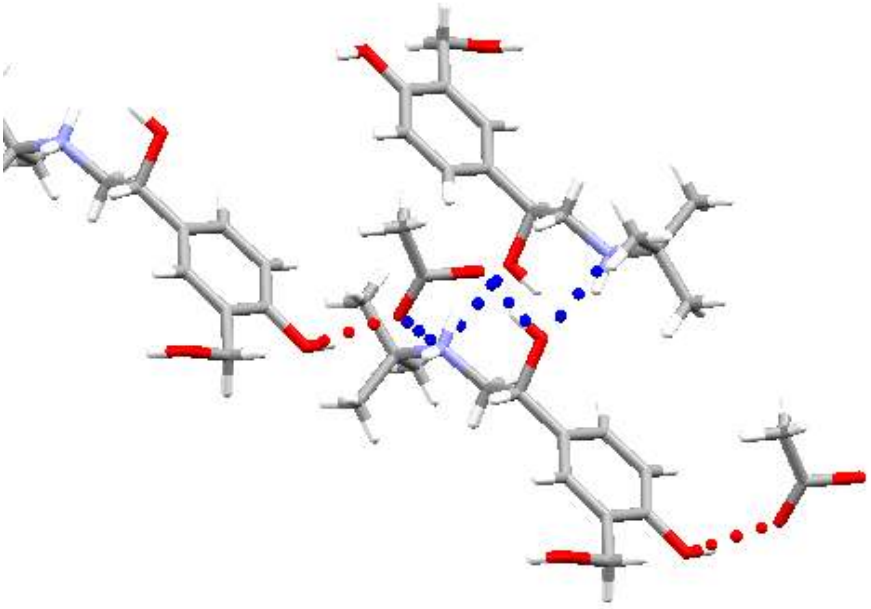

Figure 5.8 Hydrogen bonding interactions in salbutamol acetate showing the $R_2^2(9)$ interactions (blue) and $D_1^1(2)$ interactions (red).

The hydrogen bonding in salbutamol acetate leads to the formation of alternating layers of salbutamol ions and acetate ions as shown in Figure 5.9

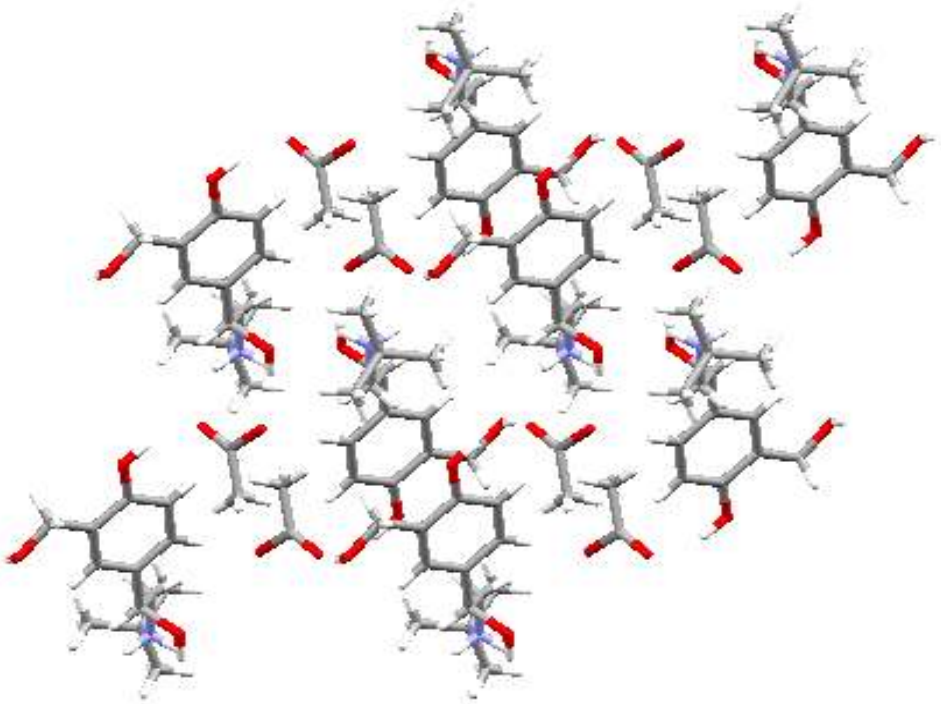

Figure 5.9 Formation of alternating layers of salbutamol ions and acetate ions in salbutamol acetate.

Figure 5.10 shows how the salbutamol and acetate ions pack in the unit cell.

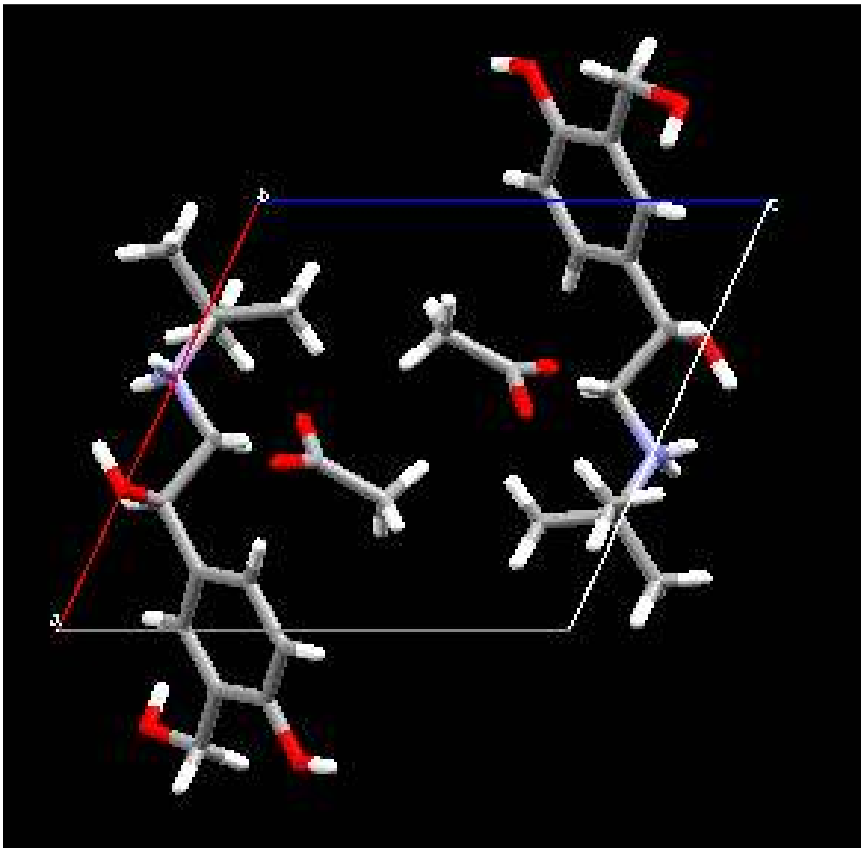

Figure 5.10 Packing diagram for salbutamol acetate.

The Rietveld plot shows that the crystal structure of salbutamol acetate is an excellent fit to the diffraction data. The Rietveld plot for salbutamol acetate is shown in Figure 5.11

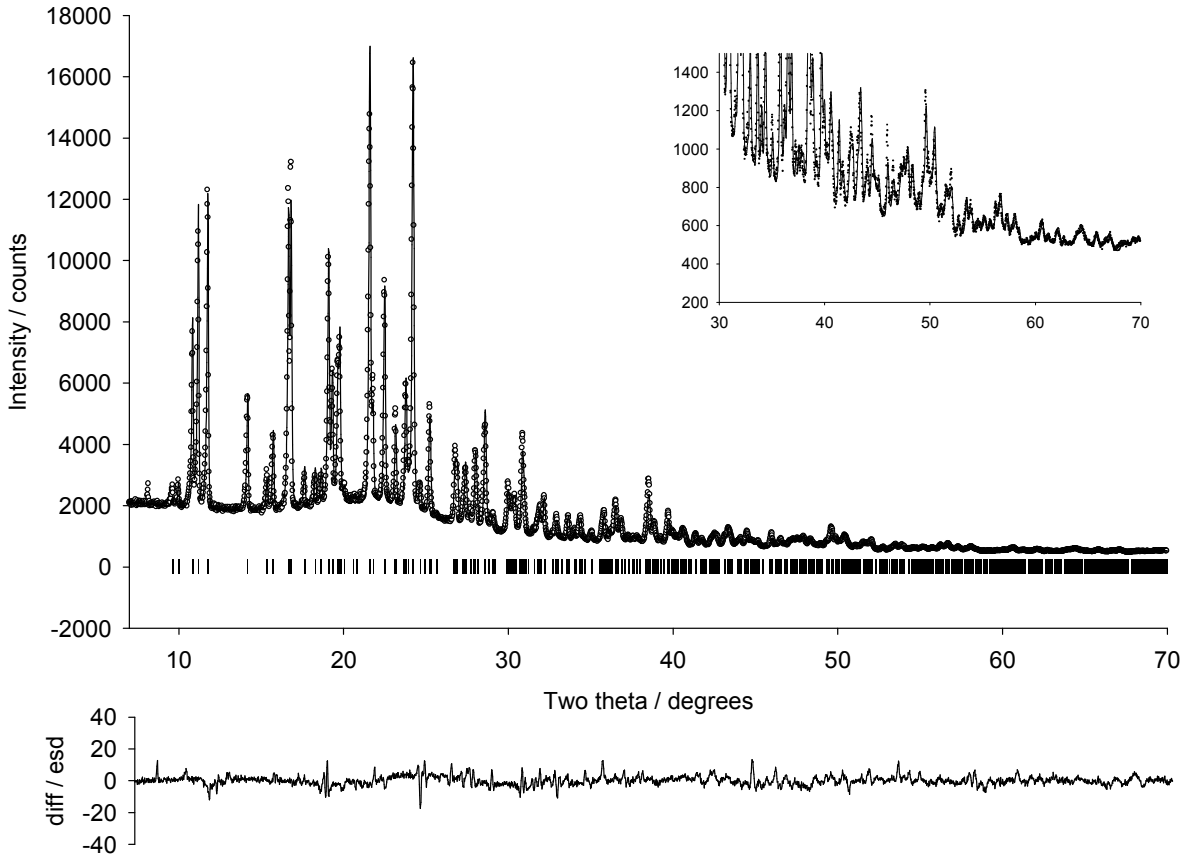

Figure 5.11 Observed profile (circles), calculated profile (line) and difference [(y_{obs} − y_{calc})/σ(y_{calc}) plot for the rigid body Rietveld refinement of salbutamol acetate in the range 2-70° 2θ. Inset: high-angle data 30-70° 2θ.

5.3.5.2 The crystal structure of salbutamol butyrate

The asymmetric unit contains one butyrate anion and one salbutamol cation. The conformation of the carboxylate group relative to the carbon chain is described by the torsion of 70.84° and the angle of 110.45°. The hydrogen bonded interactions and packing are the same as for salbutamol acetate. A packing diagram for salbutamol butyrate is shown in Figure 5.12

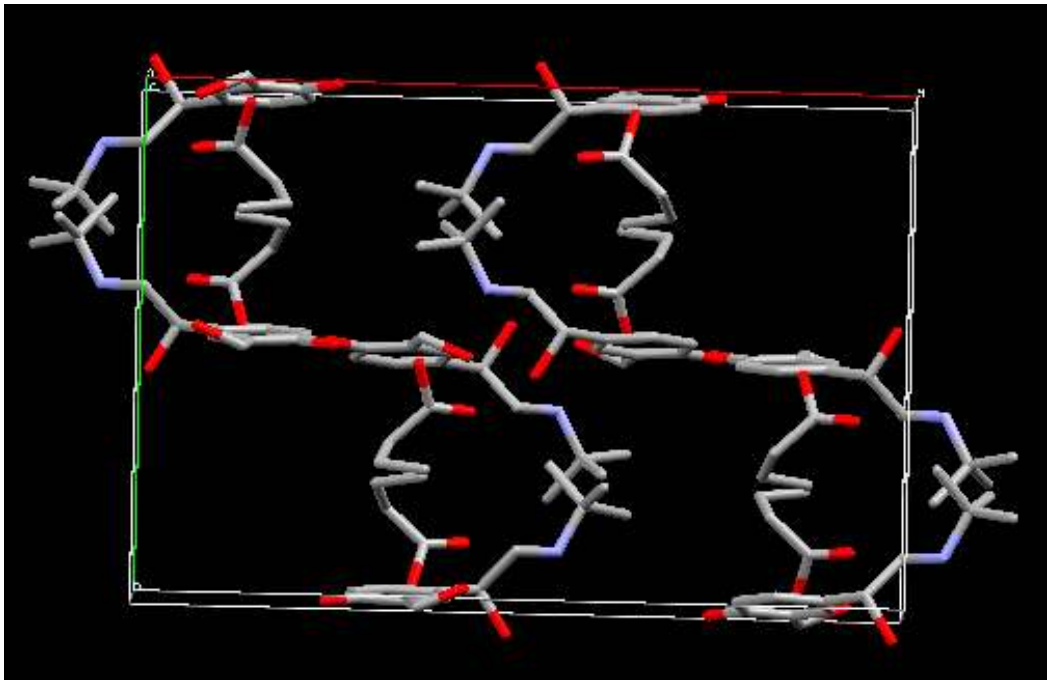

Figure 5.12 Packing diagram for salbutamol butyrate. The view is along the c axis.

From Table 5.6, it is clear that salbutamol butyrate is the most complex of the salbutamol salts (19 DOF). It is also clear that salbutamol butyrate has the highest R_{wp} value of all of the salbutamol salts. Indicating that the experimentally derived crystal structure for this salt does not fit the data as well as the other salbutamol salts. Preferred orientation is one possible cause of a high R_{wp}, but March-Dollase preferred orientation corrections (carried out in 001, 010 and 100 directions) had no significant effect on the final R_{wp} value. Closer inspection of the Rietveld refinement plot showed that there is significant misfit. The difference plot is shown in Figure 5.13.

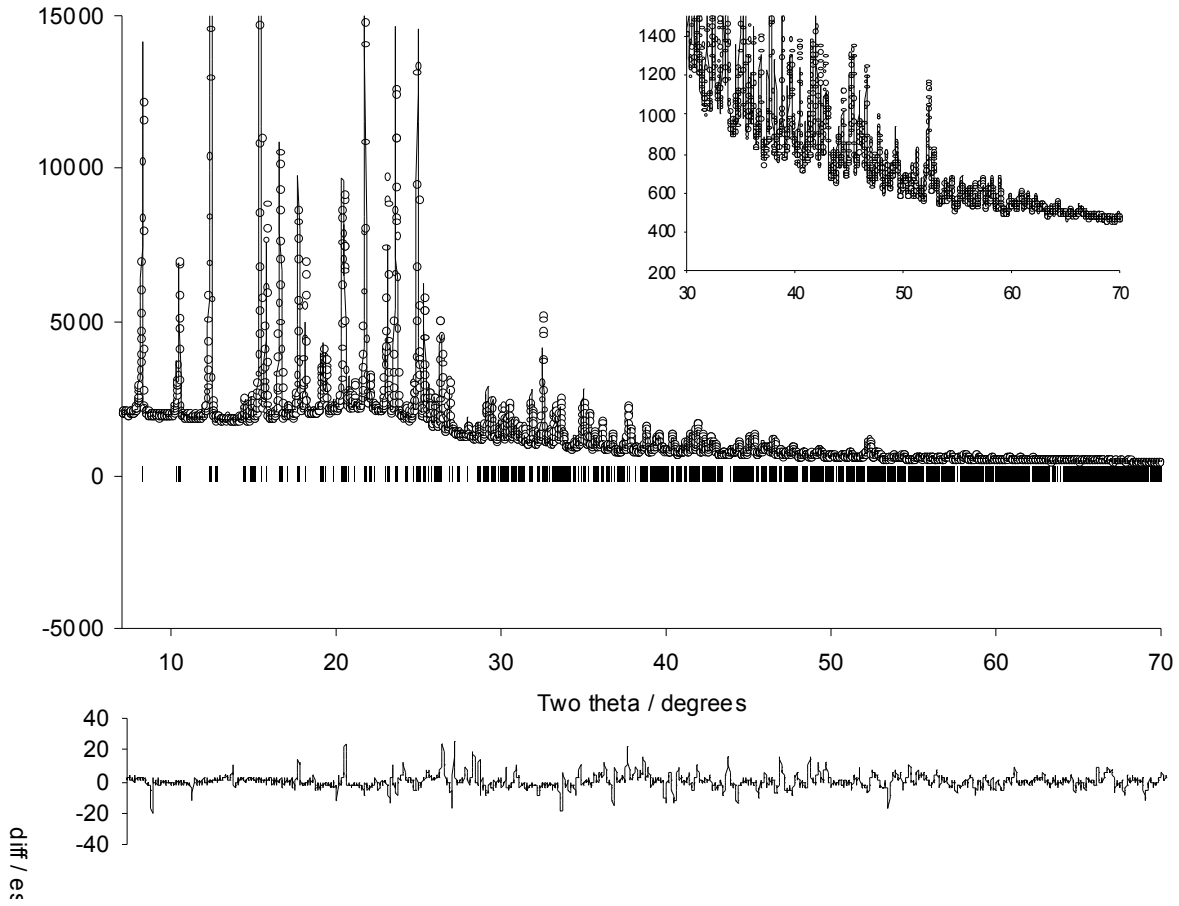

Figure 5.13 Observed profile (circles) calculated profile (line) and difference [$(y_{obs} - y_{calc})/\sigma(y_{obs})$] plot for the rigid body Rietveld refinement of salbutamol butyrate in the range 2-70° 2θ. Inset: high-angle data 30 -70° 2θ. There is clear misfit in the difference plot.

The misfit in the difference plot could also be due to the presence of disorder in the structure. In fact, when simulated annealing runs were carried out using two half-occupancy butyrate ion Z-matrices, although the total DOF was increased significantly from 19 to 27 DOF. That said, structure solution was still feasible under the simulated annealing conditions, and in fact the disordered input model performed much better the fully ordered input model. Table 5.10 shows the results of simulated annealing runs using two half-occupancy butyrate ion Z-matrices.

Table 5.10 Simulated annealing results using two half-occupancy butyrate ion Z-matrices

data range/2θ	N_{ref}	Pawley χ^2	best DASH ratio	N_{solved}	$\%_{solved}$
7.012-37.110	134	5.22	3.21	250	31.25

It is clear from Table 5.10 that the crystal structure of salbutamol butyrate is best described using two half-occupancy butyrate ions rather than a single full-occupancy butyrate ion. However, the disorder in this structure could not be satisfactorily refined, even though it was straightforward to describe all of the structural fragments as rigid bodies. A possible reason for the unsuccessful Rietveld refinement may be that the data available was simply not of sufficient quality to allow satisfactory Rietveld refinement of the structure. This problem may have been circumvented by collecting high-resolution data at a synchrotron radiation source. That said, refinement of the fully ordered crystal structure did result in a reasonable R_{wp} value and a chemically sensible structure which lends confidence that the structure is indeed correct, although it is known that the butyrate ion is actually disordered.

5.3.5.3 The crystal structure of salbutamol formate

The asymmetric unit contains one formate anion and one salbutamol cation. Hydrogen bonded interactions and packing in this salt are the same as those found in salbutamol acetate and salbutamol butyrate. A packing diagram for salbutamol formate is shown in Figure 5.14.

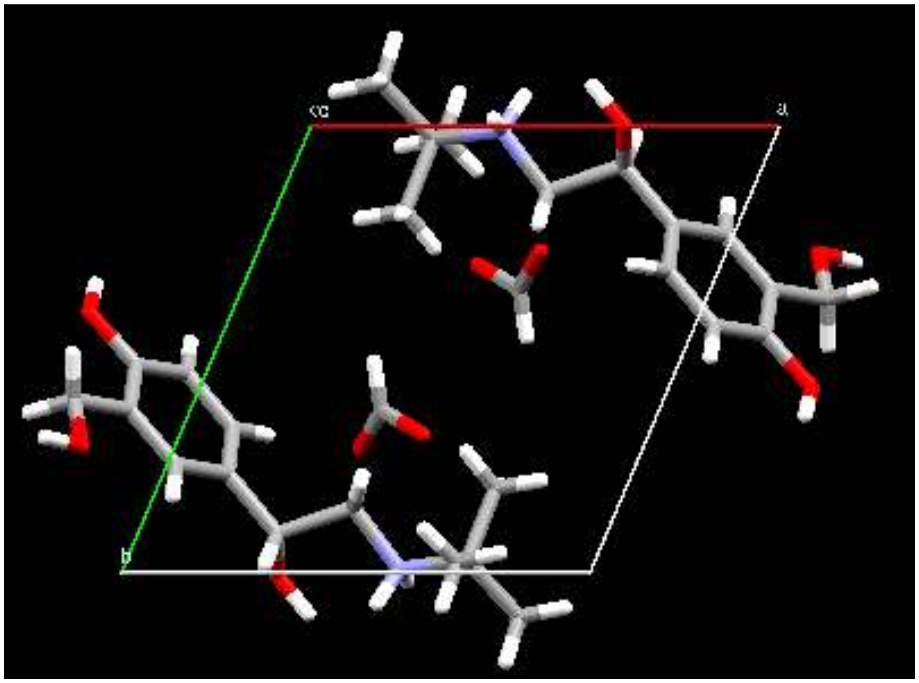

Figure 5.14 packing diagram for salbutamol formate. The view is along the c axis.

The accuracy of the crystal structure of this salt was confirmed by an excellent fit to the data. The final Rietveld plot for this salt is shown in Figure 5.15.

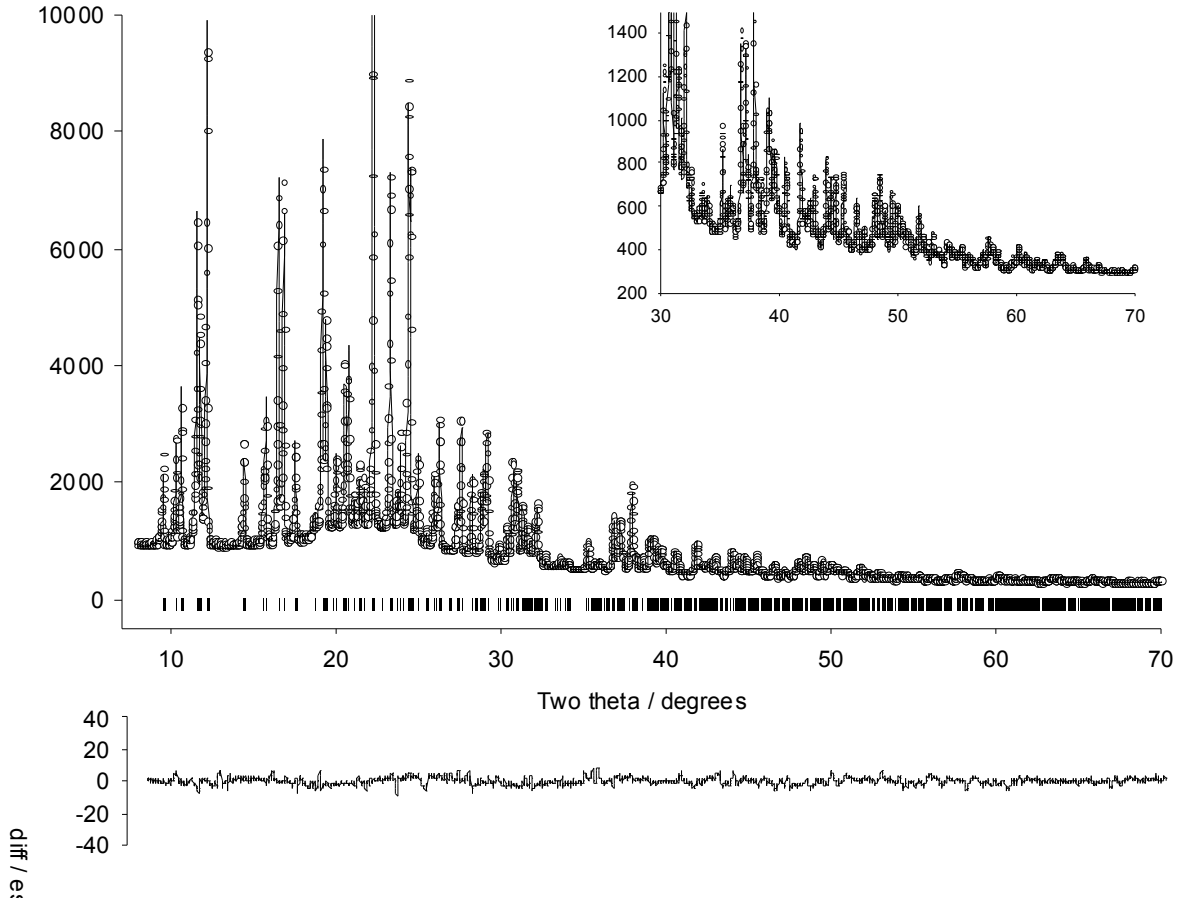

Figure 5.15 Observed profile (circles), calculated profile (line) and difference [(y_{obs} − y_{calc})/σ(y_{calc}) plot for the rigid body Rietveld refinement of salbutamol formate in the range 2-70° 2θ. Inset: high-angle data 30-70° 2θ.

5.3.5.4 The crystal structure of salbutamol nicotinate

The asymmetric unit contains one nicotinate anion and one salbutamol cation. The conformation of the carboxylate group relative to the pyridine ring is described by a torsion angle of 169.00° and the angle of 119.16°. Hydrogen bonding between the salbutamol cation and the nicotinate anion forms $R_2^1(7)$ synthons, which are linked by $D_1^1(2)$ interactions. The hydrogen bonding interactions in this salt are shown in Figure 5.16

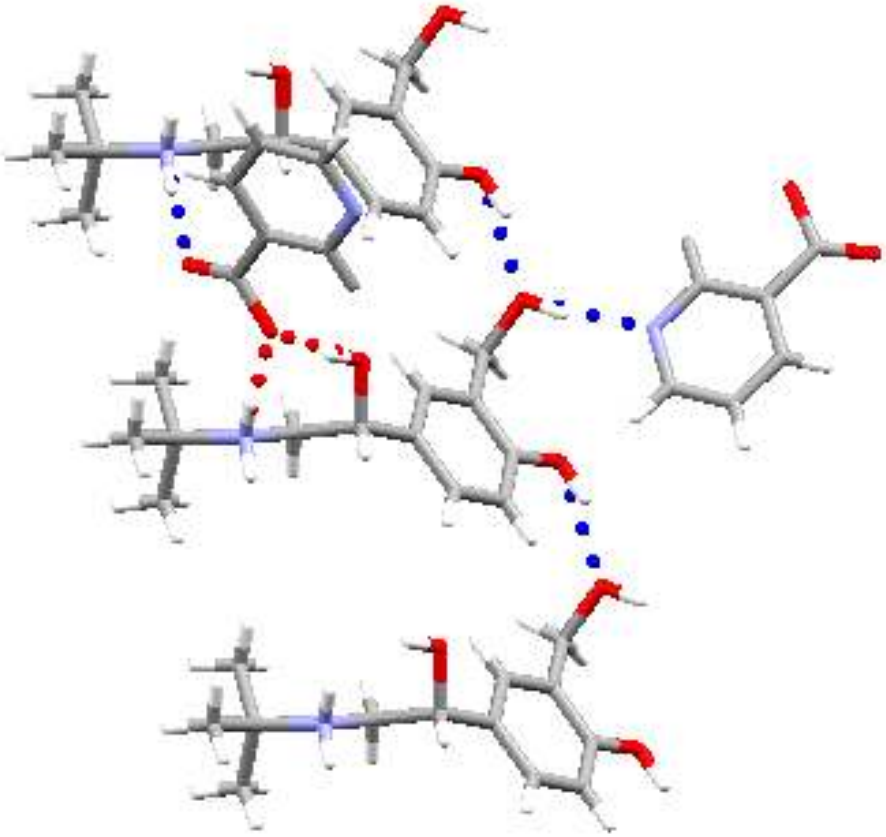

Figure 5.16 Hydrogen bonding interactions in salbutamol nicotinate showing the $R_2^1(7)$ synthon (red) and the $D_1^1(2)$ interactions (blue).

The packing of salbutamol nicotinate results in the formation of alternating layers of nicotinate ions and salbutamol ions. A packing diagram for salbutamol nicotinate is shown in Figure 5.17.

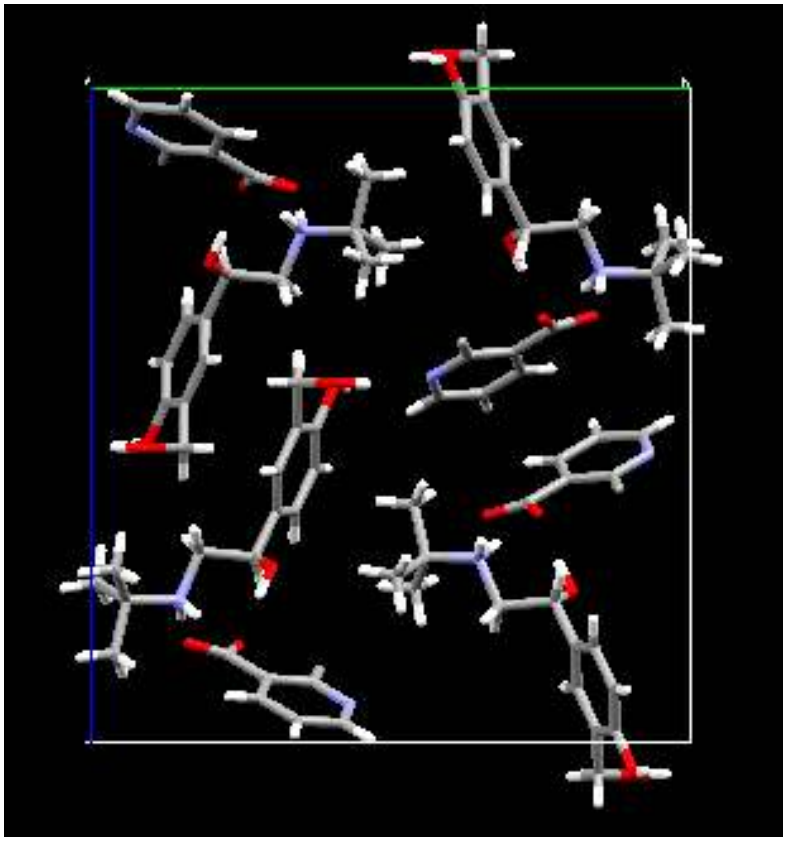

Figure 5.17 Packing diagram for salbutamol nicotinate. The view is along the a axis

The accuracy of the refined crystal structure of salbutamol nicotinate was confirmed by the excellent fit to the data. The final Rietveld plot is shown in Figure 5.18

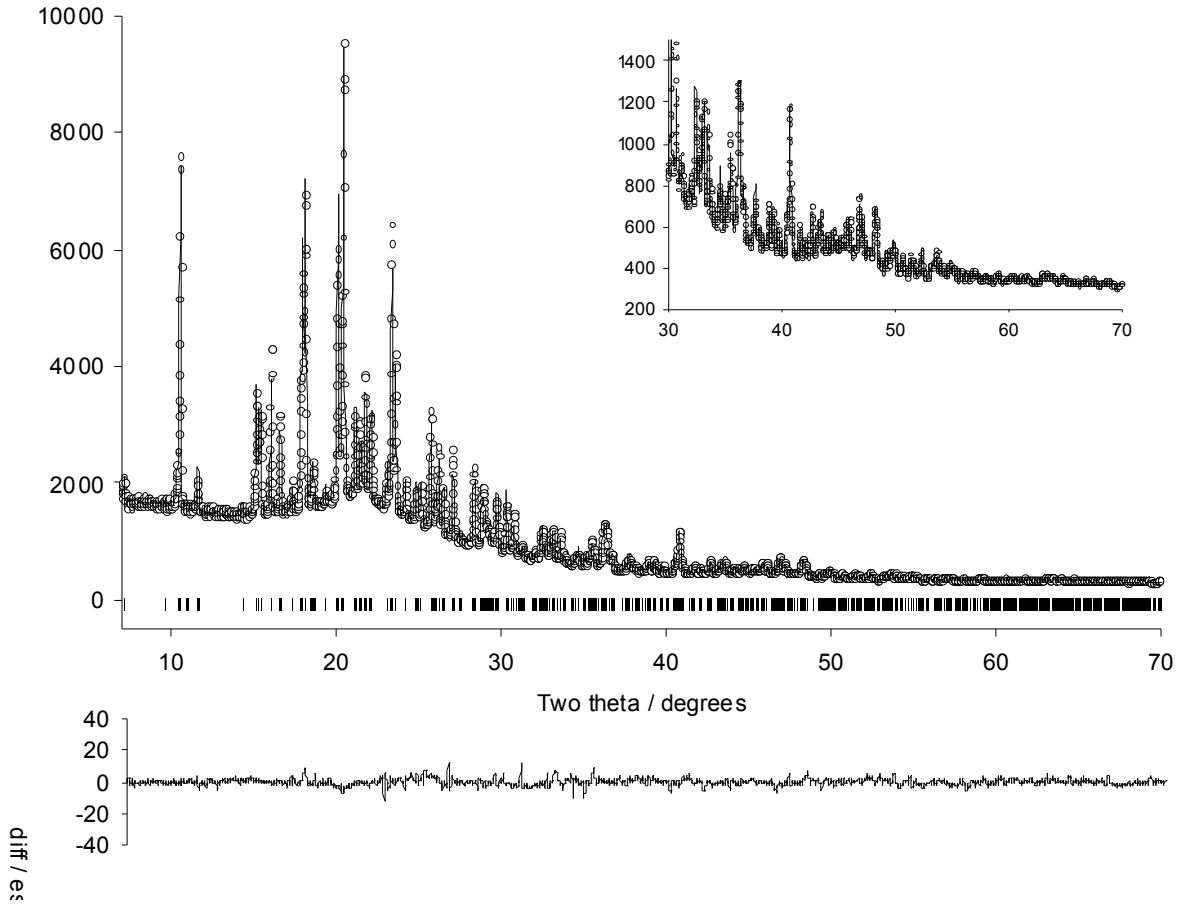

Figure 5.18 Observed profile (circles), calculated profile (line) and difference [(y_{obs} − y_{calc})/σ(y_{calc}) plot for the rigid body Rietveld refinement of salbutamol nicotinate in the range 2-70° 2θ. Inset: high-angle data 30-70° 2θ.

5.3.5.5 The crystal structure of salbutamol saccharinate

The asymmetric unit contains one saccharin anion and one salbutamol cation. The hydrogen bonding interactions are more complex in this salt than in the other salts, and result in the formation of chains of alternating layers of salbutamol and saccharinate ions. As shown in Figure 5.19.

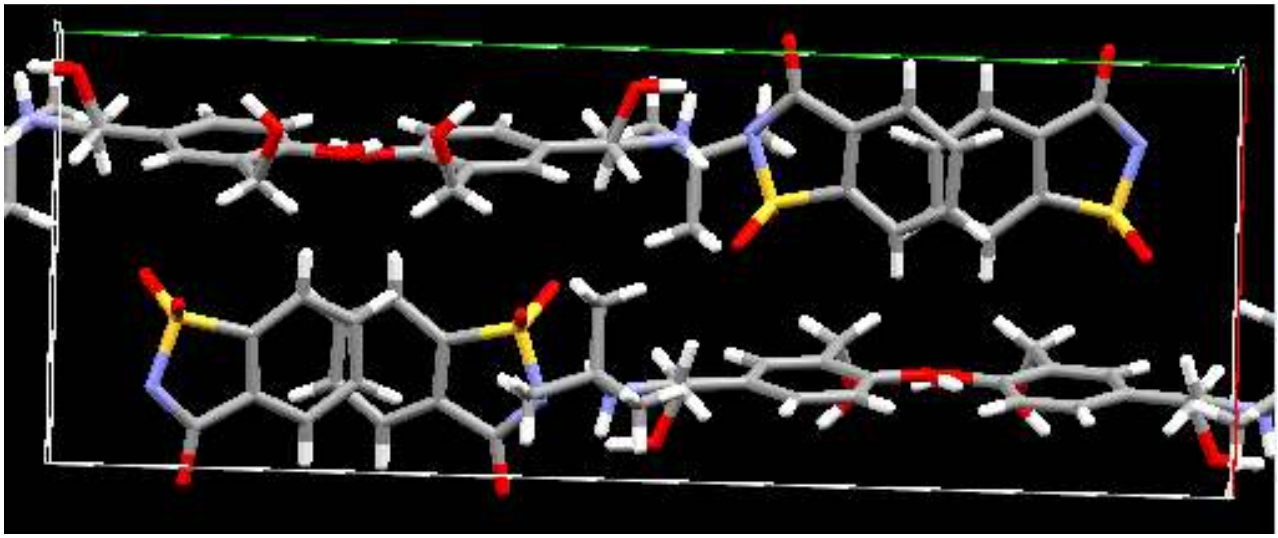

Figure 5.19 Packing diagram for salbutamol saccharinate. The view is along the b axis

The accuracy of the structure was confirmed by an excellent fit to the data. The final Rietveld plot is shown in Figure 5.20.

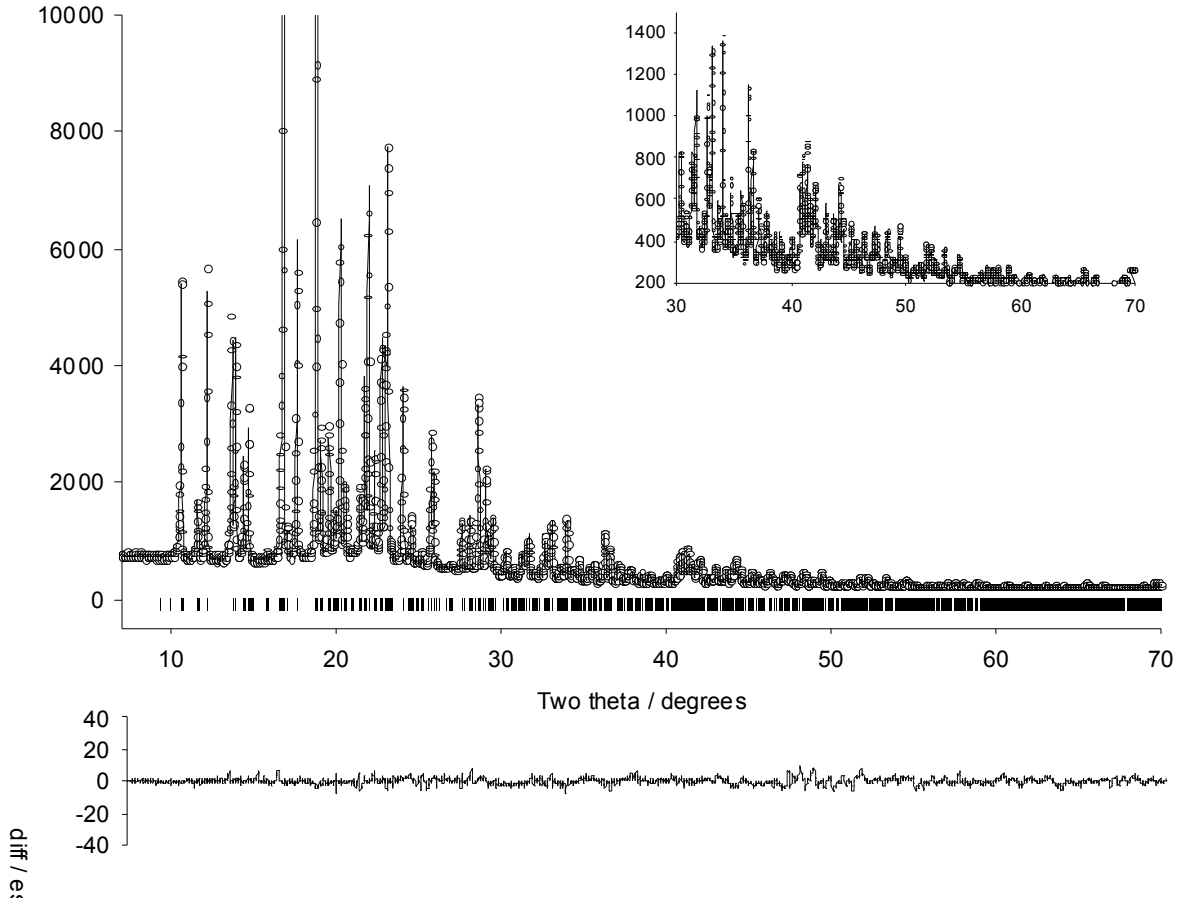

Figure 5.20 Observed profile (circles), calculated profile (line) and difference [$(y_{obs} - y_{calc})/\sigma(y_{calc})$] plot for the rigid body Rietveld refinement of salbutamol saccharinate in the range 2-70° 2θ. Inset: high-angle data 30-70° 2θ.

5.3.5.6 The crystal structure of salbutamol xinafoate

The asymmetric unit contains one xinafoate anion and one salbutamol cation. The conformation of the carboxylate group relative to the naphthalene ring is described by the torsion angle of 176.29° and the angle of 120.38°. The hydrogen bonded interactions in this salt leads to the formation of zigzag chains of salbutamol ions alternating with layers of xinafoate ions as shown in Figure 5.21.

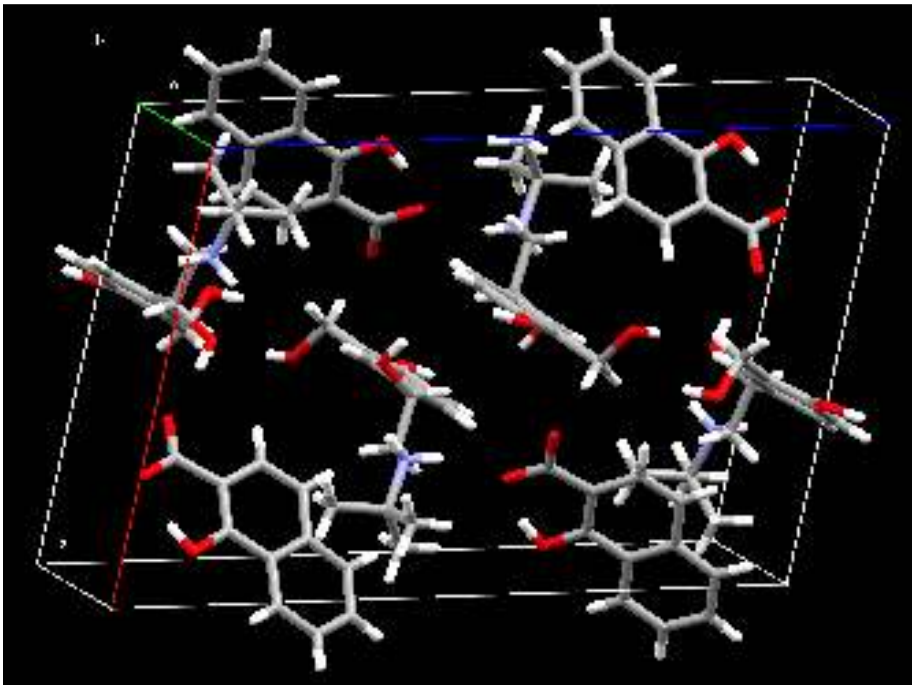

Figure 5.21 Packing diagram for salbutamol xinafoate showing the formation of layers of salbutamol cations and xinafoate anions.

As with salbutamol butyrate, the R_{wp} value returned from Rietveld refinement of salbutamol xinafoate is relatively high, and again inclusion of March-Dollase PO corrections in the final Rietveld refinement did not have a significant effect on the R_{wp} value, and the difference plot shows similar misfit to that observed in the difference plot for salbutamol butyrate, suggesting potential disorder in this salt, however, in this instance, using half-occupancy anion input models did not improve the success rate of structure solution. A single crystal of this salt was obtained, and disorder was suspected in the naphthalene ring system, but this disorder could not be successfully refined in the single crystal structure. The Rietveld plot for salbutamol xinafoate is shown in Figure 5.22.

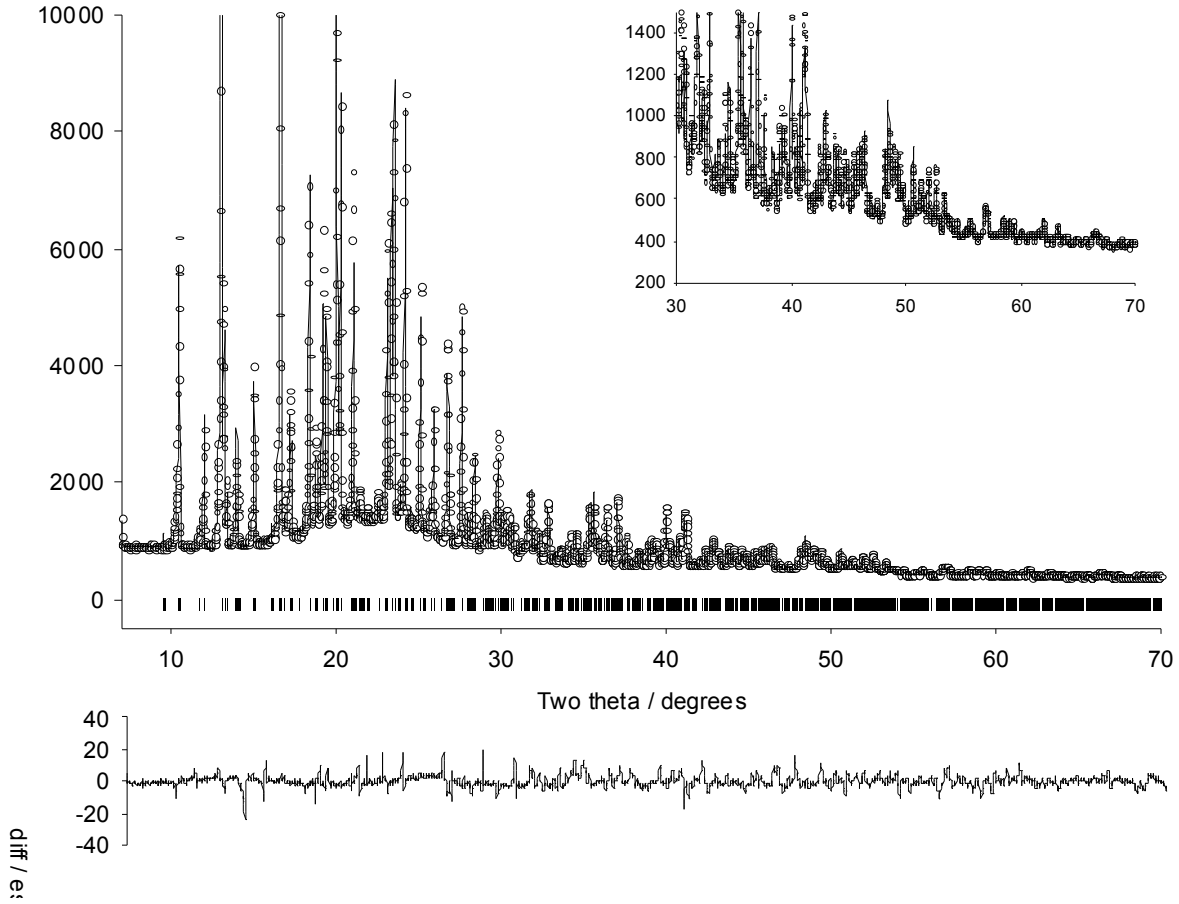

Figure 5.22 Observed profile (circles), calculated profile (line) and difference [$(y_{obs} - y_{calc})/\sigma(y_{calc})$] plot for the rigid body Rietveld refinement of salbutamol xinafoate in the range 2-70° 2θ. Inset: high-angle data 30-70° 2θ.

5.3.6 DFT calculations and unconstrained Rietveld refinement

The agreement between the geometry optimised and experimental structures is excellent, with no significant differences between the experimental structures and geometry optimised structures. This further increased confidence that the experimental structures were accurate. The RMSD values reflect the excellent agreement between the experimental and optimised structures. The RMSD values are shown in Table 5.11. Figure 5.23 shows an overlay of the refined and optimised crystal structures of salbutamol acetate. The geometry optimisations were carried out overnight on a grid system.

Table 5.11 RMSD values for experimental and optimised structures

salbutamol salt	**RMSD (Å)**
acetate	0.101
butyrate	0.11
formate	0.102
nicotinate	0.072
saccharinate	0.073
xinafoate	0.052

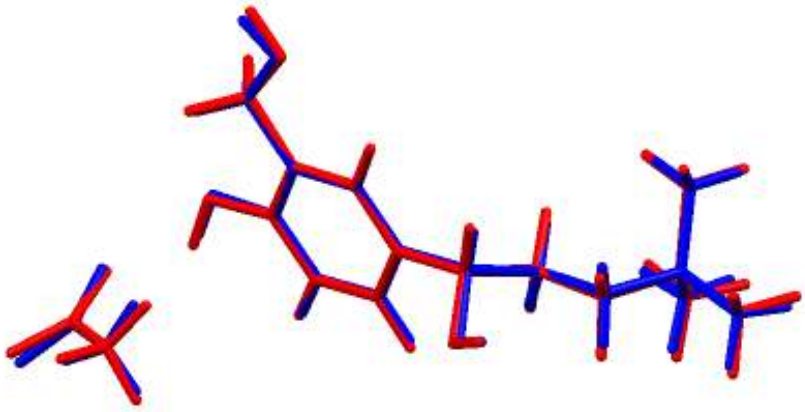

Figure 5.23 Overlay of the refined crystal structure (blue) with the CASTEP optimised structure (red) of salbutamol acetate. The agreement between the structures is excellent, and the only difference between the two structures is the more accurate location of the hydrogen atoms in the CASTEP optimised structure through small movement of C-H-O groups in the salbutamol ion.

As a final check, unconstrained Rietveld refinement was carried out on each crystal structure. It was found that the connectivity of all of the heavy atoms in the crystal structures remained intact, albeit with slight distortion, but each structural fragment was recognisable, thus lending even more confidence that the crystal structure was indeed at a minimum.

5.4 Summary

A series of organic salts of salbutamol were prepared using traditional solution based salt screening and a mechanochemical approach. The mechanochemical approach used allowed very rapid preparation of the salts; typically a reaction mixture was ground for 15 minutes. In the case of the acetate, butyrate and formate salts of salbutamol, it took up to 2 weeks for the salt to crystallise from solution but the salts were readily prepared by grinding. The crystal structures of this series of polycrystalline organic salbutamol salts were accurately determined by simulated annealing and refined by rigid-body Rietveld refinement. The crystal structures were verified by CASTEP optimisation, and in the case of salbutamol xinafoate, the crystal structure solved from powder diffraction data could be compared with the single crystal structure, to give a further insight of the accuracy of crystal structures that can be obtained purely from X-ray powder diffraction data.

Although not a necessary step in SDPD attempts, geometry optimisation calculations can help to increase the accuracy of crystal structures solved from powder diffraction data, due to the more accurate location of hydrogen atoms than can be obtained from X-ray powder diffraction data alone. In the case of the salbutamol salts, the hydrogen atoms were more accurately located due to very small changes in the orientation of hydrogen bonding groups (C-H-O groups) in the salbutamol ions. The changes in the position of the heavy atoms in these groups were, however, insignificant, as the positions of the heavy atoms in the structures were very accurately defined in the experimental structures. CASTEP calculations are therefore a useful, if computationally expensive method on enhancing the accuracy of crystal structures solved from X-ray powder diffraction data.

The use of mechanochemical salt screening, coupled with SDPD has shown that it is possible to screen an API against a wide range of pharmaceutically acceptable salt formers, with no need to await solvent evaporation or crystallisation to allow structural characterisation of the polycrystalline material. The use of these techniques may be very useful in those cases where conventional solution based crystallisation screens result in the formation of viscous oils which fail to nucleate within a reasonable timescale, as is indeed the case with many of the salbutamol salts prepared during the course of this work. Furthermore, the use of mechanochemical methods to prepare salts of an API may also be very useful when conducting extensive polymorph screening on promising salt candidates in drug development, as it may be possible to prepare and characterise polymorphs which are not obtainable by conventional crystallisation. The diffraction data and crystal structures of any such polymorphic forms could be of great importance for regulatory and patent reasons.

Chapter 6

Characterisation of X-ray amorphous pharmaceuticals using a Total Scattering Pair Distribution Function (TS-PDF) approach

6.1 Introduction

It has already been stated that salt or co-crystal formation are both effective methods of increasing the aqueous solubility and bioavailability of a poorly soluble drug. There is, however, no guarantee that it is possible to form suitable salts or co-crystals of the drug. Another method of increasing the aqueous solubility and therefore bioavailability of a poorly soluble drug is to prepare a "high energy" amorphous form of the drug. The solubility differences between crystalline and amorphous drugs can be significant. For example, the solubility of novobiocin acid is increased approximately 10-fold when this drug is converted to an amorphous form. In fact, the solubility increase can be as much as 1600 fold on conversion of a crystalline drug to the amorphous state (Hancock & Parks, 2000). Surprisingly, relatively few pharmacokinetic studies have been carried out to evaluate the improvement in bioavailability of amorphous forms of poorly soluble drugs, but those which have been carried out have shown that the bioavailability of amorphous drugs is indeed higher than that of the crystalline counterparts (DiNunzio *et al.,* 2008, Kennedy *et al.,* 2008, Lalkshman *et al.*, 2008, Ambike *et al.*, 2005). It has also been shown that the amorphous form of the vanilloid receptor antagonist AMG 517 is more soluble and has a higher bioavailability than co-crystals of the same compound. The structure of AMG 517 is shown in Figure 6.1 (Kennedy *et al.*, 2008).

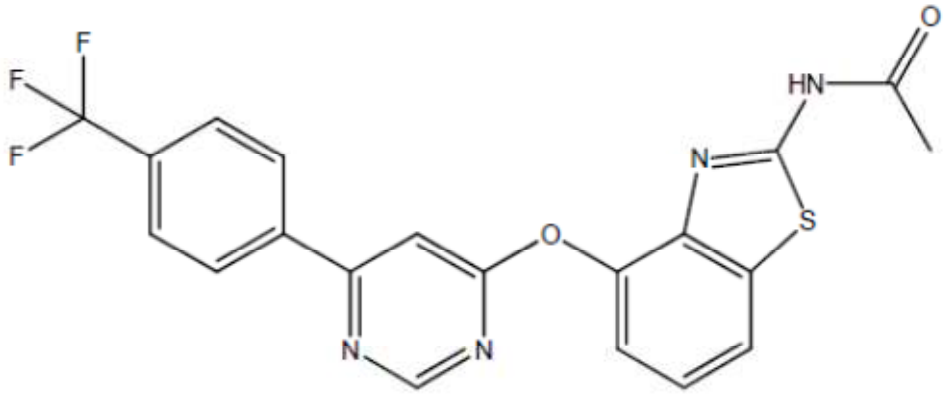

Figure 6.1 The molecular structure of AMG 517. The bioavailability of this drug is 1020ng/ml in the crystalline state, but on preparing an amorphous solid dispersion the solubility was significantly increased to 1480ng/ml (Kennedy *et al.,* 2008).

Amorphous, or 'glassy', pharmaceutical solids have faster dissolution rates because the crystal packing energy (energy needed to disrupt the crystal packing) is much lower in an amorphous solid, given the disordered nature of the material. The higher free energy state of the disordered solid leads to an increase in solubility and hence a higher rate of dissolution (Bansal *et al.*, 2007). Although the increase in solubility and bioavailability of the amorphous state can be a definite advantage, the inherent physical instability and propensity for recrystallisation of the amorphous state can make it very difficult to routinely prepare amorphous dose forms of drugs where the benefits of increased solubility and bioavailability are maintained for extended periods of time. Furthermore, amorphous materials can also be difficult to handle, which can make large scale production of amorphous drugs difficult.

6.1.1 Methods of preparing amorphous pharmaceuticals

There are several methods that may be used to prepare an amorphous form of a pharmaceutical. These methods are discussed below along with the advantages and disadvantages associated with the amorphisation method.

6.1.1.1 Milling

Milling involves grinding the material of interest to produce very small particles of the material. Milling can be used to render pharmaceuticals X-ray amorphous by mechanical disruption of the crystal lattice. The method is particularly useful for those pharmaceutical compounds that are thermolabile, so melt quenching is not an option. A potential drawback to this method is the fact that the compound can degrade due to the high levels of mechanical stress. Furthermore, local heating can cause damage to the compound if it is thermolabile. That said, cooling the grinding jar to cryogenic temperatures can remove the heat produced during grinding, and in fact the very low temperatures seem to be synergistic with the grinding, probably by making the crystal lattice brittle and easy to disrupt, helping to lead to the formation of amorphous material, with a reduced risk of thermal or mechanical degradation (Crowley & Zografi, 2002).

6.1.1.2 Melt-quenching

Melt-quenching is another method of producing X-ray amorphous pharmaceuticals. Typically, the melt is held at high temperature for a short while (1-2 minutes) to destroy any seeds of the crystalline form. This ensures that the orientation of the molecules in the melt is totally random. Rapid, deep quenching of the melt then locks the random orientation of the molecules into the structure, producing a supercooled liquid. An obvious drawback to this

technique is the risk of thermal degradation of the material. However, if the material is thermally stable, the melt-quench technique is often a reliable method of preparing an amorphous material.

6.1.1.3 Melt extrusion

Melt-extrusion is a similar technique to melt-quenching, where the material is melted, but along with a pharmaceutically acceptable polymer. The polymer acts as a crystallisation inhibitor, typically by vastly increasing the T_g of the material, thus preventing molecular reorientation and eventual recrystallisation. The main advantage of the method is that the drug and the polymer are co-melted, so this avoids the need to carry out any formulation studies. A disadvantage is the fact that since the drug must be heated to 10-15° above the melting point, the technique cannot be applied to thermolabile drugs.

6.1.1.4 Formation of amorphous solid dispersions (ASDs)

An amorphous solid dispersion can readily be prepared by dissolving an API together with a pharmaceutically acceptable polymer then rapidly removing the solvent under vacuum. The method is relatively gentle in terms of impact on chemical stability, and is also scalable. The choice of polymer is normally governed by the intended administration route; for example if the drug is for oral administration, the most commonly used polymer is PVP (polyvinylpyrrolidone) as this polymer is biocompatible with this administration method. The main advantages of the method have already been stated; however, the main disadvantage of the technique is the use of relatively large amounts of organic solvents. This can lead to toxicity concerns, especially if it is necessary to use ICH class 2 solvents. The disordered nature of amorphous solids is actually one of the main barriers to the widespread acceptance

of amorphous dosage forms of poorly soluble drugs. An amorphous drug is thermodynamically unstable, due to the high entropy and free energy relative to the crystalline state; thus there is a thermodynamic driving force towards spontaneous recrystallisation. Recrystallisation of an amorphous drug could lead to the loss of any solubility improvement seen in the amorphous form or the formation of a solid with undesirable biopharmaceutical or mechanical properties. The use of hydrophilic organic polymers has been shown to inhibit recrystallisation of amorphous drugs for long periods (Taylor & Zografi, 1997a, Taylor & Zografi, 1997b, Newman *et al.*, 2008, Tobyn *et al.*, 2009, Kennedy *et al.*, 2008).

6.1.2 Structural Characterisation and Analysis of the amorphous state

Little is known about molecular packing in the amorphous state, as traditional diffraction methods cannot be used to characterise amorphous materials, due to the lack of Bragg diffraction from the sample. Spectroscopic techniques have been used to examine intermolecular interactions at the macroscopic level (Taylor & Zografi, 1997a, Taylor & Zografi, 1997b, Kaushal *et al.*, 2008) but little has been stated about the packing of amorphous pharmaceuticals at the microscopic level, other than that the molecules are likely to pack in such a way that minimises the local free energy (random close packing) or that the glassy material is characterised by a single hydrogen-bonding network (Bates *et al.*, 2006). The poorly soluble, BCS class II drugs carbamazepine (CBZ) and indomethacin (IND) have been studied extensively in the amorphous state (Patterson *et al.*, 2005, Sauolainen *et al.*, 2007, Savolainen *et al.*, 2009, Hedoux *et al.*, 2008, Zeitler *et al.*, 2007, Andronis & Zografi, 2000, Crowley & Zografi, 2002, Carpentier *et al.*, 2006). However, all of these studies have involved the characterisation of the amorphous materials at the macroscopic level; no characterisation at the molecular (microscopic) level has been reported. The structure of

indomethacin is shown in Figure 6.2.

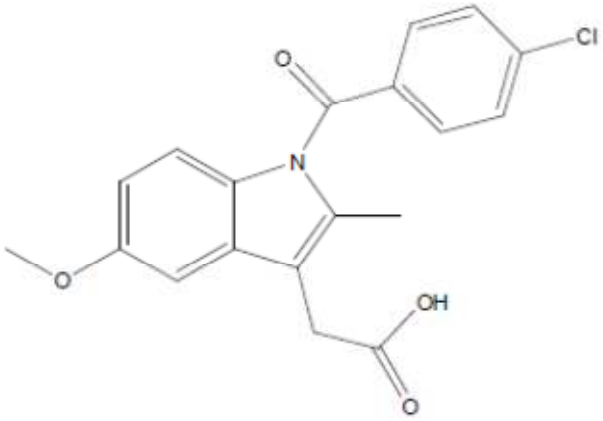

Figure 6.2 Molecular structure of indomethacin

CBZ and IND were amorphised in the laboratory by a melt-quench method, and the resulting amorphous forms were characterised in the laboratory. Samples of amorphous CBZ and IND were also examined at Advanced Photon Source (APS) at the Argonne National Laboratory, Argonne, Illinois using a total-scattering pair distribution function (TS-PDF) approach in collaboration with the Billinge group from Columbia University, New York. The TS-PDF approach was able to provide useful structural information at the molecular level on an otherwise X-ray amorphous sample. Additionally, PDF data collected at APS were compared with simulated TS-PDFs, using copper (Cu, $\lambda = 1.5406$A), silver (Ag, $\lambda = 0.559$A) and molybdenum (Mo, $\lambda = 0.709$A) calculated from APS data to determine if laboratory diffractometers using metal anodes can allow data to be collected to a sufficiently high Q range to allow reliable fingerprinting of an amorphous solid.

6.2 Preparation and characterisation of amorphous pharmaceuticals

6.2.1 Preparation of amorphous CBZ and IND

CBZ was made amorphous by melting a sample at 200°C on a glass microscope slide. The sample was held at this temperature for one minute to ensure that all of the crystalline material had melted. The slide containing the molten CBZ was then immediately immersed in liquid nitrogen to form a glass, following a previously described method (Zeitler *et al.*, 2007). The CBZ glass was examined by polarised light microscopy and no birefringence was observed. The CBZ glass was then scraped from the microscope slide and gently ground in an agate mortar. The resulting powder was then stored in a desiccator to await further analysis. Amorphous IND was prepared by melting a sample at 170°C on a glass microscope slide then cooling the slide in liquid nitrogen. The melt quenched material was then treated in the same manner as the melt-quenched CBZ.

6.2.2 Laboratory characterisation of amorphous CBZ and IND

6.2.2.1 Laboratory XRPD

Samples of melt-quenched CBZ and IND were confirmed as being amorphous by XRPD 'fingerprinting' in the range 4-35° 2θ. Samples were mounted on a thin film of Kapton and the step size was 0.017° 2θ. The observed amorphous "haloes" due to the lack of Bragg peaks confirmed an absence of long-range order in the melt-quenched samples. Good quality datasets were also collected from the amorphous pharmaceuticals. Samples were lightly ground and packed into Kapton capillaries (1mm diameter). The capillaries were then mounted in a goniometer and data was collected in the range 2-40° 2θ, step size 0.017° 2θ the step time was 10s. The capillary datasets were collected at 100K, which was achieved by cooling the sample with a flow of cold nitrogen gas from a cryostream device fitted to the powder diffractometer.

6.2.2.2 Thermal analysis

Samples (3-5mg) of the melt-quenched pharmaceuticals were lightly ground and sealed in 25µl aluminium pans with pierced lids. The samples were then heated from 20°C to 10°C past the melting point of the crystalline pharmaceutical (192°C for CBZ, 160°C for IND) under a nitrogen purge in order to determine the glass transition temperature (Tg) and crystallisation temperature (Tc), samples were run in triplicate.

6.2.2.3 Study of recrystallisation kinetics

The amorphous pharmaceuticals were stored at different temperatures; 20, 50, 70 and 90°C. Samples were examined by XRPD fingerprinting at 15 minute intervals in an attempt to find the optimum temperature to induce recrystallisation of the amorphous pharmaceuticals within a reasonable time. The recrystallisation of the amorphous pharmaceuticals was also studied *in situ*. Lightly ground samples were packed into Kapton capillaries, and the samples were heated using a stream of nitrogen gas from the cryostream. A series of short powder diffraction scans (0.1s per step) in the range 2-40° 2θ were carried out to determine the time taken for recrystallisation at a given temperature.

6.2.2.4 Preparation of pure phase pharmaceutical polymorphs.

Both CBZ and IND are polymorphic. CBZ has five polymorphic forms, but form IV is not readily prepared and can only be prepared in the presence of hydroxypropylcellulose (Lang *et al.*, 2002). CBZ form V can only be prepared by templating on form II dihydrocarbamazepine (Arlin *et al.*, 2011) so given the difficulties with preparation, CBZ forms IV and V were not prepared for these studies. CBZ form III (β CBZ) is the commercially available form and was used as received. CBZ form II (α CBZ) was prepared by dissolving CBZ in 1-hexanol at 60°C then cooling the solution on ice. CBZ form I (γ CBZ) was prepared by annealing a

sample of CBZ form III at 185oC overnight. Phase purity was confirmed by successfully Pawley fitting the powder patterns to the published unit cell parameters. The commercial form of IND is γ IND, which was used as received. The metastable α polymorph was prepared by dissolving the γ polymorph in warm ethanol then precipitating using deionised water (Crowley & Zografi, 2002). An unstable polymorph of IND (δ IND) has been shown to crystallise from the melt (Wu & Yu, 2006) but this polymorph was not prepared for these studies. All materials were ground and sieved (38μm pore size) prior to analysis in the laboratory.

6.2.3 Characterisation of materials at APS

Amorphous CBZ and IND were prepared fresh at the synchrotron as previously described. Crystalline CBZ form I, CBZ form III, γ-IND and α-IND which had previously been ground and sieved was loaded into Kapton capillaries with no further treatment necessary. The freshly prepared amorphous samples were also lightly ground and sieved before being filled into Kapton capillaries immediately before analysis. Data were then collected as described in § 3.2.2.2.

6.3 Results and discussion

6.3.1 Laboratory characterisation of the amorphous pharmaceuticals

6.3.1.1 Laboratory XRPD characterisation of amorphous CBZ

In the laboratory X-ray powder diffraction experiments, only a characteristic halo for the amorphous forms of CBZ and IND was observed. No other information was immediately available from the powder diffraction patterns, other than that the halo observed for IND was different from the halo observed for CBZ. Given the fact that these compounds are totally different, this is to be expected since the local packing of different molecules must also be different. The amorphous haloes collected from samples of amorphous CBZ and IND in the laboratory are shown in Figure 6.3.

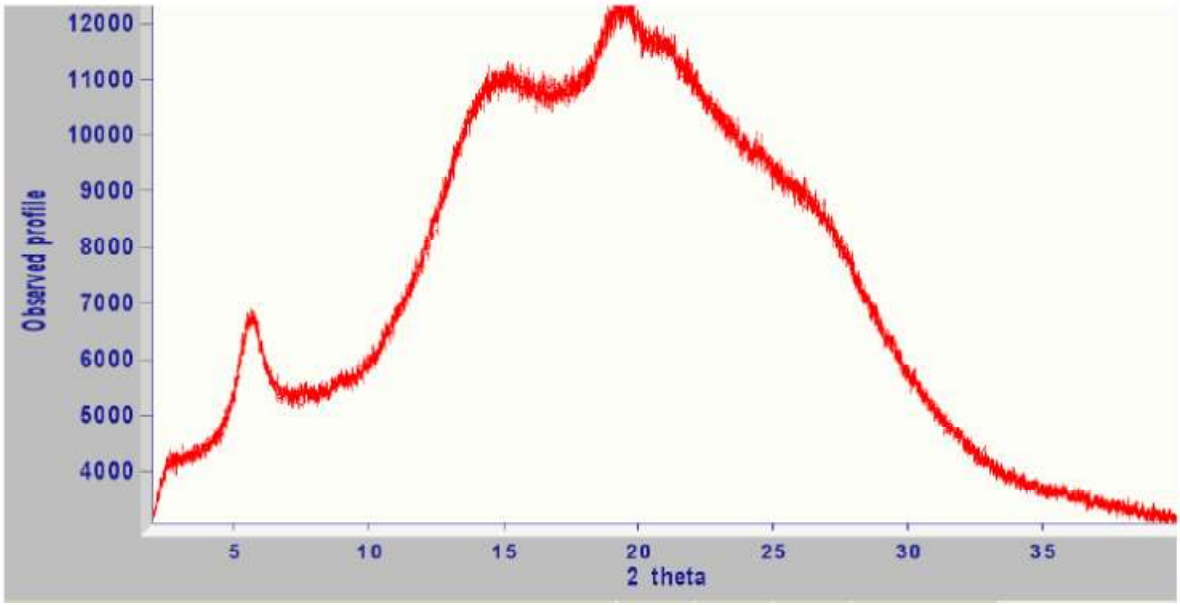

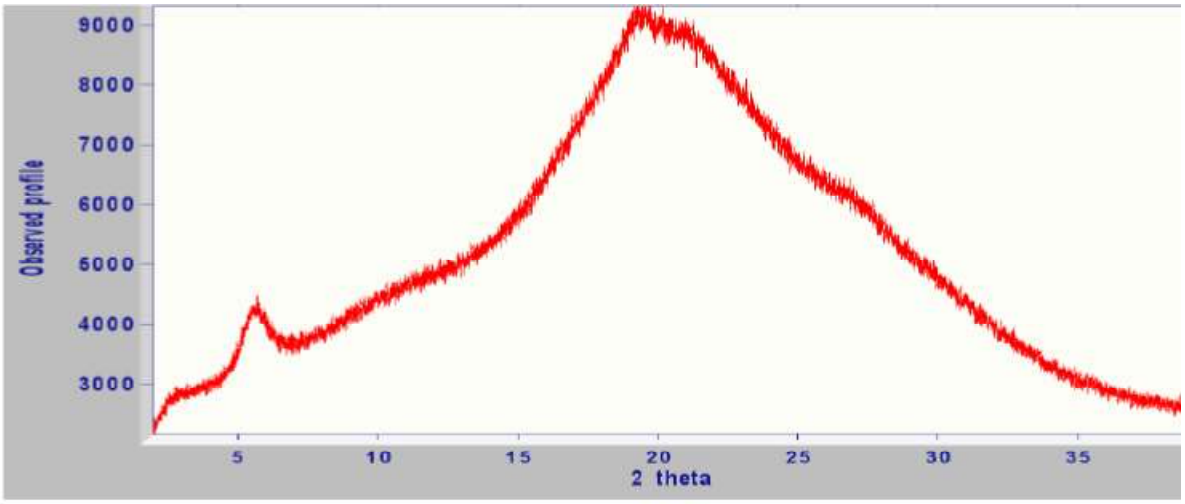

Figure 6.3 amorphous 'haloes' observed in laboratory XRPD experiments at 100K Top: amorphous CBZ, Bottom: amorphous IND. The only information immediately obtainable from laboratory XRPD is that the local packing in CBZ is different to that in IND, which is unsurprising. The peak at ca. 6° 2θ which is present in both the IND and CBZ patterns is due to the Kapton capillary.

6.3.1.2 Thermal analysis of amorphous CBZ

Thermal analysis of the amorphous pharmaceuticals clearly showed the glass transition, recrystallisation and melting events. The glass transition temperature of CBZ has previously been reported to be in the range 46.85-61.85°C and the crystallisation temperature has been reported as 83.85°C (Zeitler *et al.*, 2007). It was also stated that the form obtained by recrystallisation of amorphous CBZ at this temperature is CBZ form III, confirmed by Terahertz pulsed spectroscopy experiments (Zeitler *et al.*, 2007). This study claimed that CBZ form III was crystallising due to the observance of the hydrogen-bonded carboxamide dimer which is characteristic of CBZ. However, all known polymorphs of CBZ crystallise with this dimer, so the spectral analysis is not definitive proof that CBZ crystallises from the amorphous as CBZ form III. The melt-quenched CBZ prepared for these studies had a glass transition temperature of 41.3°C, a recrystallisation temperature of 81.95°C followed by a polymorph transition at 141.71°C before melting at 167.34°C. DSC runs were carried out in triplicate. The glass transition temperature (T_g), crystallisation temperature (T_c) polymorph

transition temperature (T_{trans}) and melting temperature (T_f) are listed in Table 6.1. A representative DSC trace of amorphous CBZ is shown in Figure 6.4.

Table 6.1 Thermal properties of melt-quenched CBZ.

Sample number	T_g/°C	T_c/°C	T_{trans}/°C	T_f/°C
1	43.69	83.08	141.65	170.55
2	42.45	81.31	141.8	170.39
3	37.75	81.45	141.67	161.07

It is clear from Table 6.1 that the melt-quench method developed for these studies is reproducible and can be used to reliably form the same amorphous phase of CBZ. From Table 6.1, it is also evident that the melting point of the recrystallised CBZ is quite different from that of crystalline CBZ (Tf = 192°C). Also, in Figure 6.4, the DSC peaks are broad. The broad DSC peaks could be due to the small crystallite size in the sample (poor crystallinity), but the crystallite size should not have such a high influence on the melting point of the sample. In a study of different preparative techniques to prepare amorphous pharmaceuticals (Patterson *et al*., 2005) it has been shown that recrystallised melt quenched CBZ melts at 180°C, which is also below the expected temperature of ≈ 190°C. It was suggested that the significant depression of the melting point could be due to the crystallisation of more than one polycrystalline phase from the amorphous (Patterson *et al*., 2005). Another possibility for the depression of melting point is the presence of degradation products. However, when meltquenched CBZ was examined by HPLC (Patterson *et al*., 2005), the material was found to be 98.74% pure CBZ (compared with 99.12% for crystalline CBZ). The laboratory data collected from recrystallised melt quenched CBZ was successfully Pawley fitted to CBZ form I cell parameters, suggesting that no significant degradation of CBZ had occurred during the melt-quench experiments in the laboratory.

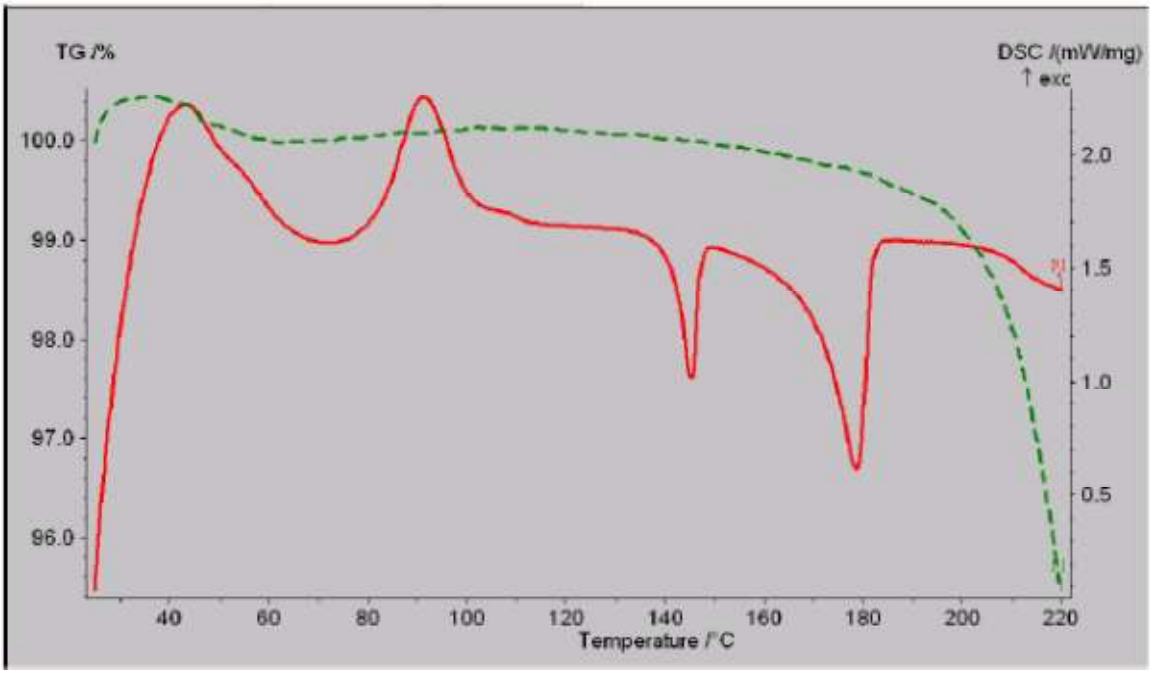

Figure 6.4 Typical DSC trace for melt-quenched CBZ showing the recrystallisation of CBZ (as CBZ form III), polymorph transition (CBZ form III transforms to CBZ form I) and melting of CBZ form I (CBZ always converts to form I before melting).

6.3.1.3 Study of recrystallisation kinetics of amorphous CBZ

Initially, samples of amorphous CBZ were prepared as described in § 6.2.1, but rather than scraping the melt-quenched CBZ from the microscope slides, the slides were stored at four different temperature as described in § 6.2.2.3. The samples were then examined by polarised light microscopy at 15 minute intervals and the time for birefringence to be observed was noted. Samples showing birefringence were analysed by XRPD fingerprinting to confirm that recrystallisation was underway. It was found that storing the samples at 90°C lead to much faster recrystallisation, as expected since the recrystallisation temperature of melt-quenched CBZ has been determined as being 81.95°C in these studies. Storing the samples above the glass transition temperature but below the crystallisation temperature did decrease the time taken for recrystallisation, but the optimum temperature for rapid recrystallisation was determined to be 90°C, with a total annealing time of 15 minutes.

In situ recrystallisation experiments were carried out using ground and sieved CBZ. The sample was heated to 90°C and a series of short (0.1s step time) scans were carried out in the range 2-40° 2θ, which equated to ca. three minutes of data collection per scan. However, setting the Cryostream to 90°C did not lead to crystallisation as quickly as storing a sample in an oven set to 90°C, this was probably due to differences in temperature control or sample presentation. Setting the Cryostream temperature to 96°C did however induce rapid recrystallisation during the *in situ* recrystallisation experiments. Figure 6.5 shows the results of annealing a sample of amorphous CBZ in a Kapton capillary at 96°C for 15 minutes. Crystallisation was monitored for a further 15 minutes and was complete after 30 minutes of heating. The resulting crystalline phase was identified as CBZ form I by comparison of the recrystallised powder pattern with powder patterns of pure polymorphs and further confirmed by successful Pawley refinement of the recrystallised samples to the form I unit cell parameters.

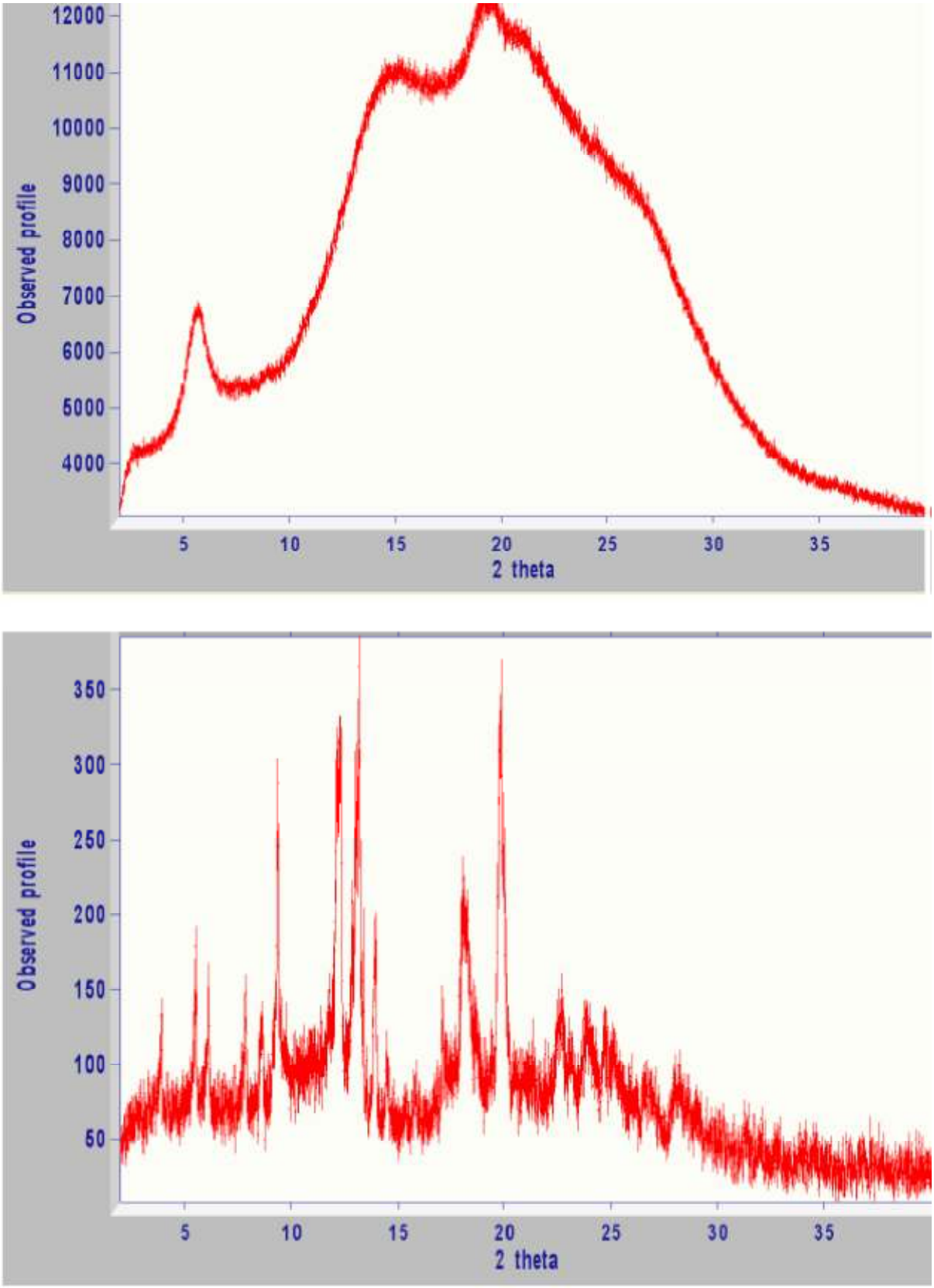

Figure 6.5 Effect of annealing an amorphous sample of CBZ at 96°C for 15 minutes. Top: initial x-ray amorphous halo. Bottom: emergence of crystalline CBZ form I peaks from the amorphous phase after 15 minutes heating in a Kapton capillary.

6.3.2 Total Scattering Pair Distribution Function analysis of the pharmaceuticals

Conventional X-ray powder diffraction techniques are very useful for characterising crystalline materials, which are characterised by a periodic arrangement of atoms in the crystal lattice. However, when the crystal lattice is disrupted, as is the case with amorphous materials, then no Bragg diffraction is observed thus conventional XRPD techniques lose their ability to characterise the solid material. However, Total Scattering Pair Distribution Function experiments can allow structural characterisation of X-ray amorphous materials. As in a traditional XRPD experiment, Bragg intensities are observed in a TS-PDF experiment. A very important difference is the fact that in a TS-PDF experiment it is also possible to observe and extract meaningful information from diffuse intensities, which is not possible in a traditional XRPD experiment. Thus, TS-PDF experiments allow characterisation of both long range and very local structure of the solid under study. It is not straightforward to look at PDF data and gain an understanding of the local structure, but it is relatively straightforward to pick out structural features of the material. For example, if the sample contains an aromatic ring, then intense peaks will be observed at 1.4 A and 2.4 A corresponding to nearest neighbour and next-nearest neighbour carbon atom distances in the aromatic ring. As described in § 1.9.4, PDF gives the probability of finding a pair of atoms separated by a given distance, r. The number of atoms with this specific pairing can be related to the intensity of the peak in the PDF. It is important to note that conventional PDF and TS-PDF both provide exactly the same information, the only difference being the experimental set-up. However, TS-PDF has a higher Q-space resolution and therefore a higher information content than conventional PDF. In this work, the TS-PDF data were collected by the use of short wavelength synchrotron radiation (0.137A) and use of an appropriate data collection strategy allowed sufficiently high Q-range data to be collected, which in turn provided sufficient resolution in real space for quantitative structural analyses to be performed.

It is not however, necessary to visit central facilities in order to collect TS-PDF data, as will be discussed later. Indeed, it has been shown that use of laboratory powder diffractometers can indeed yield useful TS-PDF data, but this is dependent on the instrument anode and consequently the wavelength of X-rays. The work carried out at APS Argonne showed how useful the technique of TS-PDF may be in providing unambiguous fingerprints of amorphous pharmaceuticals.

6.3.2.1 Analysis of CBZ by Total Scattering Pair Distribution Function

CBZ was the most extensively characterised material at the beamline, due to time constraints. The analysis of TS-PDF data was carried out by the Billinge group in Columbia University, New York. In the context of this thesis, the contribution to this work by was to prepare samples for the experiments and to study the recrystallisation of the amorphous pharmaceuticals using laboratory XRPD and DSC experiments. Crystalline CBZ form I and CBZ form III were used to generate reference TS-PDF traces for comparison with the amorphous material. The total scattering data, F(Q), for a sample of melt-quenched CBZ measured over a wide Q-range and properly normalised is rich in information compared to data collected from melt-quenched CBZ in the laboratory. Close inspection shows that there is no clear Bragg diffraction in melt-quenched CBZ (i.e. only diffuse scattering was observed from the TS-PDF experiment). The F(Q) data distinguishes polycrystalline CBZ form III and polycrystalline CBZ form I (Figure 6.6a and c respectively). From Figure 6.6, the F(Q) data show that melt-quenched CBZ resembles CBZ form III more than CBZ form I.

Fourier transforming the F(Q) data to G(r) (i.e. the TS-PDF) allows comparisons to be made in real space. There is a very good resemblance between the TS-PDF of CBZ form III and the TS-PDF of the melt-quenched sample (Figure 6.6d and e respectively).

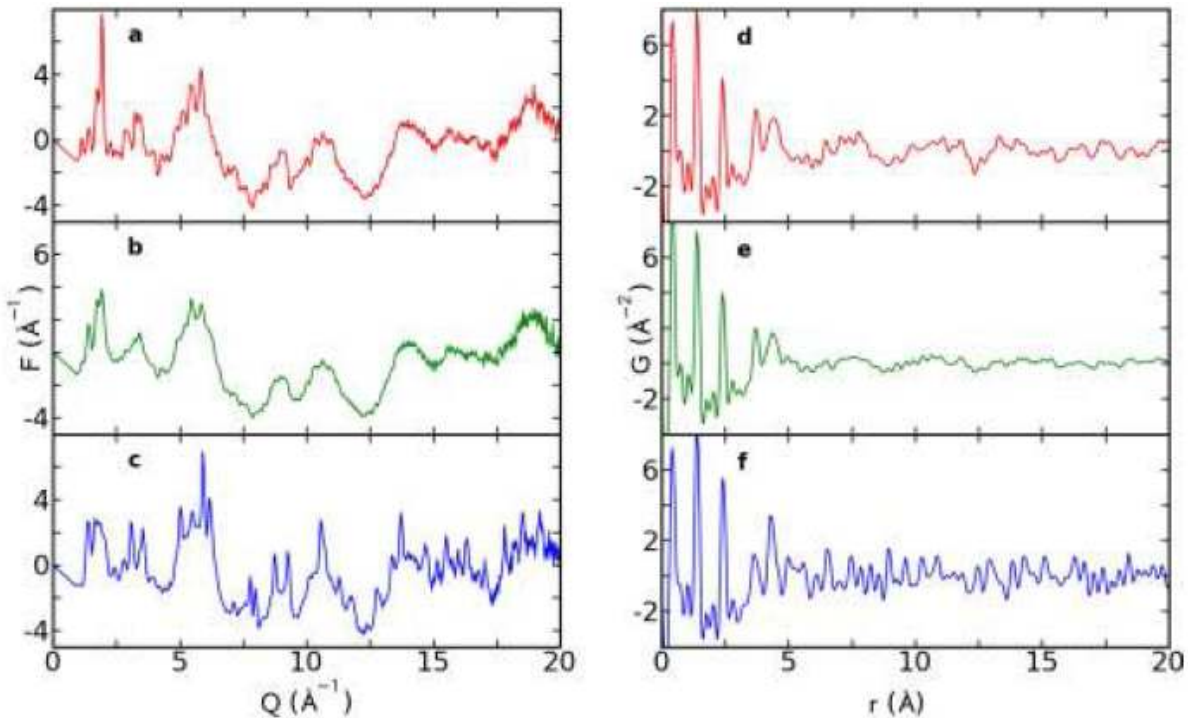

Figure 6.6 Total scattering diffraction patterns and TS-PDF data collected at beamline ID-11-B. Panels (a) and (d) correspond to CBZ form III. Panels (b) and (e) correspond to a sample of melt-quenched CBZ and panels (c) and (f) correspond to CBZ form I. (a), (b) and (c) show the total scattering in the form $F(Q)$ and (d), (e) and (f) show the data in the form of $G(r)$. Of particular note is the similarity of the data collected from the amorphous sample and CBZ form III. Both are different to the data collected from CBZ form I.

From the above Figure, the most important point to note is that the local packing of the molecules in the amorphous melt-quenched sample of CBZ is extremely similar to the arrangement of the molecules in crystalline CBZ form III; i.e. the intermolecular interactions in the amorphous sample and in CBZ form III are essentially the same (Billinge *et al.,* 2010). Full profile comparisons of the TS-PDFs in the range dominated by intermolecular interactions (3-20Å) for the different modifications of CBZ (form I, form III and amorphous) using polySNAP (Barr *et al.,* 2004) yielded a correlation coefficient of 0.8389 for the TS-PDFs of CBZ form III and melt-quenched CBZ (a perfect match has a correlation coefficient of 1.0). The next closest similarity was between melt-quenched CBZ and CBZ form I, but this time the correlation co-efficient was only 0.6124. The polySNAP analyses confirmed this

visual observation that there is a similarity between the TS-PDFs of CBZ form III and melt-quenched CBZ. Table 6.2 shows the numerical correlation between the PDFs of different solid forms of CBZ calculated in polySNAP.

Table 6.2 Correlation co-efficients between the solid forms of CBZ. Correlations higher than 0.8 are shown in bold (except when the correlations are unity).

100K APS data	CBZ form I	CBZ form III	quench CBZ
CBZ form I	1	0.4467	0.6124
CBZ form III	0.4467	1	**0.8389**
quench CBZ	0.6124	**0.8389**	1

Given the very good agreement between the melt quenched CBZ and CBZ form III TSPDFs, the structural similarity between the samples was examined in more detail. The TSPDF of CBZ form III was modified by attenuating the TS-PDF peaks in the high-r region using a spherical characteristic function to simulate the effects of reducing structural coherence (or long-range ordering), assuming spherical particles (Billinge *et al.,* 2010). The range of structural coherence was determined to be 4.5nm using this approach. The attenuated TS-PDF of CBZ form III was compared with the TS-PDF of melt-quenched CBZ in polySNAP, this time yielding a correlation co-efficient of 0.8601. The excellent agreement between the attenuated TS-PDF of CBZ form III and the TS-PDF of melt-quenched CBZ is definitive proof that the local packing in melt-quenched CBZ is that of CBZ form III but with a structural coherence range of 4.5nm. Figure 6.7 shows the overlay between the attenuated TS-PDF of CBZ form III and the TS-PDF of melt-quenched CBZ.

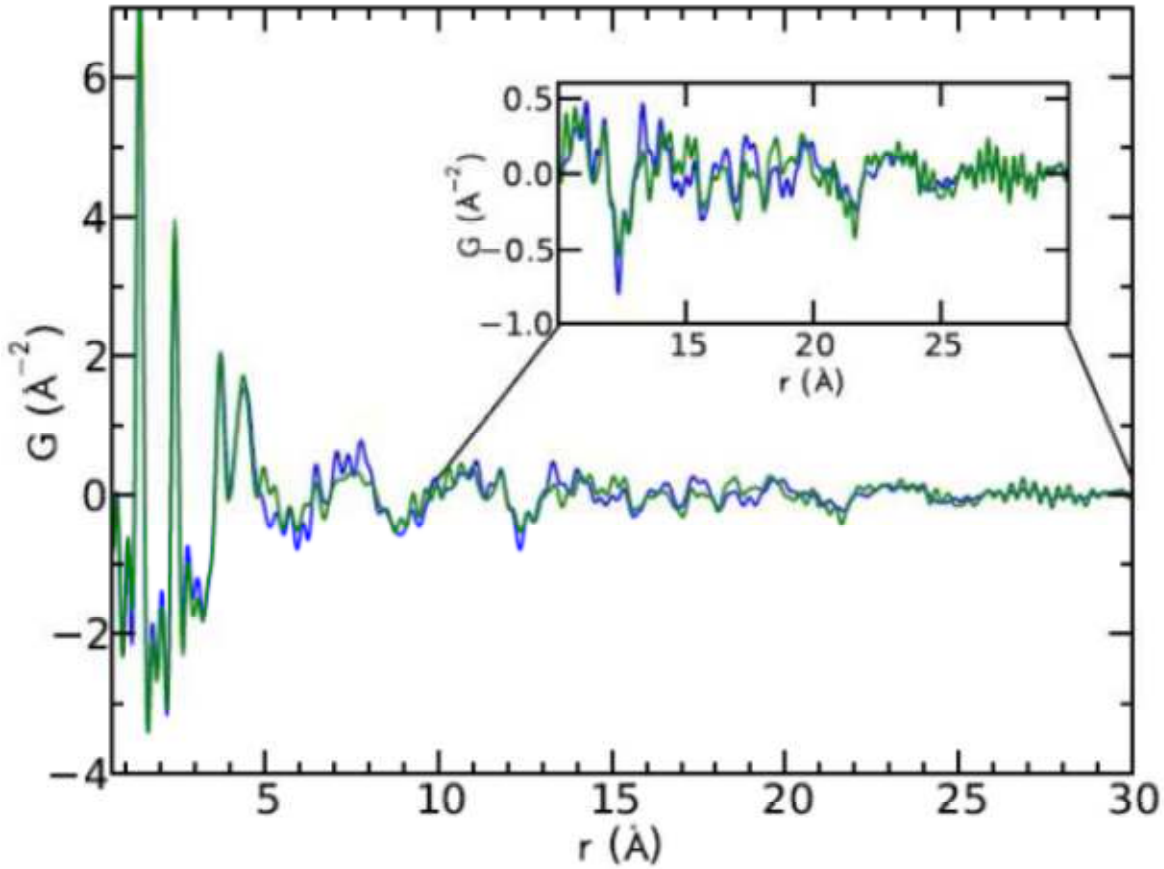

Figure 6.7 Comparison of the TS-PDF from melt-quenched CBZ (green) and the attenuated TS-PDF (particle size 4.5nm) of CBZ form III (blue). The polySNAP correlation coefficient is 0.8601.

An interesting question posed by Figure 6.7 is whether melt-quenched CBZ is made up of discrete 4.5nm crystallites of CBZ form III (i.e. melt-quenched CBZ is actually nanocrystalline CBZ form III) or if the sample is truly a homogenous amorphous structure with short range CBZ form III like packing. Given the fact that as r increases, the sharpness of the TS-PDF peaks is preserved, albeit with reduced amplitude, it seems that "amorphous" melt-quenched CBZ is in fact nanocrystalline, rather than truly amorphous.

6.3.2.2 Analysis of IND by Total Scattering Pair Distribution Function

IND was briefly characterised at the beamline. The metastable α-polymorph was prepared at the beamline, as was melt-quenched IND. TS-PDF data were collected from the α, γ and melt-quenched phases of IND. The F(Q) data collected from a sample of melt-quenched IND showed the sample had no clear Bragg diffraction peaks (X-ray amorphous) but the diffuse scattering was rich in structural information. From Table 6.3, the highest correlation coefficient from full profile comparisons of the TS-PDFs of α, γ and melt-quenched IND in polySNAP was 0.6770, which was returned from comparison of the α-IND and meltquenched IND phases (Billinge *et al.,* 2010). All other correlation co-efficients were less than 0.5. Thus, The TS-PDF data shows that the local structure of melt-quenched IND at 100K is different from the crystalline α and γ forms. This data contradicts the suggestion based on crystallisation and spectroscopic evidence that below Tg (315K) amorphous IND has a local structure similar to the γ form with dimeric hydrogen bonding. Linear combinations of the α and γ phases did not give good agreement with the TS-PDF from the melt-quenched sample. The unstable δ form of IND can be recrystallised from the glassy amorphous phase (Wu & Yu, 2006) but comparison of TSPDF data collected from this polymorph with the TS-PDF of melt quenched IND was not possible at the time of the experiment. However, the experiments showed that TS-PDF can readily characterise distinct local packing in melt-quenched IND. As with CBZ, the melt-quenched sample of IND gave rise to TS-PDF data with oscillations apparent over the whole Q range, and extending beyond 20A indicating that melt-quenched IND is also nanocrystalline rather than truly amorphous. The TS-PDF data collected from IND is shown in Figure 6.8.

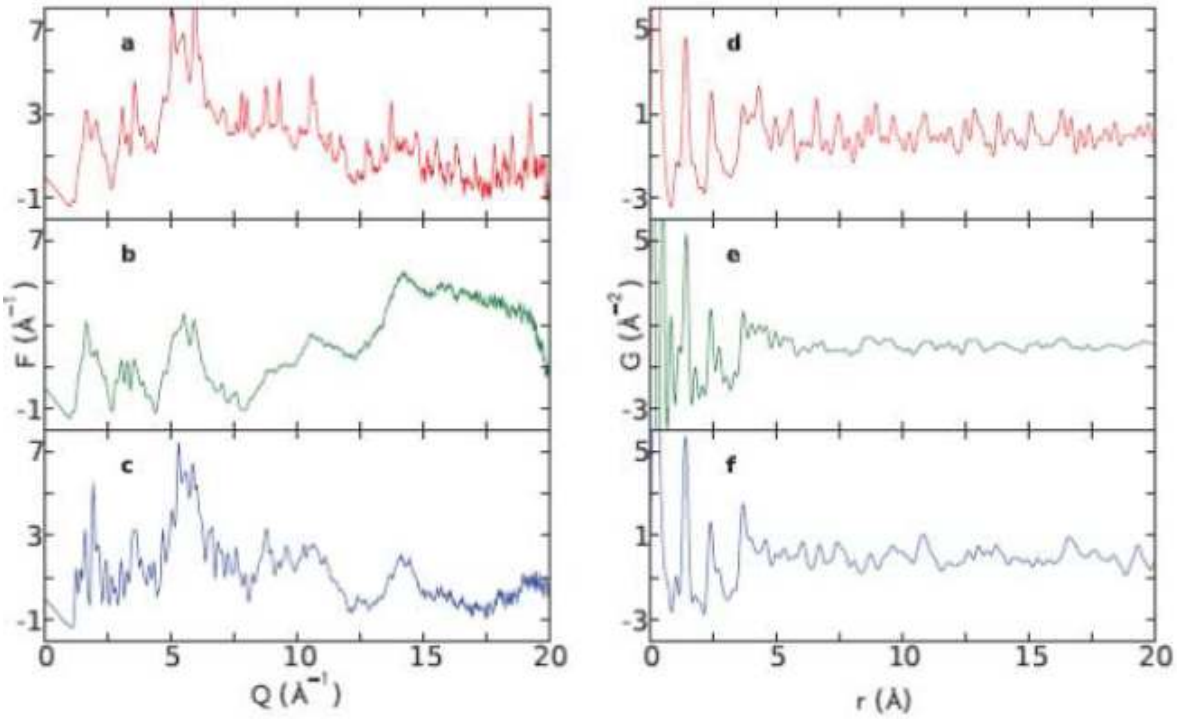

Figure 6.8 Total scattering diffraction patterns and TSPDFs of IND samples. The total scattering data shows that the local packing in the melt-quenched sample (b) is distinct from that in α IND (a) and γ IND (c). After Fourier transformation of the total scattering data to obtain the TS-PDF (in G(r)) to allow comparison in real space, it is also clear that the local packing in melt-quenched IND (e) is distinct from that found in the α polymorph (d) or the γ polymorph (f).

Table 6.3 correlation co-efficients between the solid forms of IND

100K APS data	αIND	γIND	quench IND
α-IND	1	0.4057	0.677
γ-IND	0.4057	1	0.4886
quench IND	0.677	0.4886	1

Whilst good quality TS-PDF data can be obtained using very hard X-rays or neutrons, it is also possible to obtain useable PDF data without the need to visit central facilities for data collection. For instance, it is perfectly feasible to collect data on a laboratory diffractometer, depending on the anode material used. For example it possible to obtain useful data using a molybdenum (Mo) anode, with a wavelength of 0.709A or a silver (Ag) anode, with a wavelength of 0.556A. The fact that for Mo and Ag sources, λ is a factor of 2-3 times smaller than that of a copper (Cu) anode (wavelength 1.5406A) used to collect conventional powder diffraction data means that higher Q values can be accessed for any given diffraction angle. At beamline ID-11-B, the total scattering data were Fourier transformed with a Qmax of 20A-1.

It is also possible to achieve this resolution by collecting total scattering data in the laboratory, using a Ag anode. That said, a problem with Ag sources is very weak intensities, and this necessitates very long data collection times. A possible solution to this problem is to use a laboratory diffractometer with a Mo anode, as this setup offers several advantages over the use of a Ag anode, such as higher incident flux, increased X-ray scattering and higher detector efficiency. However, the use of synchrotron radiation with a very short wavelength allows sufficient statistics to be collected over a wide Q-range in a short time, as compared to many hours if a laboratory instrument using either a Ag or Mo anode is utilised.
Although the best data (in terms of Q-space resolution) were obtained using synchrotron radiation, synchrotron beam time must be booked well in advance, and it may be necessary to travel considerable distances in order to carry out an experiment at a synchrotron. As a follow-up to the work carried out at APS Argonne, it was decided to test the ability of laboratory diffractometers using different anode materials to produce useful TS-PDF data. It

was found that laboratory instruments equipped with Cu, Ag and Mo anodes gave very different TS-PDF data (Dyhkne *et al.,* 2011). This is unsurprising, as the Qmax and therefore the information content of the TS-PDF data differ greatly. During the course of the work described in this thesis, fingerprinting using a Cu anode was in the range 2-40o 2θ, which works well for comparing and/or indexing peaks from a crystalline sample. However, this set-up does not provide much Q-space resolution (Q_{max} is 2.8A-1) in a TS-PDF pattern, which makes fingerprinting of an X-ray amorphous form difficult. However, as has been said, use of Ag or Mo anodes can yield better TS-PDF data in the laboratory. In order to test the ability of laboratory TS-PDF data to differentiate between local packing of X-ray amorphous pharmaceuticals, it would be useful to collect data (from the same sample) using Cu, Mo and Ag anodes. However, to provide a uniform comparison, data for the 3 anode types were simulated from data collected at beamline ID-11-B up to the relevant Q_{max} for each anode type, as shown in Table 6.4 (Dykhne *et al.,* 2011).

Table 6.4 Maximum ranges for laboratory diffractometer anodes to yield TS-PDF data.

Anode	$2\theta_{max}$	Q_{max}
Cu	160°	8.0Å^{-1}
Mo	90°	12.5Å^{-1}
Ag	90°	15.9Å^{-1}

From the above table, 2θmax is defined as the maximum 2θ value obtainable using a Cu anode, and a reasonable 2θ which corresponds to a short experimental measurement time for Mo and Ag anodes. Qmax is the maximum Q-space resolution that can be achieved under

these conditions. Figure 6.9 shows simulated melt-quenched CBZ TS-PDF data for Cu, Mo and Ag anodes. The synchrotron data and low-angle Cu data (Qmax 2.8A-1) are shown for completeness. TS-PDF data for crystalline CBZ form III are also shown.

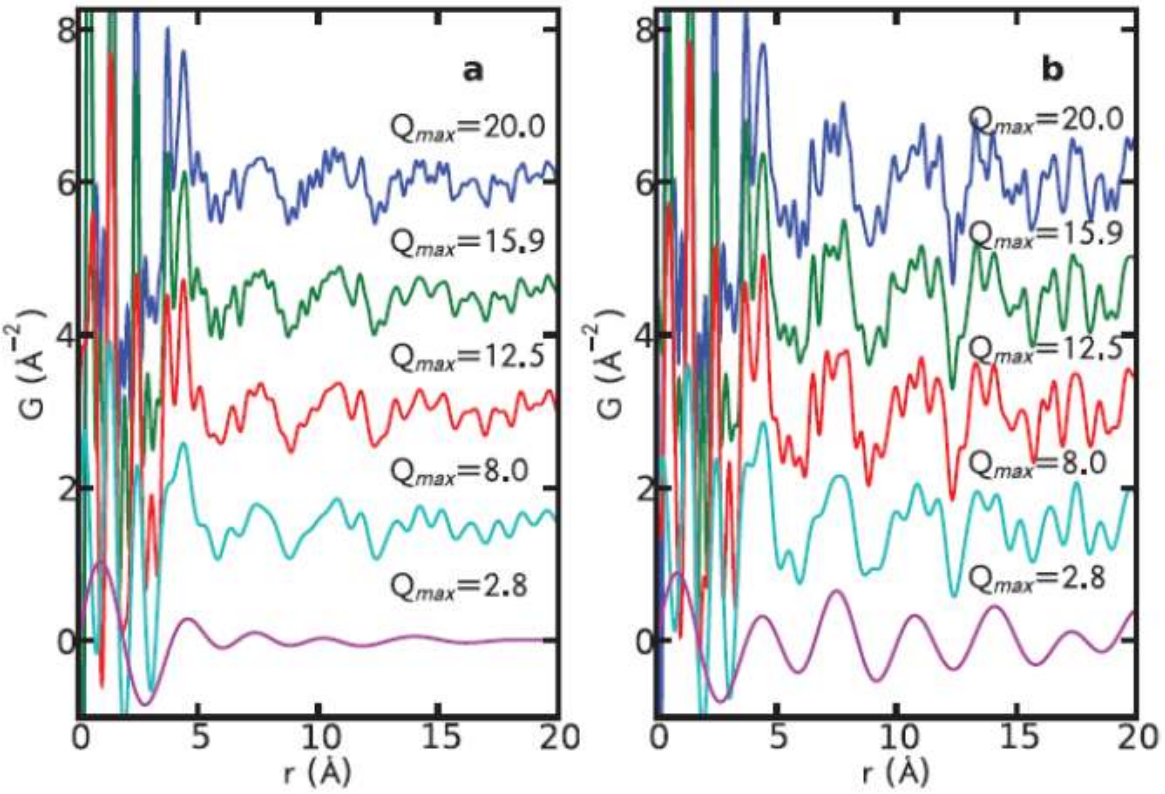

Figure 6.9 TS-PDF data of (a) melt-quenched CBZ and (b) crystalline CBZ form III, corresponding to (top – bottom) beamline ID-11-B data, Ag anode laboratory data, Mo anode laboratory data, Cu anode laboratory data (160o 2θ) and Cu anode laboratory data (40o 2θ).

It is clear from the above figure that a Qmax of 12.5A-1 which can be achieved in the laboratory by using a diffractometer equipped with a Mo anode, is sufficient to obtain all of the features that distinguish the local packing of a material (i.e. in the region above r = 3 A). Although the general shape of the TS-PDF is reproduced in the Qmax = 8.0 dataset, some important information is lost. This suggests that for differentiating the local packing in an X-ray amorphous API, laboratory total scattering data collected using a Mo anode should be

adequate. For the low Qmax Cu anode data, it is clear that there is significant loss of information, and that this dataset is clearly inadequate for fingerprinting an X-ray amorphous material. As would be expected, the TS-PDF data collected in the laboratory using a Cu anode did not give reliable correlation coefficients in polySNAP. However, data collected using all of the other radiation sources did indeed give good correlation coefficients.

6.4 Summary

The characterisation of X-ray amorphous pharmaceuticals is a significant challenege. However, if the correct approach is used, it is possible to compare the local packing of X-ray amorphous pharmaceuticals with that of known crystalline polymorphs of the compound. The ability to fingerprint amorphous pharmaceuticals using a TS-PDF approach in an analogous manner to which conventional XRPD is used to fingerprint crystalline forms of pharmaceuticals opens the door to future studies exploring the effects of processing or storage on X-ray amorphous pharmaceutical materials. There may also be sufficient information in the TS-PDF data to allow the fitting of a well-defined structural model to determine the molecular conformation and packing arrangement of an X-ray amorphous sample. This would clearly have been beneficial in the case of melt-quenched IND, where the local packing in a melt-quenched sample was distinct from that found in either the α or γ forms of IND, but the development of such models is beyond the scope of the current work. The results presented in this thesis chapter offers the potential to revolutionise the study of X-ray amorphous materials, by giving an insight into the basic science underpinning the structure of non-crystalline molecular materials to add to the plethora of thermodynamic and spectroscopic information that is already available. Also, by tracking the evolution of structure of melt-quenched materials, it may be possible to discover new polymorphs, *via* an amorphous or nanocrystalline route.

Chapter 7

Conclusions and Further work

7.1 Conclusions

The main conclusions that can be drawn from the experimental work presented in this thesis are outlined in the following sections.

7.1.1 Crystal structures of pharmaceutically acceptable carbamazepine co-crystals solved from synchrotron and laboratory X-ray powder diffraction data.

The high resolution powder diffraction beamline (beamline ID11) at Diamond Light Source is a very powerful tool for SDPD attempts using a simulated annealing approach. The beamline was newly commissioned at the time of the experiments carried out as part of the work described in this thesis, and the CBZ co-crystals were indeed the first totally organic, and certainly the first pharmaceutically relevant samples to be examined. It was found that the data quality available from beamline ID11 was excellent, as shown by the excellent indexing figures of merit for datasets collected on the beamline. The traditional caveat of radiation damage was observed in one sample examined on the beamline, but this is not too surprising, as organic materials with only weakly scattering atoms can be prone to radiation damage. Beamline ID11 data allowed for the rapid and accurate solution of two CBZ cocrystal structures from powder diffraction data; CBZ: HNA and CBZ: CAM. However, it was also possible to solve the crystal structures of two other co-crystals, CBZ: BEN and CBZ:SAL from laboratory XRPD data, albeit with less precisely determined unit cell parameters than the CBZ co-crystals solved from beamline ID11 data. Whilst work was on-going to prepare the CBZ co-crystal structures solved from powder diffraction data for publication, single crystal structures of the co-crystals were published. However, as has been shown by the work described in this thesis, the crystal structures of these materials were solved and refined quickly and accurately from powder diffraction data (and were found to be in excellent agreement with the single crystal structures). It is clear that beamline ID11 is a

useful tool for structure solution from powder diffraction data, but it is also perfectly feasible to solve crystal structures of pharmaceutical co-crystals from laboratory powder diffraction data.

7.1.2 Crystal structures of organic salbutamol salts from laboratory X-ray powder diffraction data.

Traditional salt screening involves allowing the API and the salt former to react in a solvent, then analysing the resulting solids using XRPD, DSC and other physicochemical techniques. There is, however, no guarantee that solid will precipitate from a given system within an acceptable timeframe if this approach is used. If no solid is produced, one option is to use an antisolvent to precipitate the salt. Another approach is to prepare the salt by grinding the reactants to form the desired salt. This grinding approach was used to prepare four pharmaceutically acceptable salts of salbutamol; salbutamol acetate, salbutamol butyrate, salbutamol formate and salbutamol saccharinate. Another two salts of salbutamol (salbutamol nicotinate and salbutamol xinafoate) were prepared by the more traditional solution based approach, with salbutamol xinafoate forming single crystals suitable for single crystal diffraction experiments. All of the other salts were available only as polycrystalline powders. All of the salbutamol salts were sharply indexing, although salbutamol saccharinate was initially amorphous and had to be crystallised by storing at high humidity, and could readily be indexed.

A salbutamol cation input Z-matrix for simulated annealing was readily prepared by manually protonating the crystal structure of salbutamol base, then correcting the structure to account for ionisiation. All of the anions formed salts for which crystal structures were available from the CSD, so input Z-matrices were readily prepared for the anions, with no correction necessary other than renumbering of the atoms in the anion. The crystal structures

of each of the salts were solved and refined relatively easily from laboratory X-ray powder diffraction data, and the accuracy of the structures was confirmed by performing CASTEP calculations to show that only the positions of hydrogen atoms could be optimised, as is normal due to the inherent difficulty in locating hydrogen atoms from X-ray (or even synchrotron) diffraction data. The results presented in chapter 5 of this thesis show that careful selection of input models for structure solution and rigid body Rietveld refinement of the solved structure can produce high quality crystal structures from laboratory X-ray powder diffraction data.

7.1.3 Characterisation of X-ray amorphous pharmaceuticals using a Total Scattering Pair Distribution Function (TS-PDF) approach.

In the literature, there is a plethora of papers reporting thermal and spectroscopic analyses of X-ray amorphous pharmaceutical compounds, but there are very few papers which describe the local packing of molecules in such a solid. When the crystal lattice is disrupted by some process, such as milling or melt-quenching, the long range order characteristic of crystalline compounds is lost. Consequently, no Bragg diffraction is visible, and only an X-ray amorphous 'halo' is typically observed. However, as has been shown in this thesis, it is possible to use TS-PDF data to probe the local structure in X-ray amorphous pharmaceuticals, and it was shown using this approach that melt-quenched "amorphous" CBZ is actually nanocrystalline CBZ form III. It was also found that melt-quenched IND is also nanocrystalline rather than truly amorphous, but the TS-PDF data showed that melt-quenched IND has local packing which is distinct to that found in the crystal structures of α or γ IND. The fact that it is possible to fingerprint the local packing in an X-ray amorphous sample in the laboratory is a major advantage, as this opens the door to more detailed studies of amorphous pharmaceuticals. For example, changes in local structure of an amorphous drug

as a function of humidity or temperature could readily be studied, which may help understand the processes involved in plasticisation and structural relaxation, which may in turn lead to the development of more stable X-ray amorphous dosage forms of APIs.

7.2 Further work

7.2.1 Crystal structures of pharmaceutically acceptable carbamazepine co-crystals solved from synchrotron and laboratory X-ray powder diffraction data.

The CBZ co-crystals examined during this work were, with the exception of the CBZ: CAM co-crystal, at the mid-point of structural complexity that is known to solve 'routinely' using DASH. It would be interesting to systematically increase the complexity by virtue of increased internal degrees of freedom in the co-crystal former. This could readily be achieved by choosing flexible, long chain fatty acids, such as stearic acid (Figure 7.1) as the co-crystal formers.

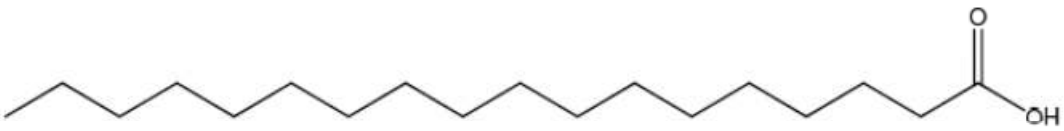

Figure 7.1 Molecular structure of stearic acid $C_{18}H_{36}O_2$

The CBZ co-crystals were all 1:1 stoichiometry, but as is the case with (+)-camphoric acid (CAM) some carboxylic acids contain two (or more) carboxyl groups, which raises the possibility of changing the co-crystal stoichiometry and therefore the complexity of the crystal structure. For example, if azelaic acid (AZL, Figure 7.2) was used as a co-crystal former, it could be possible to prepare 1:1, 1:2 and 2:1 co-crystals of CBZ: AZL. Table 7.1 lists the degrees of freedom associated with each of the potential CBZ: AZL co-crystal compositions.

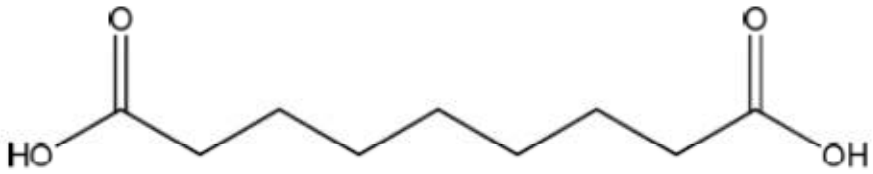

Figure 7.2 Molecular structure of azelaic acid $C_9H_{16}O_4$

Table 7.1 Degrees of freedom for potential CBZ: AZL co-crystals as a representative example of how the complexity of the system under study can be increased systematically by changing the stoichiometry of the co-crystal. The DOF values quoted in the table assume that the co-crystal crystallises as Z' = 1.

CBZ: AZL co-crystal stoichiometry	external DOF	internal DOF	total DOF
1 CBZ: 1 AZL	12	9	21
2 CBZ: 1 AZL	18	10	28
1 CBZ: 2 AZL	18	17	35

Increasing the complexity of the system in this manner by preparing new co-crystals then collecting data in the laboratory and on beamline ID11 would give a better insight as to whether the higher quality data available from the synchrotron played a key role in structure solution of such highly complex systems by simulated annealing in DASH.

7.2.2 Crystal structures of organic salbutamol salts from laboratory X-ray powder diffraction data.

As was mentioned in chapter 5 of this thesis, it is possible to prepare fatty acid salts of salbutamol, which may be useful as drugs for treatment of an asthma attack which has already begun. However, apart from the crystal structures of the six salts discussed in chapter 5, no crystal structures for organic salts of salbutamol have been reported. During the course of the work discussed in this thesis, it was possible to prepare samples of salbutamol caprate,

salbutamol laurate and salbutamol stearate according to a published method (Penkler *et al.*, 1999). These fatty acid salts of salbutamol are sharply diffracting, and could readily be indexed from laboratory XRPD data. Table 7.2 shows the unit cell parameters of the fatty acid salbutamol salts.

Table 7.2 Unit cell parameters for salbutamol fatty acid salts. Indexing was performed using TOPAS 4.

salbutamol salt	a (Å)	b(Å)	c (Å)	α°	β°	γ°	space group	total DOF
caprate	10.258	10.744	11.537	84.705	74.969	88.257	$P\bar{1}$	25
laurate	10.293	10.67	24.489	89.87	82.57	90.034	$P\bar{1}$	54
stearate	10.644	10.259	15.338	76.303	92.287	88.506	$P\bar{1}$	33

Attempts to solve the crystal structures of these salts from laboratory XRPD data were unsuccessful. The failure to successfully solve the crystal structures is probably due to the complexity of the systems, rather than poor data quality, as each of the salts was convincingly indexed. In order to solve the crystal structure of these salts, it seems that more attention to the simulated annealing protocol is required. Carrying out a series of experiments where the cooling rate, starting temperature, number of moves per run and random seeds of the simulated annealing runs is varied may be useful in structure solution attempts. Also, the application of 'chemical sense' could be considered. For example, the long alkyl chains in the fatty acid molecules confer considerable flexibility, and if this flexibility could somehow be constrained, in such a way that conserves chemical sense, but effectively removes some degrees of freedom from the simulated annealing runs, then the chances of structure solution may be increased. The application of chemically sensible constraints to the alkyl chains of the acid anions was briefly evaluated, but a more systematic approach is needed in order to successfully solve the crystal structures of these salts. Another possibility would be to collect synchrotron data from samples of the fatty acid salbutamol salts, in the hope that the increased resolution in the data could be exploited to enable structure solution. Synchrotron

data could also be collected from a sample of salbutamol butyrate, as better data may make it possible to accurately refine the disorder in the crystal structure of this material.

7.2.3 Characterisation of X-ray amorphous pharmaceuticals using a Total Scattering Pair Distribution Function (TS-PDF) approach.

Given the fact that melt-quenched IND has local packing that is distinct from both the α and γ polymorphs of IND, a logical next step would be to focus on preparing a pure phase sample of δ-IND which can be prepared by recrystallisation from the melt. If a sample of δ-IND is successfully prepared, the next step would be to attempt structure solution from powder diffraction data and collect TS-PDF data, either in the laboratory using a molybdenum anode instrument or at a synchrotron. This would allow direct comparison of the local packing of melt-quenched IND with that of δ-IND. Another possible set of experiments could be to prepare an amorphous API using different amorphisation route (e.g. melt-quenching and milling), then stress test the material at different temperatures and relative humidities. The changes in local packing could then be monitored up to the crystallisation point. Such experiments may give an insight to the stability of amorphous APIs prepared by different routes. Finally, the TS-PDF method could be applied to simple ASDs in order to assess the local interactions between the API and the polymer. Such information may yield valuable structural information for such systems that could be useful in rationalising the physical stability of ASDs.

References

Allen, F. H. (2002). *Acta Crystallographica Section B-Structural Science* **58**, 380-388.

Altomare, A., Campi, G., Cuocci, C., Eriksson, L., Giacovazzo, C., Moliterni, A., Rizzi, R. & Werner, P. E. (2009). *Journal of Applied Crystallography* **42**, 768-775.

Altomare, A., Cuocci, C., Giacovazzo, C., Guagliardi, A., Moliterni, A. G. G. & Rizzi, R. (2002). *Journal of Applied Crystallography* **35**, 182-184.

Altomare, A., Cuocci, C., Giacovazzo, C., Moliterni, A. & Rizzi, R. (2008). *Journal of Applied Crystallography* **41**, 592-599.

Ambike, A. A., Mahadik, K. R. & Paradkar, A. (2005). *Pharmaceutical Research* **22**, 990-998.

Amidon, G. L., Lennernas, H., Shah, V. P. & Crison, J. R. (1995). *Pharmaceutical Research* **12**, 413-420.

Andronis, V. & Zografi, G. (2000). *Journal of Non-Crystalline Solids* **271**, 236-248.

Arlin, J.-B., Price, L. S., Price, S. L. & Florence, A. J. (2011). *Chemical Communications* **47**, 7074-7076.

Bak, A., Gore, A., Yanez, E., Stanton, M., Tufekcic, S., Syed, R., Akrami, A., Rose, M., Surapaneni, S., Bostick, T., King, A., Neervannan, S., Ostovic, D. & Koparkar, A. (2008). *Journal of Pharmaceutical Sciences* **97**, 3942-3956.

Banerjee, R., Bhatt, P. M., Ravindra, N. V. & Desiraju, G. R. (2005). *Crystal Growth & Design* **5**, 2299-2309.

Bansal, S. S., Kaushal, A. M. & Bansal, A. K. (2007). *Molecular Pharmaceutics* **4**, 794-802.

Basavoju, S., Bostrom, D. & Velaga, S. P. (2008). *Pharmaceutical Research* **25**, 530-541.

Bates, S., Kelly, R. C., Ivanisevic, I., Schields, P., Zografi, G. & Newman, A. W. (2007). *Journal of Pharmaceutical Sciences* **96**, 1418-1433.

Bates, S., Zografi, G., Engers, D., Morris, K., Crowley, K. & Newman, A. (2006). *Pharmaceutical Research* **23**, 2333-2349.

Beale, J. P. & Grainger, C. T. (1972). *Cryst.Struct.Commun.* **1**, 73.

Beukes, J. A., Mo, F. & van Beek, W. (2007). *Physical Chemistry Chemical Physics* **9**, 4709-4720.

Bhugra, C., Shmeis, R., Krill, S. L. & Pikal, M. J. (2008). *Journal of Pharmaceutical Sciences* **97**, 4498-4515.

Billinge, S. J. L. (2008). *Journal of Solid State Chemistry* **181**, 1695-1700.

Billinge, S. J. L., Dykhne, T., Juhas, P., Bozin, E., Taylor, R., Florence, A. J. & Shankland, K. (2010). *Crystengcomm* **12**, 1366-1368.

Billinge, S. J. L., McKimmy, E. J., Shatnawi, M., Kim, H. J., Petkov, V., Wermeille, D. & Pinnavaia, T. J. (2005). *Journal of the American Chemical Society* **127**, 8492-8498.

Blagden, N., de Matas, M., Gavan, P. T. & York, P. (2007). *Advanced Drug Delivery Reviews* **59**, 617-630.

Boultif, A. & Louer, D. (1991). *Journal of Applied Crystallography* **24**, 987-993.

Brandao-Neto, J., Thompson, S. P., Lennie, A. R., Ferreria, F. F. & Tang, C. C. (2010). *Journal of synchrotron radiation* **17**, 53-60.

Brown, A. B., York, P., Shields, L., Doherty, C. & Frampton, C. (1994). *Pharmaceutical Research (New York)* **11**, S151.

Brown, A. B., York, P., Williams, A. C., Edwards, H. G. M. & Worthington, H. (1993). *Journal of Pharmacy and Pharmacology* **45**, 1135.

Bruno, I. J., Cole, J. C., Edgington, P. R., Kessler, M., Macrae, C. F., McCabe, P., Pearson, J. & Taylor, R. (2002). *Acta Crystallographica Section B-Structural Science* **58**, 389-397.

Bruno, I. J., Cole, J. C., Kessler, M., Luo, J., Motherwell, W. D. S., Purkis, L. H., Smith, B. R., Taylor, R., Cooper, R. I., Harris, S. E. & Orpen, A. G. (2004). *Journal of Chemical Information and Computer Sciences* **44**, 2133-2144.

Bucci, R., Magrí, A. D. & A.L, M. (1998). *Fresenius J Anal Chem* **326**, 577-582.

Caira, M. R., Dodds, D. R. & Nassimbeni, L. R. (2002). *Journal of Thermal Analysis and Calorimetry* **68**, 647-655.

Carino, S. R., Sperry, D. C. & Hawley, M. (2006). *Journal of Pharmaceutical Sciences* **95**, 116-125.

Carpentier, L., Decressain, R., Desprez, S. & Descamps, M. (2006). *Journal of Physical Chemistry B* **110**, 457-464.

Childs, S. L., Rodriguez-Hornedo, N., Reddy, L. S., Jayasankar, A., Maheshwari, C., McCausland, L., Shipplett, R. & Stahly, B. C. (2008). *Crystengcomm* **10**, 856-864.

Childs, S. L., Wood, P. A., Rodriguez-Hornedo, N., Reddy, L. S. & Hardcastle, K. I. (2009). *Crystal Growth & Design* **9**, 1869-1888.

Clark, S. J., Segall, M. D., Pickard, C. J., Hasnip, P. J., Probert, M. J., Refson, K. & Payne, M. C. (2005). *Zeitschrift Fur Kristallographie* **220**, 567-570.

Coelho, A. A. (2000). *Journal of Applied Crystallography* **33**, 899-908.

Coelho, A. A. (2003). *Journal of Applied Crystallography* **36**, 86-95.

Crowley, K. J. & Zografi, G. (2002). *Journal of Pharmaceutical Sciences* **91**, 492-507.

David, S. E., Ramirez, M., Timmins, P. & Conway, B. R. (2010). *Journal of Pharmacy and Pharmacology* **62**, 1519-1525.

David, W. I. F., Shankland, K., Mc Cusker, L. B. & Baerlocher, C. (2002). *Structure Determination from Powder Diffraction Data*.

David, W. I. F., Shankland, K. & Shankland, N. (1998). *Chemical Communications*, 931-932.

David, W. I. F., Shankland, K., van de Streek, J., Pidcock, E., Motherwell, W. D. S. & Cole, J. C. (2006). *Journal of Applied Crystallography* **39**, 910-915.

Derollez, P., Dudognon, E., Affouard, F., Danede, F., Correia, N. T. & Descamps, M. (2010). *Acta Crystallographica Section B-Structural Science* **66**, 76-80.

DiNunzio, J. C., Miller, D. A., Yang, W., McGinity, J. W. & Williams, R. O. (2008). *Molecular Pharmaceutics* **5**, 968-980.

Dollase, W. A. (1986). *Journal of Applied Crystallography* **19**, 267-272.

Dykhne, T., Taylor, R., Florence, A. & Billinge, S. J. L. (2011). *Pharmaceutical Research* **28**, 1041-1048

Eixarch, H., Haltner-Ukomadu, E., Beisswenger, C. & Bock, U. (2010). *Journal of Epithelial Biology and Pharmacology* **3**, 1-14.

Elder, D. P., Delaney, E., Teasdale, A., Eyley, S., Reif, V. D., Jacq, K., Facchine, K. L., Oestrich, R. S., Sandra, P. & David, F. (2010). *Journal of Pharmaceutical Sciences* **99**, 2948-2961.

Etter, M. C., Macdonald, J. C. & Bernstein, J. (1990). *Acta Crystallographica Section B-Structural Science* **46**, 256-262.

Fernandes, P., Shankland, K., Florence, A. J., Shankland, N. & Johnston, A. (2007). *Journal of Pharmaceutical Sciences* **96**, 1192-1202.

Fernandez-Bertran, J., Alvarez, J. C. & Reguera, E. (1998). *Solid State Ionics* **106**, 129-135.

Feth, M. P., Volz, J., Hess, U., Sturm, E. & Hummel, R. P. (2008). *Journal of Pharmaceutical Sciences* **97**, 3765-3780.

Fini, A., Cavallari, C. & Ospitali, F. (2008). *European Journal of Pharmaceutics and Biopharmaceutics* **70**, 409-420.

Fleischman, S. G., Kuduva, S. S., McMahon, J. A., Moulton, B., Walsh, R. D. B., Rodriguez-Hornedo, N. & Zaworotko, M. J. (2003). *Crystal Growth & Design* **3**, 909-919.

Florence, A. J., Bardin, J., Johnston, B., Shankland, N., Griffin, T. A. N. & Shankland, K. (2009). *Zeitschrift Fur Kristallographie*, 215-220.

Florence, A. J., Shankland, N., Shankland, K., David, W. I. F., Pidcock, E., Xu, X. L., Johnston, A., Kennedy, A. R., Cox, P. J., Evans, J. S. O., Steele, G., Cosgrove, S. D. & Frampton, C. S. (2005). *Journal of Applied Crystallography* **38**, 249-259.

Fudala, P. J. & Johnson, R. E. (2006). *Drug and Alcohol Dependence* **83**, S40-S47.

Fujii, K., Young, M. T. & Harris, K. D. M. (2011). *Journal of Structural Biology* **174**, 461-467.

Glusker, J. P., Lewis, M. & Rossi, M. (1994). *Crystal Structure Analysis for Chemists and Biologists*. New York.

Goldring, D., Botoshansky, M., Khalfin, R. L., Pertsikov, B., Nisnevitch, G., Ponomarev, V., Zaltzman, I., Gutman, A. & Kaftory, M. (2004). *Acta Crystallographica Section C-Crystal Structure Communications* **60**, O843-O846.

Gowthamarajan, K., Kulkarni, G. T. & Kumar, N. N. (2004). *Resonance* **9**, 25-32.

Griffin, T. A. N., Shankland, K., van de Streek, J. V. & Cole, J. (2009a). *Journal of Applied Crystallography* **42**, 356-359.

Griffin, T. A. N., Shankland, K., van de Streek, J. V. & Cole, J. (2009b). *Journal of Applied Crystallography* **42**, 360-361.

Hancock, B. C. & Parks, M. (2000). *Pharmaceutical Research* **17**, 397-404.

Harris, H., Shur, J., Clarke, J., French, E. & R, P. ***Rapid Pre-formulation Screening of Drug Salts for Dry Powder Inhalers,*** ddl-conference.org.uk/files/sessions/11.4P.**Harris**.pdf.

Harris, K. D. M., Johnston, R. L. & Kariuki, B. M. (1998). *Acta Crystallographica Section A* **54**, 632-645.

Haynes, D. A., Jones, W. & Motherwell, W. D. S. (2005). *Journal of Pharmaceutical Sciences* **94**, 2111-2120.

Hedoux, A., Guinet, Y., Capet, F., Paccou, L. & Descamps, M. (2008). *Physical Review B* **77**, 10.

Hickey, M. B., Peterson, M. L., Scoppettuolo, L. A., Morrisette, S. L., Vetter, A., Guzman, H., Remenar, J. F., Zhang, Z., Tawa, M. D., Haley, S., Zaworotko, M. J. & Almarsson, O. (2007). *European Journal of Pharmaceutics and Biopharmaceutics* **67**, 112-119.

Imboden, R. & Imanidis, G. (1999). *European Journal of Pharmaceutics and Biopharmaceutics* **47**, 161-167.

Immirzi, A., Erra, L. & Tedesco, C. (2009). *Journal of Applied Crystallography* **42**, 810-814.

Johnston, J. C., David, W. I. F., Markvardsen, A. J. & Shankland, K. (2002). *Acta Crystallographica Section A* **58**, 441-447.

Kaduk, J. A. (2007). *Powder Diffraction* **22**, 74-82.

Kasim, N. A., Whitehouse, M., Ramachandran, C., Bermejo, M., Lennernas, H., Hussain, A. S., Junginger, H. E., Stavchansky, S. A., Midha, K. K., Shah, V. P. & Amidon, G. L. (2004). *Molecular Pharmaceutics* **1**, 85-96.

Kaushal, A. M., Chakraborti, A. K. & Bansal, A. K. (2008). *Molecular Pharmaceutics* **5**, 937-945.

Kellici, S., Gong, K. A., Lin, T. A., Brown, S., Clark, R. J. H., Vickers, M., Cockcroft, J. K., Middelkoop, V., Barnes, P., Perkins, J. M., Tighe, C. J. & Darr, J. A. (2010). *Philosophical Transactions of the Royal Society a-Mathematical Physical and Engineering Sciences* **368**, 4331-4349.

Kennedy, M., Hu, J., Gao, P., Li, L., Ali-Reynolds, A., Chal, B., Gupta, V., Ma, C., Mahajan, N., Akrami, A. & Surapaneni, S. (2008). *Molecular Pharmaceutics* **5**, 981-993.

Lalkshman, J. P., Cao, Y., Kowalski, J. & Serajuddin, A. T. M. (2008). *Molecular Pharmaceutics* **5**, 994-1002.

Lang, M. D., Kampf, J. W. & Matzger, A. J. (2002). *Journal of Pharmaceutical Sciences* **91**, 1186-1190.

Lightfoot, P., Mehta, M. A. & Bruce, P. G. (1993). *Science* **262**, 883-885.

Lindenmayer, J. (2010). *Neuropsychiatr Dis Treat* **6**, 261-267.

Lipinski, C. A., Lombardo, F., Dominy, B. W. & Feeney, P. J. (2001). *Advanced Drug Delivery Reviews* **46**, 3-26.

Louer, D. & Boultif, A. (2007). *Zeitschrift Fur Kristallographie*, 191-196.

Maccaroni, E., Malpezzi, L., Panzeri, W. & Masciocchi, N. (2010). *Journal of Pharmaceutical and Biomedical Analysis* **53**, 1-6.

Margiolaki, I. & Wright, J. P. (2008). *Acta Crystallographica Section A* **64**, 169-180.

Margiolaki, I., Wright, J. P., Wilmanns, M., Fitch, A. N. & Pinotsis, N. (2007). *Journal of the American Chemical Society* **129**, 11865-11871.

Markvardsen, A. J., David, W. I. F., Johnson, J. C. & Shankland, K. (2001). *Acta Crystallographica Section A* **57**, 47-54.

Markvardsen, A. J., Shankland, K., David, W. I. F. & Didlick, G. (2005). *Journal of Applied Crystallography* **38**, 107-111.

McNamara, D. P., Childs, S. L., Giordano, J., Iarriccio, A., Cassidy, J., Shet, M. S., Mannion, R., O'Donnell, E. & Park, A. (2006). *Pharmaceutical Research* **23**, 1888-1897.

Mowat, J. P. S., Groves, J. A., Wharmby, M. T., Miller, S. R., Li, Y., Lightfoot, P. & Wright, P. A. (2009). *Journal of Solid State Chemistry* **182**, 2769-2778.

Neumann, M. A. (2002). *J. Appl. Cryst.* **36**.

Newman, A., Engers, D., Bates, S., Ivanisevic, I., Kelly, R. C. & Zografi, G. (2008). *Journal of Pharmaceutical Sciences* **97**, 4840-4856.

P., H. S. & Wermuth, C. G. (2002). *Handbook of Pharmaceutical Salts Properties, Selection and Use*, edited by H. S. P. & C. G. Wermuth.

Patel, R. & Patel, M. (2008). *Journal of Dispersion Science and Technology* **29**, 193-204.

Patterson, J. E., James, M. B., Forster, A. H., Lancaster, R. W., Butler, J. M. & Rades, T. (2005). *Journal of Pharmaceutical Sciences* **94**, 1998-2012.

Pawley, G. S. (1981). *Journal of Applied Crystallography* **14**, 357-361.

Penkler, L. J., DeKock, L.-A. & Whittaker, D. V. (1999). Farmac Nederland BV

Peschar, R., Pop, M. M., De Ridder, D. J. A., van Mechelen, J. B., Driessen, R. A. J. & Schenk, H. (2004). *Journal of Physical Chemistry B* **108**, 15450-15453.

Petkov, V., Billinge, S. J. L., Heising, J. & Kanatzidis, M. G. (2000). *Journal of the American Chemical Society* **122**, 11571-11576.

Reddy, L. S., Bethune, S. J., Kampf, J. W. & Rodriguez-Hornedo, N. (2009). *Crystal Growth & Design* **9**, 378-385.

Rietveld, H. M. (1969). *J. Appl. Cryst* **2**.

Sauolainen, M., Heinz, A., Strachan, C., Gordon, K. C., Yliruusi, J., Rades, T. & Sandler, N. (2007). *European Journal of Pharmaceutical Sciences* **30**, 113-123.

Savolainen, M., Kogermann, K., Heinz, A., Aaltonen, J., Peltonen, L., Strachan, C. & Yliruusi, J. (2009). *European Journal of Pharmaceutics and Biopharmaceutics* **71**, 71-79.

Seijas, L. E., Mora, A. J., Delgado, G. E., Lopez-Carrasquero, F., Baez, M. E., Brunelli, M. & Fitch, A. N. (2009). *Acta Crystallographica Section B-Structural Science* **65**, 724-730.

Serajuddin, A. T. M. (2007). *Advanced Drug Delivery Reviews* **59**, 603-616.

Shah, K. P. & Chafetz, L. (1994). *International Journal of Pharmaceutics* **109**, 271-281.

Shankland, K., David, W. I. F. & Sivia, D. S. (1997). *Journal of Materials Chemistry* **7**, 569-572.

Shankland, K., McBride, L., David, W. I. F., Shankland, N. & Steele, G. (2002). *Journal of Applied Crystallography* **35**, 443-454.

Shatnawi, M., Paglia, G., Dye, J. L., Cram, K. C., Lefenfeld, M. & Billinge, S. J. L. (2007). *Journal of the American Chemical Society* **129**, 1386-1392.

Sheth, A. R., Young, V. G. & Grant, D. J. W. (2002). *Acta Crystallographica Section E-Structure Reports Online* **58**, m197-m199.

Singhal, D. & Curatolo, W. (2004). *Advanced Drug Delivery Reviews* **56**, 335-347.

Spek, A. L. (2003). *Journal of Applied Crystallography* **36**, 7-13.

Stewart, J. J. P. (1990). *Journal of Computer-Aided Molecular Design* **4**, 1-45.

Stylianou, K. C., Heck, R., Chong, S. Y., Bacsa, J., Jones, J. T. A., Khimyak, Y. Z., Bradshaw, D. & Rosseinsky, M. J. (2010). *Journal of the American Chemical Society* **132**, 4119-4130.

Taylor, L. S. & Zografi, G. (1997a). *Pharmaceutical Research* **14**, 1691-1698.

Taylor, L. S. & Zografi, G. (1997b). *Pharmaceutical Research (New York)* **14**, S186-S187.

Telang, C., Mujumdar, S. & Mathew, M. (2009). *Journal of Pharmaceutical Sciences* **98**, 2149-2159.

Thompson, S. P., Parker, J. E., Potter, J., Hill, T. P., Birt, A., Cobb, T. M., Yuan, F. & Tang, C. C. (2009). *Review of Scientific Instruments* **80**.

Tobyn, M., Brown, J., Dennis, A. B., Fakes, M., Gao, Q., Gamble, J., Khimyak, Y. Z., McGeorge, G., Patel, C., Sinclair, W., Timmins, P. & Yin, S. (2009). *Journal of Pharmaceutical Sciences* **98**, 3456-3468.

Towler, C. S., Li, T. L., Wikstrom, H., Remick, D. M., Sanchez-Felix, M. V. & Taylor, L. S. (2008). *Molecular Pharmaceutics* **5**, 946-955.

Trask, A. V., Haynes, D. A., Motherwell, W. D. S. & Jones, W. (2006). *Chemical Communications*, 51-53.

Trask, A. V., Motherwell, W. D. S. & Jones, W. (2004). *Chemical Communications*, 890-891.

van Mechelen, J. B., Peschar, R. & Schenk, H. (2008). *Acta Crystallographica Section B-Structural Science* **64**, 240-248.

Veerapandian, B., Salunke, D. M. & Vijayan, M. (1984). *Acta Crystallographica Section C-Crystal Structure Communications* **40**, 500-502.

Vishweshwar, P., McMahon, J. A., Peterson, M. L., Hickey, M. B., Shattock, T. R. & Zaworotko, M. J. (2005). *Chemical Communications*, 4601-4603.

Werner, P. E., Eriksson, L. & Westdahl, M. (1985). *Journal of Applied Crystallography* **18**, 367-370.

Wright, J. P., Besnard, C., Margiolaki, I., Basso, S., Camus, F., Fitch, A. N., Fox, G. C., Pattison, P. & Schiltz, M. (2008). *Journal of Applied Crystallography* **41**, 329-339.

Wu, T. & Yu, L. (2006). *Journal of Physical Chemistry B* **110**, 15694-15699.

Xu, L., Li, S. M. & Sunada, H. (2007). *Chemical & Pharmaceutical Bulletin* **55**, 1545-1550.

Zeitler, J. A., Taday, P. F., Pepper, M. & Rades, T. (2007). *Journal of Pharmaceutical Sciences* **96**, 2703-2709.

Zhou, D., Zhang, G. G. Z., Law, D., Grant, D. J. W. & Schmitt, E. A. (2008). *Molecular Pharmaceutics* **5**, 927-936.

Zupancic, V., Smrkolj, M., Benkic, P., Simonic, I., Plevnik, M., Ritlop, G., Kristl, A. & Vrecer, F. (2010). *Acta Chimica Slovenica* **57**, 376-385.

Appendix 1

Publications arising from this work

1. Articles published

Billinge, S. J. L., Dykhne, T., Juhas, P., Bozin, E., Taylor, R., Florence, A. J. & Shankland, K. (2010).

Characterisation of amorphous and nanocrystalline molecular materials by total scattering, *Crystengcomm* **12**, 1366-1368.

Abstract The use of high-energy X-ray total scattering coupled with pair distribution function analysis produces unique structural fingerprints from amorphous and nanostructured phases of the pharmaceuticals carbamazepine and indomethacin. The advantages of such facility based experiments over laboratory based ones are discussed and the technique is illustrated with the characterisation of a melt-quenched sample of carbamazepine as a nanocrystalline (4.5nm domain diameter) version of form III.

Dykhne, T., Taylor, R., Florence, A., & Billinge, S. J. L. (2011).

Data Requirements for the Reliable Use of Atomic Pair Distribution Functions in Amorphous Pharmaceutical Fingerprinting, *Pharm Res* **28**, 1041-1048.

Abstract The optimal measurement strategy for fingerprinting condensed phases of pharmaceutical systems using atomic pair distribution functions (PDFs) obtained using several different types of X-ray diffraction instruments was determined. PDFs of crystalline and amorphous phase molecular systems derived from data accessible to copper-, molybdenum- and silver-anode laboratory sources were compared to one another and synchrotron data using qualitative and quantitative methods. We find that reliable fingerprinting is still possible using silver and molybdenum laboratory sources, but data from copper anode laboratory sources are unreliable for fingerprinting, yielding ambiguous and potentially incorrect results. The ambiguities make data measured using low energy X-rays unsuitable for fingerprinting active pharmaceutical ingredients and small molecule systems,

and, in general, copper anode diffractometers are undesirable for this purpose; however, laboratory X-ray sources with either Mo or Ag anodes are well suited for this application.

Appendix 2

An example TOPAS rigid body ".inp" file

A

xdd "temp.xye" xye_format
.raw

Read in diffraction data. Can be or .xye format

B

r_exp 1.562
r_exp_dash 4.994
r_wp 4.176
r_wp_dash 13.351
r_p 3.876
r_p_dash 13.001
gof 2.673
weighted_Durbin_Watson 0.353

some commonly used GOF indicators. Typically r_wp is used as the main fit descriptor, but the other values also give useful diagnostic information on the fit The "_dash" keywords in the file refer to background subtracted parameters in the refinement. The gof refers to the fit of the structural model to the observed data

C

chi2_convergence_criteria 0.000001
'only_penalties
bkg @

Chi2_convergence_criteria is set to a low value to ensure the refinement does not terminate early. Only_penalties is used at earlier stages in the refinement when the co-ordinates of the rigid body are mapped to the real atomic coordinates in the crystal structure. In later steps this is commented out ('). Bkg refers to the background modelling routine. The number of parameters listed which is typically 10-15 for laboratory data determines the order of the Chebyshev polynomial to be applied

D

start_X 2.0000
finish_X 70.5495
Zero_Error(, 0.00852)
LP_Factor(26)
Rp 217.5
Rs 217.5

Start_X and finish_X determine the data range to be considered during the refinement. Zero_Error is the zeropoint error (in °2θ) due to errors in the instrument calibration. The LP_Factor(26) term makes sure that the Lorentz-polarisation correction is applied.
The value of 26 is the monochromator take off angle for the diffractometer in question
Rp and Rs are the primary and secondary radii, expressed in mm. These terms describe the diffractometer geometry

E

axial_conv
filament_length 9.47901121
sample_length 4.22049839
receiving_slit_length 8.89641639
axial_n_beta 20
axial_del 0.0053

This is a model for describing the peak asymmetry due to axial divergence of the X-ray beam. The arguments include the tube filament length (mm) sample length in the axial direction (mm) and the length of the detector/receiving slit "axial_n_beta" is the number of X-rays produced from a point source in the axial direction. "axial_del" defines the width of a fine focus tube (in °2θ) and is set at the value shown

F

lam
ymin_on_ymax 0.001
la 1 lo 1.540600
x_calculation_step 0.017112

This block describes the wavelength of radiation used. for monochromatic radiation la=1 and for CuKα_1 radiation λ= 1.54056 Å. The term ymin_on_ymax describes the emission profile and the extent to which the profile is calculated. 0.001 is the default value. The term x_calculation_step is the step size for calculations in °2θ

G

```
Str
CS_L( , 9999.99996_LIMIT_MIN_0.3)
CS_G( , 293.49218)
Strain_G( , 0.34534)
Strain_L( , 0.24787)
a       9.31514`
b       9.89233`
c       9.90068`
al      99.22876`
be      111.38470`
ga      104.83026`
space_group "P-1"
```

Str is a command that tells TOPAS that it is in Rietveld refinement mode. The terms CS_L and CS_G represent the Lorentzian and Gaussian contributions to crystallite size. Strain_G and Strain_L correspond to the Lorentzian and Gaussian contributions to crystallite strain. The unit cell parameters are refined earlier in the refinement process

H

```
  scale @  0.00273871693`
'    PO(@, 1.0, , 0 0 1)
macro ref_flag {   }
prm   bnonh  3.06312`
prm bh = 1.2 * bnonh;
```

A scale factor relating the observed and calculated data is required and should be refined. The PO term allows the inclusion of a preferred orientation correction if required. Macro ref_flag is a command that can be used to allow the atomic coordinates to refine. The term prm bnonh refers to the non-hydrogen ITF prm bh describes the H atom ITF which is taken as 1.2*bnonh which is essentially the riding atom model in single crystal refinement

I

site O4Z x ref_flag 0.99151 y ref_flag 0.05778 z ref_flag 0.21541 occ O 1 beq = bnonh;

each atom in the asymmetric unit is represented by a label the Z suffix shows that the atom is part of the rigid body description. Unlike in a restrained Rietveld refinement, the fractional coordinates are not refined during rigid body Rietveld refinement. "occ O 1" shows that the site is fully occupied by an oxygen atom.
"beq = bnonh" shows that the atom has an isotropic temperature factor (ITF) of 3.06312

J

rotate @ -63.11140` qa 1
rotate @ 108.16769` qb 1
rotate @ -96.94797` qc 1
translate ta @ 0.05976`
translate tb @ 0.24937`

translate tc @ 0.62682`

These describe the position and orientation of the rigid bodies against the diffraction data

K

z_matrix C1Z N1Z 1.4961217 C5Z 115.897331 C6Z @ -160.058190

The above section shows the major differences between rigid body Rietveld and restrained Rietveld refinement. In a restrained Rietveld refinement, the bond lengths and angles are allowed to vary within a narrow range. For example if we consider an aromatic ring, the C-C bond length can be restrained to a value of 1.39Å. In a restrained refinement, the bond length can fluctuate slightly, so the bond length may change to say, 1.38Å. Similarly, the C-C-C bond angle can be restrained to a value of 120°, but may fluctuate to ca. 119.9° after refinement. In a rigid body refinement, the bond lengths and angles do not vary during the

refinement thus the chemical knowledge input during the z-matrix construction is retained. Only the values of any flexible torsions are refined as indicated above by the '@' sign are allowed to vary, consequently, the structural parameters being refined are significantly reduced.

Appendix 3

DSC data for CBZ co-crystals

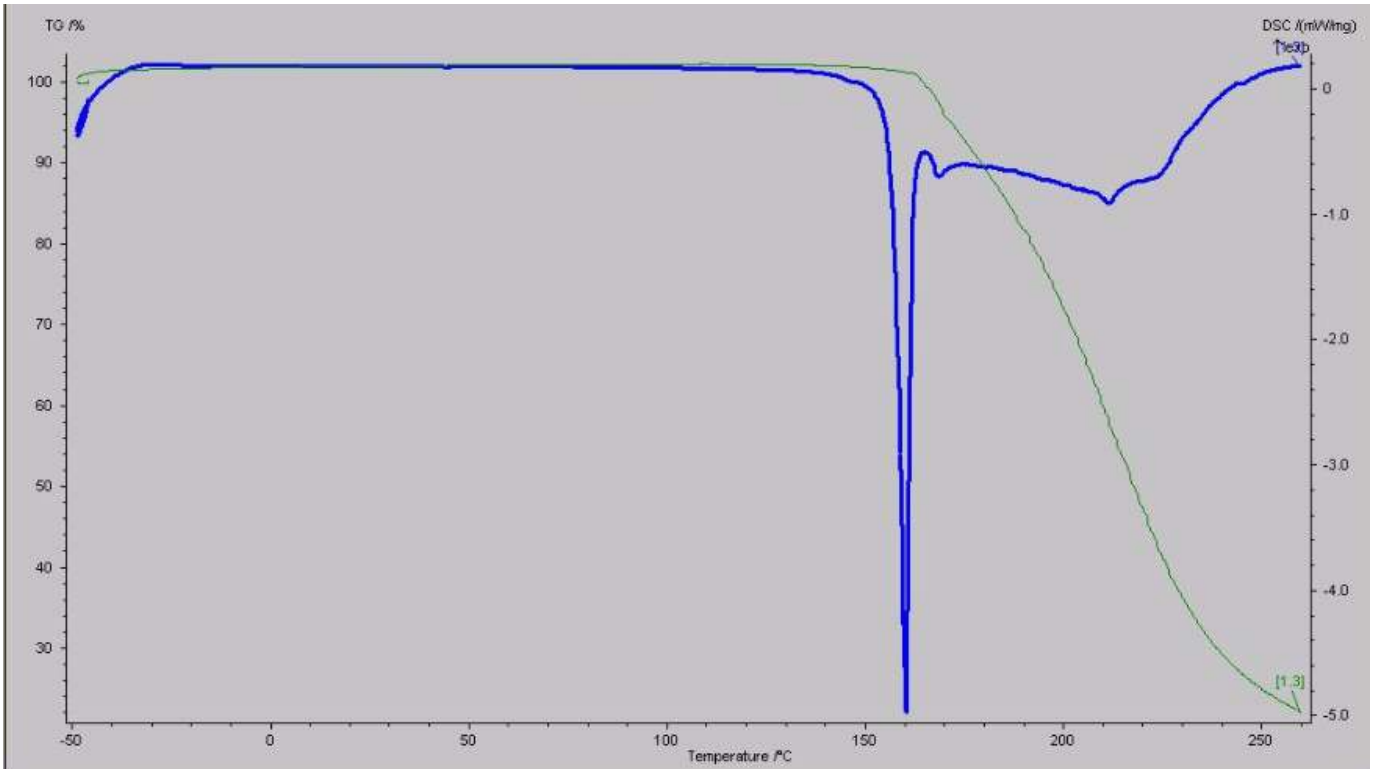

DSC trace of a sample of CBZ:SAL co-crystal in the range -50 - 250°C

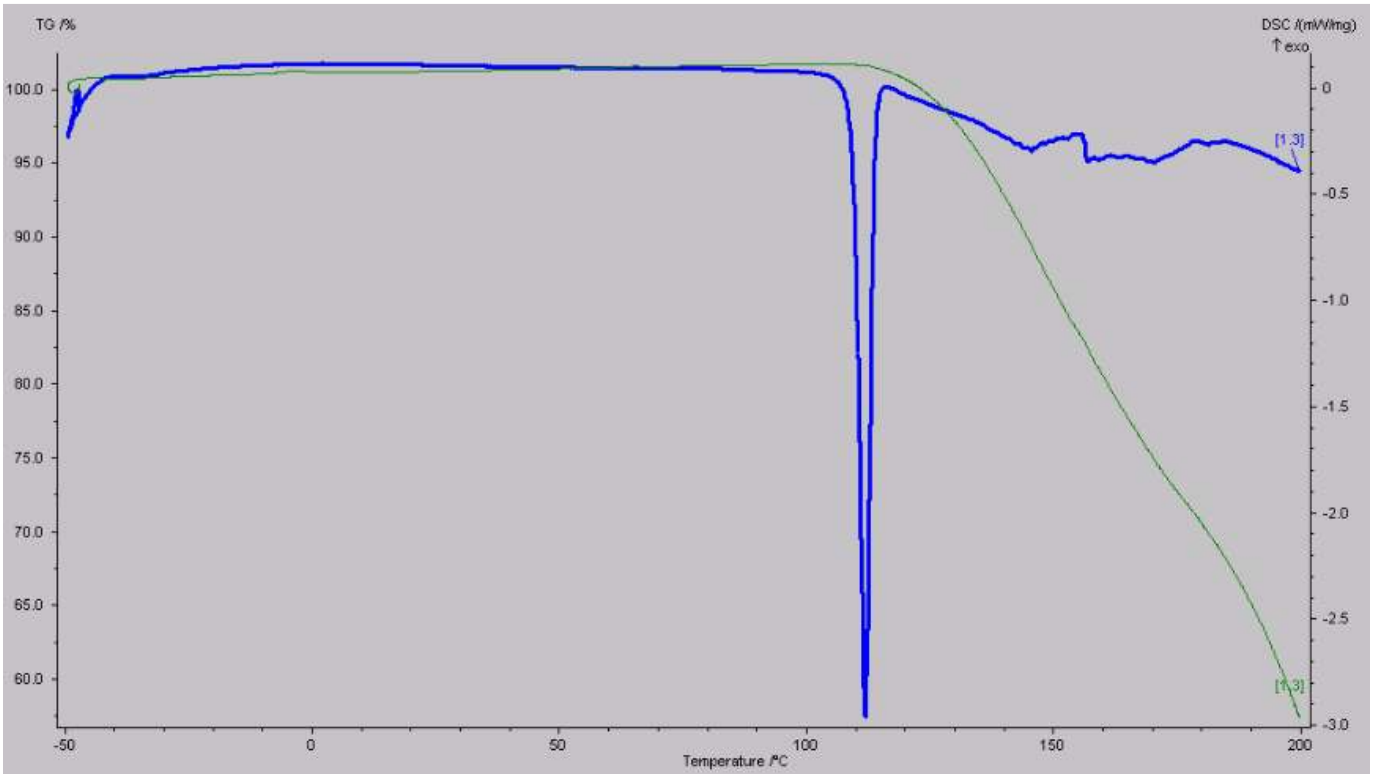

DSC trace of a sample CBZ:BEN co-crystal in the range -50 - 200°C

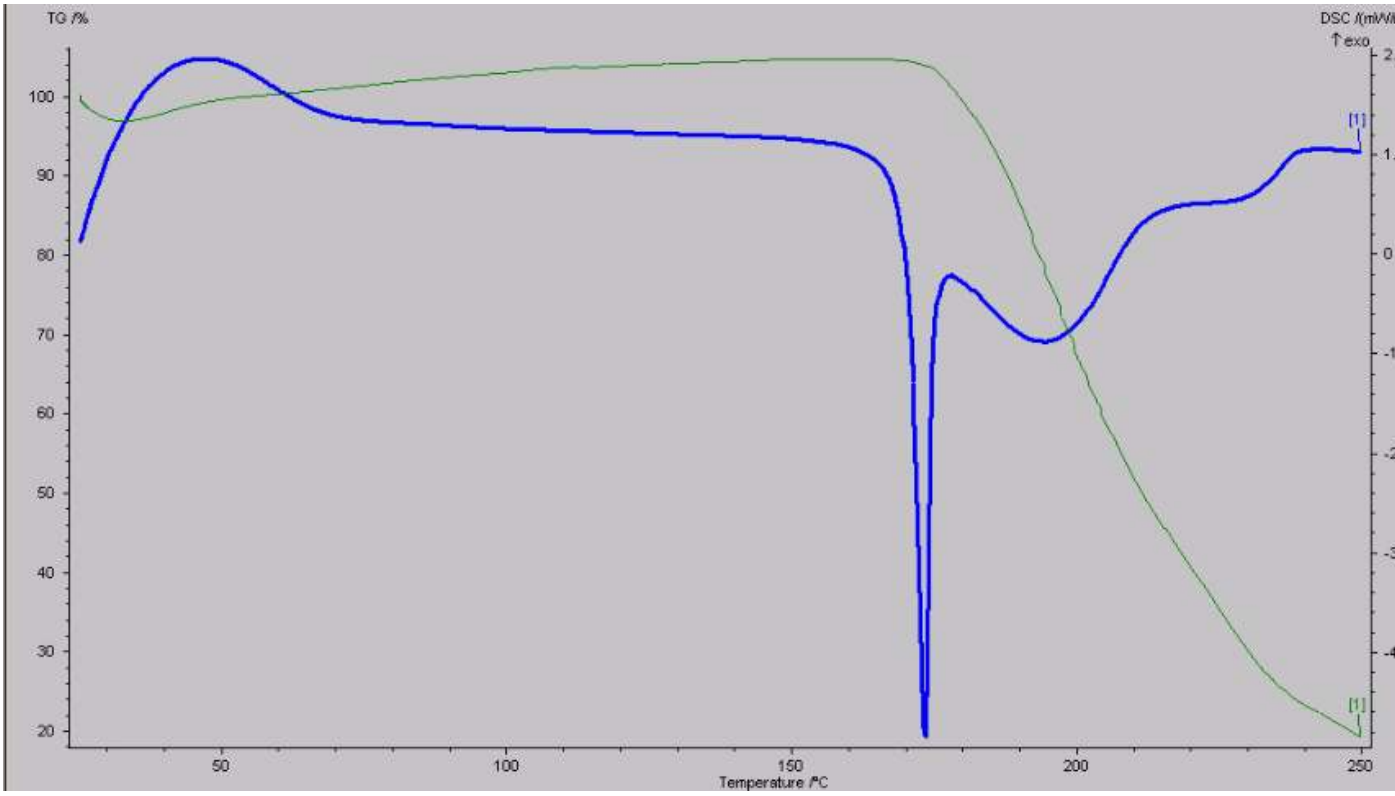

DSC trace of a sample of CBZ:HNA co-crystal in the range 20-250°C

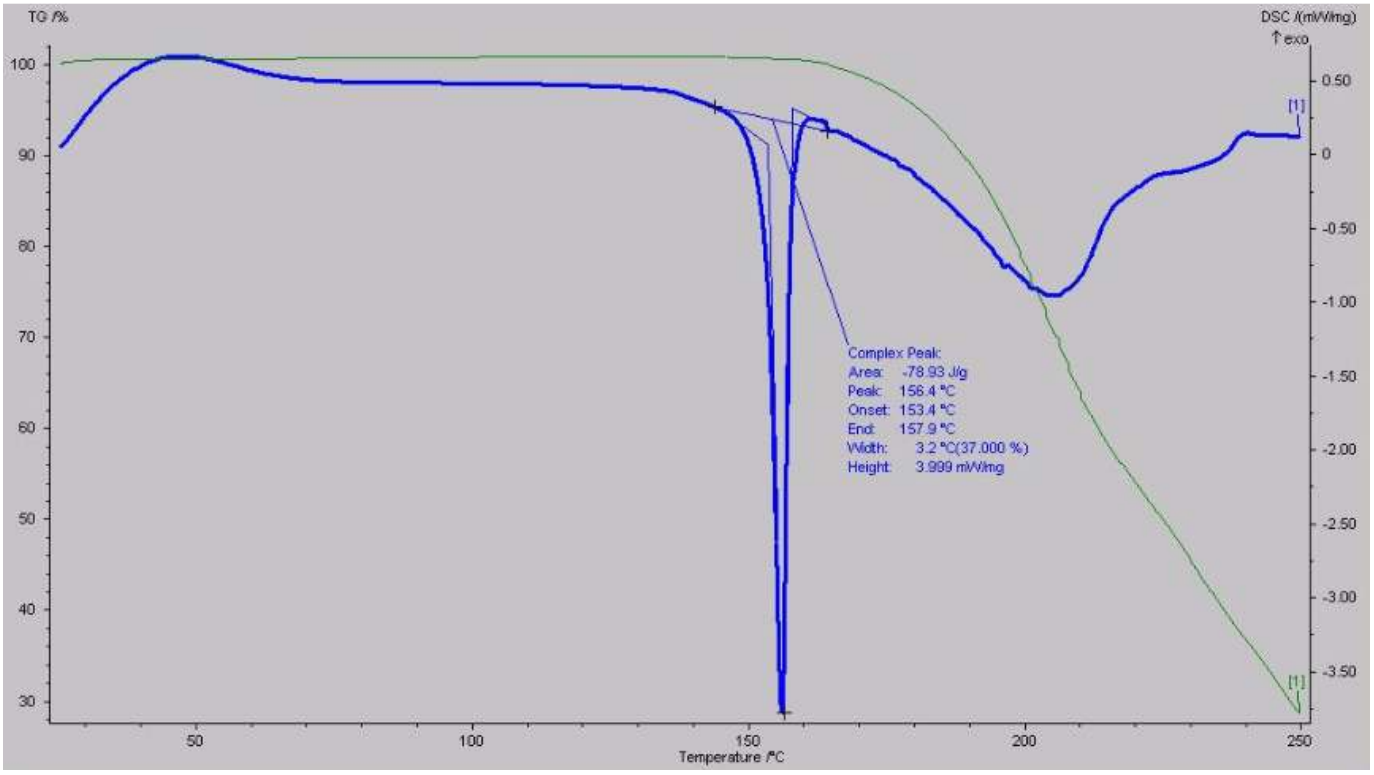

DSC trace of a sample of CBZ:CAM co-crystal in the range 20-250°C showing evaluation of the melting poin